

École Doctorale des Sciences Chimiques — ED 222

CNRS UMR7006, ISIS

THÈSE présentée par

Tanul GUPTA

soutenue le 10 December 2024

pour obtenir le grade de **Docteur de l'Université de Strasbourg**

Discipline/Spécialité : **Physique**

Novel phases in long-range interacting quantum many-body systems

THÈSE dirigée par / DISSERTATION supervisor :

Pr. PUPILLO Guido

Professeur, Université de Strasbourg

RAPPORTEURS :

Pr. FRANCHINI Fabio

Professeur, RUĐER BOŠKOVIĆ INSTITUTE

Pr. KOKKELMANS Servaas

Professeur, Eindhoven University of Technology

AUTRES MEMBRES DU JURY / OTHER MEMBERS OF THE JURY :

Pr. ERCOLESSI Elisa

Professeur, University of Bologna

Pr. MANFREDI Giovanni

Directeur de Recherche, IPCMS



This page would be intentionally left blank if we would not wish to inform about that.

Avertissement au lecteur / Warning to the reader

Ce document est le fruit d'un long travail approuvé par le jury de soutenance et mis à disposition des membres de la communauté universitaire. Il est soumis à la propriété intellectuelle de l'auteur. Cela implique une obligation de citation et de référencement lors de l'utilisation de ce document. D'autre part, toute contrefaçon, plagiat, reproduction ou représentation illicite encourt une poursuite pénale.

This document is the result of a long process approved by the jury and made available to members of the university community. It is subject to the intellectual property rights of its author. This implies an obligation to quote and reference when using this document. Furthermore, any infringement, plagiarism, unlawful reproduction or representation will be prosecuted.

[Code de la Propriété Intellectuelle](#)

[Article L122-4](#) :

Toute représentation ou reproduction intégrale ou partielle faite sans le consentement de l'auteur ou de ses ayants droit ou ayants cause est illicite. Il en est de même pour la traduction, l'adaptation ou la transformation, l'arrangement ou la reproduction par un art ou un procédé quelconque.

Any representation or reproduction in whole or in part without the consent of the author or his successors in title or assigns is unlawful. The same applies to translation, adaptation or transformation, arrangement or reproduction by any art or process whatsoever.

[Articles L335-1 à L335-9](#) : Dispositions pénales / Penal provisions.

Licence attribuée par l'auteur / Licence attributed by the author

[Veillez à ne conserver que la licence qui vous convient / Make sure you only keep the licence that suits you best]



<https://creativecommons.org/licenses/?lang=fr-FR>

Tanul GUPTA
Novel phases in long-range interacting
quantum many-body systems

Résumé

Cette thèse explore les propriétés de l'état fondamental des systèmes bosoniques 1D fortement corrélés avec un saut à longue portée, où la cohérence quantique et les phénomènes collectifs induisent des comportements distincts de ceux des systèmes à interactions de courte portée. En utilisant des méthodes numériques avancées comme la Monte Carlo à intégrale de chemin et l'algorithme du ver, elle analyse les transitions de localisation induites par le désordre et les interactions, du superfluide à l'état non-superfluide, avec un saut décroissant selon une loi de puissance. Une découverte clé est une transition de phase quantique continue et invariante d'échelle, s'écartant du scénario attendu de Berezinskii-Kosterlitz-Thouless (BKT). Les résultats remettent en question la théorie de bosonisation et les études numériques de moyenne échelle, identifiant la gamme où les interactions à longue portée dominent. Ces conclusions ont des implications expérimentales pour les plateformes réalisant des modèles XY avec couplages en loi de puissance, comme les réseaux d'atomes de Rydberg et les chaînes d'ions piégés.

Mots-clés: Systèmes quantiques à plusieurs corps, Physique de la matière condensée, Méthodes numériques, Superfluidité, Transition BKT, Interactions à longue portée, Monte Carlo quantique

Abstract

This thesis investigates the ground-state properties of strongly correlated 1D bosonic systems with long-range hopping, where quantum coherence and collective effects create distinct behaviors compared to short-range systems. Using advanced numerical methods like Path Integral Monte Carlo and the Worm Algorithm, it explores disorder- and interaction-driven localization transitions from superfluid to non-superfluid states, with hopping decaying as a power law. A key finding is a continuous, scale-invariant quantum phase transition deviating from the expected Berezinskii-Kosterlitz-Thouless (BKT) scenario. The results challenge previous bosonization theory and mid-scale numerical studies, identifying the range where long-range interactions dominate. These findings have experimental relevance for platforms realizing XY models with power-law couplings, including cold dipolar atoms, Rydberg atom arrays, and trapped ion chains.

Keywords: Quantum Many-Body Systems, Condensed Matter Physics, Numerical Methods, Superfluidity, BKT Transition, Long-Range Interactions, Quantum Monte Carlo

Acknowledgements

I would like to extend my deepest gratitude to my Ph.D. advisor, Professor Dr. Guido Pupillo, for his invaluable support throughout my doctoral studies and research. Without his patience, intelligence, diligence, erudition, prompt guidance and useful advice this work would not have been realized. Working with Professor Pupillo has been an absolute pleasure and a tremendous learning experience. I am also sincerely thankful to the members of my thesis committee: Professors Fabio Franchini, Servaas Kokkelmans, Elisa Ercolessi, and Giovanni Manfredi. I am deeply appreciative of their willingness to serve on my committee and their insightful feedback on my work.

I extend my deepest gratitude to Dr. Guido Masella for his invaluable discussions on his implementation of the Worm Algorithm, which forms the foundation of this numerical study. Our engaging whiteboard sessions were both stimulating and immensely helpful. I would also like to thank Dr. Francesco Mattiotti, who was my primary resource whenever I encountered challenges or roadblocks in my work. His insights were instrumental in helping me navigate these obstacles successfully.

I would also like to express my gratitude to Prof. Nikolay Prokof'ev, the creator of the Worm Algorithm, for the enlightening discussions and his contributions to this research.

I thank the Centre Européen de Sciences Quantiques (CESQ), University of Strasbourg for facilitating such a positive learning and research environment. I am especially thankful to Anna Guyon and Annia Bertrand for their invaluable assistance with organizational and administrative matters. I also gratefully acknowledge the fellowship from the MOQS program, and extend special thanks to Dr. Juliane Sauer for her dedicated support with administrative aspects of my research. I thank my fellow colleagues of the Quantum Matter Theory group here in Strasbourg: Dr. David Hagenmuller, Dr. Johannes Schachenmayer, Dr. Cyriaque Genet, Dr. Jerome Dubail. Last but not the least, I would like to thank my family, my parents, brother, and sister for supporting me spiritually and emotionally throughout this work and my life in general.

Finally, to Urvashi: thank you for your sticking with me in this journey. You were there to celebrate every win, pick me up after every setback, and remind me why I started this in the

first place. Your support, patience, and all the little moments we shared kept me going. I'm so lucky to have you in my life.

Résumé de la Thèse en Français

En physique quantique des systèmes à plusieurs corps, il est bien établi que les interactions à longue portée, telles que les couplages qui décroissent selon une loi de puissance avec la distance, $1/r^\alpha$, peuvent donner lieu à des phénomènes physiques nouveaux, aussi bien dans les propriétés d'équilibre que hors d'équilibre des systèmes quantiques. Ces interactions peuvent être réalisées expérimentalement dans des systèmes atomiques, moléculaires et optiques avancés [1–5], ce qui a récemment ravivé l'intérêt pour l'étude de ces effets.

Durant mes recherches de doctorat, j'ai étudié les phases de l'état fondamental de particules bosoniques avec un saut décroissant selon une loi de puissance ($1.0 < \alpha < 3.0$), dans des systèmes avec ou sans désordre. Nos résultats montrent que la décroissance en loi de puissance de l'élément de matrice de saut influence significativement la nature des transitions de phase quantiques dans ces systèmes. Pour les systèmes bosoniques unidimensionnels à interactions de courte portée, il est bien connu, grâce aux travaux de Giamarchi et al. [6, 7], que la transition entre les états superfluides et non-superfluides suit le mécanisme de Berezinskii-Kosterlitz-Thouless (BKT). Cependant, à l'aide de simulations à grande échelle par Monte Carlo quantique, nous avons démontré que la transition de phase quantique induite par le désordre dans les bosons durs unidimensionnels présente des fluctuations invariantes à l'échelle du nombre d'enroulements au point de transition, indiquant une transition de type non-BKT [8].

Cette étude a ensuite été étendue pour explorer l'impact du saut à longue portée sur les bosons à interaction douce. Nous avons découvert que l'interaction entre le saut en loi de puissance et la répulsion locale dans le modèle de Bose-Hubbard conduit à l'émergence d'un véritable ordre à longue portée (LRO) pour $\alpha < 2.0$, déviant de l'ordre quasi à longue portée généralement attendu dans les systèmes bosoniques unidimensionnels à interactions de courte portée.

Introduction

Les systèmes à interactions à longue portée se réfèrent à des systèmes dans lesquels la force d'interaction entre les éléments décroît lentement avec la distance, suivant souvent une loi de puissance $1/r^\alpha$, où r est la distance entre les éléments et α est l'exposant de décroissance. Contrairement aux interactions à courte portée, où les effets sont localisés, les interactions à longue portée influencent l'ensemble du système, conduisant à un comportement collectif et à des dynamiques complexes et non triviales. Dans le cadre de notre étude, nous utiliserons la classification des systèmes à longue portée proposée par [9].

Pour les systèmes quantiques en d dimensions, une distinction clé émerge selon que $\alpha < d$ ou $\alpha > d$. Lorsque $0 < \alpha \leq d$, les interactions décroissent suffisamment lentement pour induire une non-additivité, où l'énergie totale ne s'échelonne pas linéairement avec le nombre de constituants microscopiques N . Cela définit le *régime à longue portée forte*, dans lequel l'énergie ne peut pas simplement être sommée sur des sous-systèmes. Même pour $\alpha > d$, les interactions à longue portée peuvent encore influencer le comportement critique du système et la propagation des excitations jusqu'à α^* , où $\alpha^* > d$ est une valeur critique de l'exposant. Ce régime, que nous appellerons *régime à longue portée faible*, est d'un intérêt particulier, et dans ce travail, nous cherchons à l'explorer dans le contexte des systèmes bosoniques unidimensionnels. En résumé, les trois régimes fondamentaux sont :

- Régime à longue portée forte : $\alpha < d$
- Régime à longue portée faible : $d < \alpha < \alpha^*$
- Régime à courte portée : $\alpha > \alpha^*$

Dans ce travail, nous avons exploré numériquement les phases de l'état fondamental des systèmes bosoniques unidimensionnels avec un saut suivant une loi de puissance pour $\alpha > d$, se situant dans les régimes à longue portée faible et à courte portée. Nous utilisons des simulations Quantum Monte-Carlo à grande échelle, numériquement exactes, basées sur l'algorithme du Worm [10]. Pour les bosons à interaction forte (hardcore bosons), nous considérons le hamiltonien \mathcal{H}_1 confiné à un réseau unidimensionnel et étudions la transition de localisation induite par le désordre. Pour les bosons à interaction douce (softcore bosons), nous examinons la transition de Mott insulateur (MI) à superfluide (SF) induite par l'interaction décrite par \mathcal{H}_2 .

$$\mathcal{H}_1 = -t \sum_{i < j} \frac{a^3}{|r_{ij}|^\alpha} \left[b_i^\dagger b_j + b_j^\dagger b_i \right] + \sum_i \varepsilon_i n_i = V + H_0 \quad (1)$$

$$\mathcal{H}_2 = -t \sum_{i<j} \frac{a^3}{|r_{ij}|^\alpha} \left[b_i^\dagger b_j + b_j^\dagger b_i \right] + \frac{U}{2} \sum_i n_i(n_i - 1), \quad (2)$$

Nous employons les notations standard pour les opérateurs de création et d’annihilation bosoniques sur le site i et limitons le nombre d’occupations maximal, $n_i = b_i^\dagger b_i$, à l’unité. L’amplitude de saut entre sites voisins, t , et l’espacement du réseau, a , sont respectivement pris comme unités d’énergie et de longueur. Nous choisissons des énergies locales aléatoires ε_i uniformément réparties entre $-W$ et W . Les amplitudes de saut entre les sites i et j décroissent avec la distance suivant $1/r^\alpha$, et ε_i représentent les énergies locales aléatoires. U est la répulsion locale lorsque deux bosons occupent le même site du réseau. Il est à noter que pour les bosons à interaction forte (hardcore bosons), $U \rightarrow \infty$, ce qui impose la contrainte qu’un site ne peut être occupé que par un seul boson.

Worm algorithm

Les méthodes de Monte Carlo par intégrale de chemin (PIMC) [11] appartiennent à une classe d’algorithmes de Monte Carlo quantique (QMC) basés sur une représentation graphique des lignes de monde pour la fonction de partition Z . En termes de H_0 et V , la fonction de partition peut être exprimée comme $Z = \text{Tr}[\rho]$, où $\rho = e^{-\beta H} = e^{-\beta H_0} \sigma$. L’opérateur d’évolution de Matsubara σ est

$$\sigma = 1 - \int_0^\beta d\tau V(\tau) + \dots + (-1)^m \int_0^\beta d(\tau_m) \dots \int_0^{\tau_2} d\tau_1 V(\tau_m) \dots V(\tau_1) + \dots \quad (3)$$

Z peut alors être exprimé comme une somme de configurations de lignes de monde C_n avec un nombre différent de coudes n .

$$Z = \sum_{n=0}^{\infty} \sum_{C_n} W(C_n)$$

$$\langle O \rangle = \frac{1}{Z} \text{Tr}[O e^{-\beta \mathcal{H}}] = \frac{1}{Z} \sum_{n=0}^{\infty} \sum_{C_n} \langle O \rangle_{C_n} W(C_n) \quad (4)$$

La valeur d’espérance des observables donnée par l’équation 4 peut alors être calculée efficacement via les méthodes de Monte Carlo par chaîne de Markov en échantillonnant des configurations C_n à partir de la distribution $W(C_n)/Z$. L’algorithme du Worm est un schéma permettant de mettre à jour les configurations PIMC en effectuant un échantillonnage dans un espace de configurations étendu $\mathcal{G} = \text{Tr} \left[\mathcal{F}(b_i^\dagger(t_M) b_j(t_i) e^{-\beta \mathcal{H}}) \right]$.

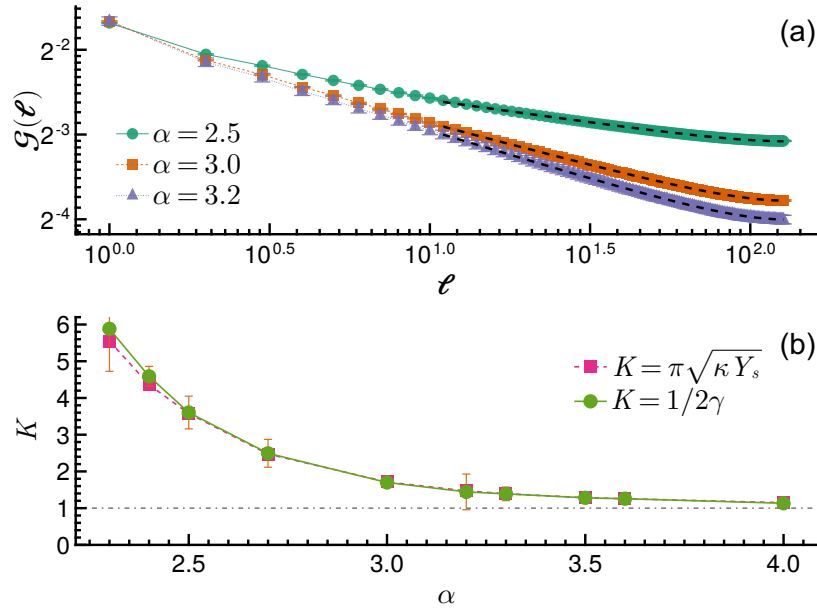


Fig. 1 Caractérisation de la phase superfluide pour $W/t = 0$: (a) Matrice de densité à une particule $\mathcal{G}(\ell)$ en fonction de la distance ℓ , montrant une décroissance algébrique pour toutes les valeurs de α avec $L = 256$. Les lignes pointillées indiquent le meilleur ajustement avec $A \cdot c(\ell)^{-\gamma}$, où $c(\ell) = \sin(\pi\ell/L)/\sin(\pi/L)$ est la distance de corde et A, γ sont des paramètres d'ajustement. (b) Évaluation numérique du paramètre de liquide de Luttinger K en fonction de α , à partir de la décroissance en loi de puissance $\mathcal{G} \propto \ell^{-1/(2K)}$ (points verts) et de la relation $K = \pi\sqrt{\kappa Y_s}$ (carrés rouges), extrapolée à la limite thermodynamique via une mise à l'échelle polynomiale en $1/L$.

Résultats et discussions

Pour caractériser les phases quantiques des hamiltoniens \mathcal{H}_1 (équation 1) et \mathcal{H}_2 (équation 2), nous analysons la rigidité superfluide, $Y_s = L\langle \mathcal{W}^2 \rangle / \beta$, où $\langle \mathcal{W}^2 \rangle$ est la moyenne des carrés du nombre d'enroulements obtenue à partir des simulations, L est la taille du réseau 1D, et β est l'inverse de la température. De plus, nous examinons la matrice de densité à une particule, $\mathcal{G}(l) = \langle b_i^\dagger(\tau)b_{i+l} \rangle$, afin d'explorer plus en détail le comportement de phase du système.

Hardcore Bosons sur un réseau désordonné en 1D

Nous commençons notre analyse par la caractérisation du liquide bosonique en l'absence de désordre ($W/t = 0$). Pour un état fondamental superfluide unidimensionnel, la matrice de densité à une particule $\mathcal{G}(\ell)$ devrait présenter une décroissance algébrique avec la distance ℓ , avec une intégrale divergente sur l'espace. Nos données pour \mathcal{G} sont présentées dans la Fig.

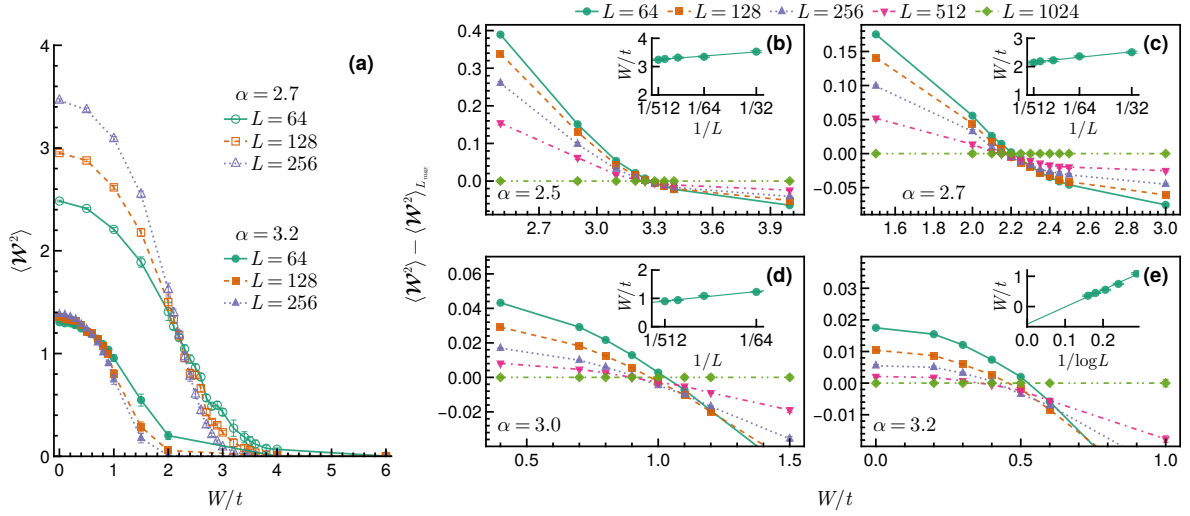


Fig. 2 Caractérisation de la transition de la phase superfluide à la phase non-superfluide pour \mathcal{H}_1 : (a) Nombre moyen des carrés d'enroulement $\langle \mathcal{W}^2 \rangle$ en fonction de la force du désordre W/t pour $\alpha = 2.7$ (symboles vides) et 3.2 (symboles pleins) pour les tailles de système $L = 64, 128, 256$. (b)-(e) Zoom sur la zone près des transitions de phase pour $\alpha = 2.5, 2.7, 3.0$ et 3.2 , montrant le croisement entre les courbes ; la courbe correspondant à la plus grande taille est soustraite de toutes les données pour plus de clarté. Les barres d'erreur verticales indiquent l'incertitude estimée provenant des simulations Monte Carlo et des moyennes sur le désordre. Insets : Mise à l'échelle de la taille finie des points de croisement entre les courbes pour les tailles de système L_1 et $L_2 = 2L_1$ en fonction de $L = L_1$.

3.1(a), pour les mêmes valeurs de α dans un système avec $L = 256$ sites et une température inverse $\beta = L/t$. Nous observons une décroissance algébrique $\mathcal{G} \sim \ell^{-\gamma}$ pour toutes les valeurs de α . Nous avons tenté une comparaison avec les attentes de la théorie des liquides de Luttinger en extrayant un paramètre effectif K en fonction de α par deux méthodes standard : la décroissance en loi de puissance $\mathcal{G} \sim \ell^{-\gamma}$ via la relation de bosonisation $\gamma = 1/(2K)$ (points verts) et la relation $K = \pi\sqrt{\kappa Y_s}$ (carrés rouges). Les valeurs de κ et Y_s peuvent être facilement calculées par Monte Carlo quantique à partir des fluctuations du nombre moyen de particules N et du nombre d'enroulements \mathcal{W} , en utilisant la relation de Pollock–Ceperley $Y_s = L\langle \mathcal{W}^2 \rangle/\beta$. La Fig. 3.1(b) montre que les deux méthodes produisent des estimations similaires de K pour toutes les valeurs de α , dans les barres d'erreur. De plus, K diminue de manière monotone et continue avec α , passant d'une grande valeur $K > 5$ à $\alpha \sim 2,3$ à $K \approx 1$ à $\alpha = 4$. Ce comportement s'explique par le fait que le saut en loi de puissance dans l'hamiltonien (1) permet des échanges de particules à grande échelle pour des valeurs suffisamment petites de $\alpha < 3$, imitant le comportement des bosons à noyau mou, pour lesquels on peut facilement obtenir $K \gg 1$. La valeur $K = 1$ (ligne pointillée) correspond au cas à courte portée des bosons

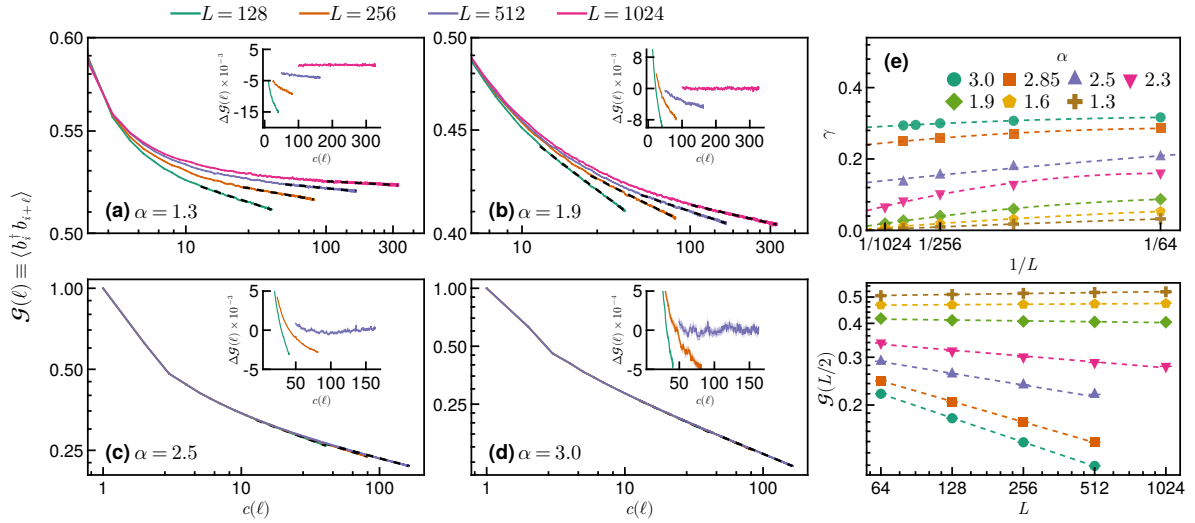


Fig. 3 Caractérisation de la phase superfluide : (a)-(d) Matrice de densité à une particule $\mathcal{G}(l)$ en fonction de l pour $\alpha = 1.3, 1.9, 2.5$, et 2.7 . La ligne en pointillés indique le meilleur ajustement avec $A \cdot c(l)^{-\gamma}$ où $c(l) = \sin(\pi l/L)$ est la distance de corde et A, γ sont les paramètres d'ajustement. Inset : $\Delta \mathcal{G}(l) = \mathcal{G}(l) - \mathcal{G}_{fit}$ est la différence entre les valeurs réelles de la matrice de densité à une particule et l'ajustement théorique \mathcal{G}_{fit} pour L_{max} . La différence indique une tendance à la hausse de $\mathcal{G}(l)$ avec l'augmentation de la taille du réseau. (e) Échelle thermodynamique de l'exposant de loi de puissance γ , indiquant un véritable Ordre de Longue Portée (LRO) pour $\alpha \leq 2 \pm 0.1$.

à noyau dur avec le saut entre voisins immédiats, une limite qui est ici asymptotiquement atteinte pour $\alpha > 3$.

Dans ce qui suit, nous analysons la situation en présence de désordre fini et, en particulier, nous explorons la nature du point de transition, qui est attendu comme étant du type BKT pour les liquides de Luttinger. Cependant, nous notons que cela pourrait ne pas être le cas ici : la transition BKT et son flux RG asymptotiquement exact reposent sur des interactions logarithmiques entre les excitations de vortex. Ces interactions proviennent de l'énergie cinétique du flux autour des vortex $E \sim \int (n_s/m) dr/r$, où m est la masse des particules et n_s la densité superfluide. Le spectre à une particule dans notre modèle n'est pas parabolique et correspond formellement à une « masse » dépendante de l'échelle $m(r) \sim r^{3-\alpha}$, ce qui implique que les vortex dans la phase superfluide devraient être liés par un potentiel en loi de puissance, et non logarithmique. Il peut donc être attendu que la physique BKT ne s'applique plus pour $\alpha \lesssim 3$.

Nous caractérisons la transition via les fluctuations du nombre d'enroulements $\langle \mathcal{W}^2 \rangle$ car elles sont une quantité invariant à l'échelle, contrairement à la rigidité superfluide Y_s . La Figure 3.2(a) montre l'évolution des propriétés superfluides mesurées par $\langle \mathcal{W}^2 \rangle$ en fonction du

désordre W/t , pour deux cas exemplaires $\alpha = 2.7$ (symboles vides) et 3.2 (symboles pleins) et pour plusieurs valeurs de $L = 64, 128, 256$. Dans les deux cas, $\langle \mathcal{W}^2 \rangle$ diminue monotoniquement avec l'augmentation de W/t , jusqu'à atteindre des valeurs proches de zéro. Ce comportement signale la transition entre les états superfluides et non-superfluides. Dans le cas à courte portée $\alpha = 3.2$, le comportement à des valeurs plus élevées de désordre rappelle ce qui est attendu pour une transition BKT lorsque, dans le système infini, $\langle \mathcal{W}^2 \rangle$ affiche un saut à zéro au point critique [7]. Cependant, de manière surprenante, pour $\alpha = 2.7$, il y a un point de croisement clair de $\langle \mathcal{W}^2 \rangle$ autour de $W/t \sim 2$. Cela est incompatible avec la criticité BKT et est, au contraire, une signature de transitions de phase continues invariantes à l'échelle. Ce fait peut être utilisé pour déterminer la force critique du désordre W_c où la superfluidité est perdue, en observant le point de croisement des courbes $\langle \mathcal{W}^2 \rangle$ en fonction de W pour différentes valeurs de L . Les panneaux (b)-(e) de la Fig. 3.2 présentent les données dans la proximité des points de transition pour $\alpha = 2.5, 2.7, 3.0$ et 3.2 en utilisant $\beta = L/8t$ [même pour $\alpha = 3.2$, notre température est un facteur deux plus petite que le mode phonon le plus bas]. Les points de croisement sont très prononcés dans (b) et (c) pour des exposants intermédiaires α , laissant peu de doute sur le fait que nous traitons de transitions continues génériques à $W/t = 3.24(5)$ pour $\alpha = 2.5$ et à $W/t = 2.12(5)$ pour $\alpha = 2.7$. Les croisements semblent persister lors du passage au régime à courte portée $\alpha \gtrsim 3$, voir les panneaux (d) et (e) dans la Fig. 3.2 avec des croisements autour de $W/t = 0.87(5)$ pour $\alpha = 3.0$ et autour de $W/t = 0.5(5)$ pour $\alpha = 3.2$, contrairement à toutes les attentes. Cependant, une mise à l'échelle soigneuse pour des tailles de système plus grandes jusqu'à $L = 1024$ montre que le point de transition pour $\alpha > 3$ se déplace vers $W/t \rightarrow 0$ dans la limite thermodynamique, voir l'Inset dans la Fig. 3.2(e), impliquant l'absence de transition de phase continue à W fini dans la limite thermodynamique. Cela est différent de $\alpha \leq 3$, où le point de transition se déplace vers une valeur finie de W/t , voir les Insets dans la Fig. 3.2(b-d). La rupture du scénario BKT pour toutes les valeurs $2 < \alpha \leq 3$ dans l'équation (1) est surprenante et constitue le principal résultat de ce travail.

Transition induite par interaction dans le modèle de Bose-Hubbard à loi de puissance

Nous avons réalisé des simulations du Hamiltonien \mathcal{H}_2 pour $1.0 < \alpha < 3.0$ dans l'ensemble grand canonique à une densité commensurable afin d'étudier la nature de la transition non triviale entre l'isolant de Mott et le superfluide (MI-SF) et de caractériser la phase superfluide [12]. La matrice de densité à une particule, $\mathcal{G}(l)$, pour $\alpha = 1.3, 1.9, 2.5$, et 3.0 , tracée en fonction de la distance de corde $c(l)$, est montrée dans la Figure 3.3(a-d). Pour $\alpha < 2.0$ (Figure

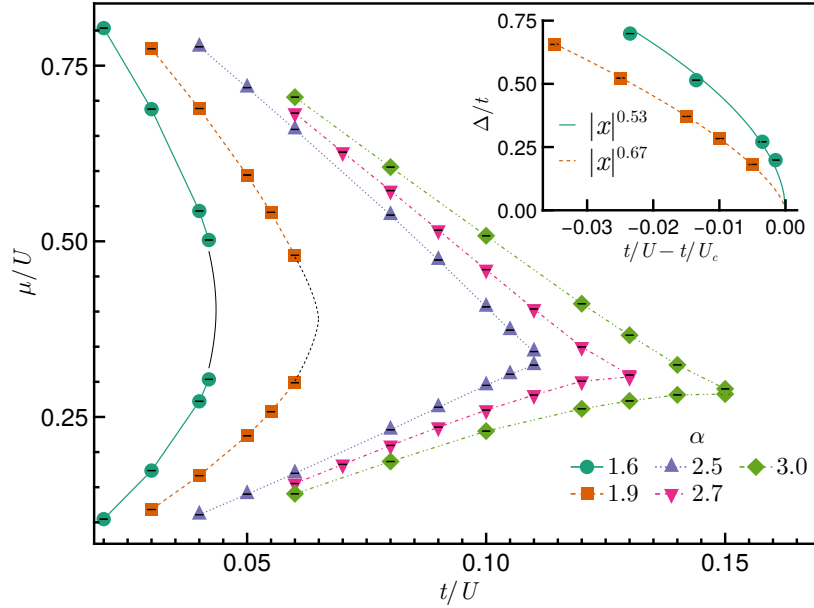


Fig. 4 Diagramme de phase de l'état fondamental du modèle de Bose-Hubbard en 1D avec des sauts suivant une loi de puissance (Equation (2)) pour $\alpha = 1.6, 1.9, 2.5, 2.7,$ et 3.0 , montrant la frontière entre les régions d'isolant de Mott (avec une densité unitaire) et de superfluide en fonction du potentiel chimique μ/U et de l'amplitude de saut t/U .

3.3(a-b)), l'exposant de loi de puissance tend vers zéro dans la limite thermodynamique (Figure 3.3(e)), indiquant la présence d'un véritable Ordre de Longue Portée (LRO). En revanche, pour $\alpha > 2.0$, $\mathcal{G}(l)$ montre une décroissance algébrique, $\mathcal{G}(l) \sim c(l)^{-\gamma}$, où γ est l'exposant de la loi de puissance. Notamment, $\mathcal{G}(l)$ augmente avec la taille du système L , exhibant un comportement anormal par rapport à ce qui est observé dans les interactions à courte portée. Comme l'exposant de loi de puissance reste fini dans la limite thermodynamique (Figure 3.3(e)), nous classifions la phase pour $2.0 \pm 0.1 < \alpha < 3.0$ comme un Ordre Quasi-Long-Range Anormal (AQLRO).

Le diagramme de phase dans le plan μ/U en fonction de t/U est présenté dans la Figure 4. Pour $\alpha < 2$, le diagramme révèle des structures lobe-like lisses caractéristiques de la phase d'isolant de Mott (MI) observée dans des dimensions supérieures. En particulier, pour $\alpha = 1.6$ et 1.9 , les lobes de Mott près de la transition ont été théoriquement ajustés en estimant l'exposant de longueur de corrélation ν , en utilisant l'énergie de gap E_{gap} en fonction de t/U . Ces ajustements théoriques sont représentés par des lignes noires dans la figure. La forme lobe-like lisse indique l'émergence d'un ordre de longue portée, en accord avec le comportement observé dans les fonctions de corrélation. Pour $\alpha > 2$, la phase MI présente une structure plus pointue le long de la ligne de densité commensurable. Cette caractéristique marquée

est indicative de la nature quasi-longue portée de la phase sous-jacente, contrastant avec le comportement lisse observé pour des valeurs plus petites de α .

Conclusion générale

Nous avons étudié les phases de l'état fondamental des bosons à cœur dur en une dimension avec des sauts suivant une loi de puissance en présence de désordre, en utilisant des techniques de Monte Carlo sur intégrale de chemin (PIMC). Nos résultats révèlent une transition de phase non-Berezinskii-Kosterlitz-Thouless (BKT) à invariance d'échelle entre les phases superfluide et non-superfluide pour diverses valeurs de l'exposant α . À travers une analyse détaillée du modèle de Bose-Hubbard à loi de puissance, nous montrons que le véritable comportement de longue portée est observable pour $\alpha < 2.0$, comme en témoignent les fonctions de corrélation et le diagramme de phase isolant de Mott-superfluide (MI-SF). Ces résultats remettent en question la notion prédominante dans la littérature actuelle, qui suggère que l'ordre de longue portée émerge autour de $\alpha \sim 2.7$ [13]. Nos simulations à grande échelle montrent de manière concluante que ce n'est pas le cas.

Table of contents

Résumé de la Thèse en Français	ix
1 Introduction	1
1.1 Phase Transitions and Critical Phenomena in Condensed Matter Physics . . .	2
1.2 Superfluidity	5
1.3 Bose-Hubbard Model	9
1.4 Berezinskii–Kosterlitz–Thouless (BKT) transition	13
1.4.1 2D XY model	15
1.4.2 Mapping of 2D XY model to 2D coulomb gas and 1D sine-Gordon model	20
1.5 Long-range interactions	22
1.6 Outline of the results	25
2 Quantum Monte Carlo Methods	29
2.1 Monte Carlo methods	29
2.2 Path Integral Monte Carlo methods	35
2.2.1 Worm Algorithm	40
2.2.2 Observables	42
3 Scale invariant phase transition of disordered bosons in one dimension	47
4 Bose-Hubbard model with power-law hopping in one dimension	57
5 Conclusions and Outlook	67
Appendix A Supplemental Material: Scale-invariant phase transition of disordered bosons in one dimension	71
A.1 Dispersion relation in the superfluid phase with finite disorder	71

Table of contents

Appendix B Supplemental Material: Bose-Hubbard model with power-law hopping in one dimension	73
B.1 One-body density matrix for hardcore bosons on 1D lattice	73
B.1.1 Condensate Fraction	74
B.1.2 Fitting of $\mathcal{G}(\ell)$	75
B.2 Single particle density matrix for softcore bosons on 1D lattice	76
List of figures	79
Bibliography	87

Chapter 1

Introduction

Quantum many-body systems with long-range, power-law decaying couplings offer a unique landscape for exploring behaviors and emergent phenomena that lie beyond the scope of traditional complex systems. In classical systems, long-range interactions are seen in models where gravitational or electrostatic forces dominate, whereas in quantum systems, examples include dipole-dipole or van der Waals interactions. These long-range forces influence collective dynamics on scales often leading to complex behaviors, exotic phases, and novel dynamical properties absent in short-range systems. In particular, long-range interactions may lead to divergence of thermalization timescale in classical systems, and may even disrupt the traditional notion of locality in quantum systems leading to non-local propagation of information and correlations. This breakdown of locality positions long-range interacting systems as a fertile ground for discovering unusual thermodynamic and quantum behaviors, including novel phase transitions and unconventional equilibrium phases.

In the broader field of condensed matter physics, researchers investigate systems composed of vast numbers of interacting particles in condensed phases, such as solids and liquids. Unlike isolated atoms, these systems exhibit *emergent phenomena* arising from collective interactions, as seen in materials like crystals, magnets, and superconductors. At low temperatures, their macroscopic properties are governed by quantum mechanics and, in theory, can be derived from the many-body Schrödinger equation. However, the sheer number of particles involved—often on the order of 10^{23} —renders a direct solution of this equation computationally infeasible, surpassing the capabilities of even the most advanced conceivable classical computers. This complexity necessitates the development of approximate numerical methods and theoretical frameworks to understand macroscopic properties effectively. Techniques such as mean-field theory, density functional theory (DFT), and quantum Monte Carlo simulations are essential for capturing the key features of collective behavior. By advancing the study of both short- and long-

range interactions, condensed matter physics provides a robust foundation for understanding the intricate properties and emergent phenomena that characterize complex materials, offering insights that are crucial for the advancement of materials science and quantum technology.

This thesis focuses on quantum many-body systems with long-range interactions, where quantum effects intertwine with power-law decaying couplings, opening up new avenues for exploring complex behaviors and emergent phenomena. In this chapter, we will begin by discussing the theory of phase transitions in Section 1.1, where we examine how microscopic fluctuations drive fundamental changes in state. We will explore critical phenomena associated with these transitions, including the divergence of correlation length and time near critical points, as well as the scale-invariant properties and power-law behaviors observed in both classical and quantum phase transitions. We will then explore the origins of superfluidity in Section 1.2, an exotic quantum phase observed in bosonic systems, where particles exhibit frictionless flow. In Section 1.3, we introduce the Bose-Hubbard model, a foundational framework for describing quantum phases in lattice systems, particularly the transition between superfluid and Mott-insulator states. We then review the Berezinskii–Kosterlitz–Thouless (BKT) transition in Section 1.4, a topological phase transition that differs from conventional symmetry-breaking transitions, explaining how 2D systems move from quasi-long-range order to disordered phases due to vortex-antivortex unbinding, which disrupts phase coherence. This section further illustrates the mapping of vortex dynamics in the XY model to models of a Coulomb gas and the sine-Gordon model. In Section 1.5, we investigate the impact of long-range interactions on strongly correlated systems, exploring how these interactions lead to novel phases and critical phenomena. Finally, in Section 1.6, we provide a brief outline of the thesis structure, summarizing the key objectives and contributions of this work.

1.1 Phase Transitions and Critical Phenomena in Condensed Matter Physics

A key aspect of emergent behavior in condensed matter systems is the occurrence of phase transitions, where a system undergoes fundamental change in state, such as melting, freezing, or the onset of superconductivity. These transitions are driven by microscopic fluctuations. The universe itself has likely experienced several phase transitions as it cooled from the high-temperature plasma state following the Big Bang to its present form [14]. When temperature is the driving factor, thermal fluctuations are responsible for the transition. As the sample temperature is raised above critical temperature T_c , thermal fluctuations—scaled by $k_B T$, where

1.1 Phase Transitions and Critical Phenomena in Condensed Matter Physics

k_B is the Boltzmann constant and T the temperature—destroy the system’s order and drive it across the phase transition. The high-temperature phase, therefore, typically exhibits greater disorder and higher symmetry compared to the low-temperature phase. However, when the temperature of the system approaches zero, all thermal fluctuations die out. This prohibits phase transition in classical systems at zero temperature. Quantum fluctuations, driven by Heisenberg’s uncertainty principle, however, continue to live on at zero temperature and under certain conditions trigger the system to undergo *quantum phase transition* (QPT). The amplitude of these quantum fluctuations can be modulated by varying external parameters in the system’s Hamiltonian. Examples include the charging energy in Josephson-junction arrays, which governs the superconductor-insulator transition [15–18]; the applied magnetic field in quantum Hall systems, which drives transitions between quantized Hall plateaus [19]; doping levels in high-temperature superconductors, which suppress antiferromagnetic order [20, 21]; the degree of disorder in conductors, influencing the metal-insulator transition and determining conductivity at zero temperature [22, 23]; and the on-site interaction strength in systems of repulsive bosons, which controls the superfluid-insulator transition [24, 19].

Phase transitions are broadly categorized into first-order and continuous (second-order) types. In first-order transitions, distinct phases coexist at the transition point, such as the coexistence of liquid and vapor during boiling. Continuous transitions, on the other hand, occur smoothly without phase coexistence and are characterized by an order parameter—a thermodynamic variable that is zero in the disordered phase and non-zero in the ordered phase. In addition to these types, there are topological transitions, such as the Berezinskii-Kosterlitz-Thouless (BKT) transition, where phase changes occur without traditional symmetry breaking (see Section 1.4). In systems that spontaneously break some symmetry in the ordered state, the value of the order parameter reflects this broken symmetry. A good example is a Heisenberg ferromagnet: The relevant symmetry of the Hamiltonian is the rotation symmetry in spin space, and the disordered and ordered states are represented by the paramagnetic and ferromagnetic states respectively. Although the average order parameter is zero in the disordered state, fluctuations remain non-zero, and near the critical point, these fluctuations become long-ranged. The correlation length ξ , which measures the spatial extent of these fluctuations, diverges as $\xi \propto |t|^{-\nu}$ where ν is the correlation length exponent and t is a dimensionless measure of distance from the critical point. If the transition is driven by disorder W and occurs at nonzero disorder W_c , t equals $|W - W_c|/W_c$. In a quantum phase transition (QPT), temporal correlations along the direction of imaginary time τ ($i\tau = k_B T$) become long-ranged, with the correlation time ξ_τ diverging as $\xi_\tau \propto \xi^z \propto |t|^{-\nu z}$, where z is the dynamic critical exponent. These divergences in correlation length and time near the critical point are central to critical

Introduction

phenomena. At the critical point, correlation length and time are infinite, fluctuations occur on all length and time scales, and the system is said to be *scale-invariant*. As a consequence all observables depend via power-laws on the external parameters.

Close to a second-order classical phase transition (CPT), the correlation length ξ becomes large (though finite) and governs the scaling behavior of the system. Since ξ is only relevant length scale, if all lengths are rescaled by a factor b while simultaneously adjusting the external tuning parameter x such that ξ maintains its initial value, the physical properties of a system should remain unchanged. This leads to a scaling form for the free-energy density f near the critical point:

$$f(t, x) = b^{-d} f\left(t b^{\frac{1}{\nu}}, x b^{y_x}\right) \quad (1.1)$$

where d is the spatial dimensionality, y_x is critical exponent associated with the external tuning parameter x , which, for example, could be magnetic field or pressure. For QPTs not only does ξ diverge in d dimensions, but also the correlation time ε_τ , acting as an extra dimension at zero temperature. Therefore, the free-energy density scales as:

$$f(t, x) = b^{(-d+z)} f\left(t b^{\frac{1}{\nu}}, x b^{y_x}\right) \quad (1.2)$$

where z is referred as the dynamic critical exponent. Thus a QPT in d spatial dimensions is equivalent to a CPT in $d + z$ dimensions.

In classical statistical mechanics, dynamics and thermodynamics are decoupled; specifically, the contributions of momentum and position in the partition function are entirely independent. For instance, calculating positional correlations does not require knowledge of particle masses. This independence simplifies the formulation of non-dynamical models, such as the Ising model, where dynamics can be ignored without loss of generality. However, this convenience does not extend to quantum systems due to the non-commutative nature of coordinates and momenta [15]. As a result, the path-integral formulation of the partition function Z inherently incorporates information on the system's imaginary-time evolution over the interval $[0, \hbar\beta]$. By employing analytic continuation, this information allows us to extract real-time dynamics:

$$G(\tau) \longrightarrow G(+it) \quad (1.3)$$

where $G(\tau) \equiv \langle 0|A(\tau)A(0)|0\rangle$ is the ground state correlation function for any operator A . Thus, in quantum statistical mechanics, thermodynamic and dynamic properties are intrinsically linked, requiring a concurrent solution—an aspect that adds depth to the field but also introduces significant complexity.

With a foundational understanding of quantum phase transitions and the intricate interplay between thermodynamics and dynamics in quantum systems, we now shift our focus to superfluidity. Superfluidity, an exotic phase of matter observed in certain bosonic systems at ultralow temperatures, vividly demonstrates the macroscopic effects of quantum coherence. In the following section, we explore the theoretical foundations of superfluidity, exploring the conditions necessary for this phase to emerge and the mechanisms underlying its remarkable, frictionless flow.

1.2 Superfluidity

Superfluidity is a state of matter characterized by the ability of a liquid to flow without viscosity. This phenomenon was first observed in 1938 in liquid helium-4 (${}^4\text{He}$) by Kapitza, and simultaneously by Allen and Misener [25]. Below a critical temperature of 2.17 K, known as the lambda temperature, liquid helium transitions from a normal phase (He-I) to a superfluid phase (He-II), where it exhibits the ability to flow through narrow capillaries and porous media without encountering resistance, a behavior Kapitza termed “superfluidity.”

The key to understanding superfluidity lies in the concept of Bose-Einstein Condensation (BEC). BEC occurs when a collection of bosons (particles with integer spin) condenses into a single one-particle quantum state at low temperatures. For ${}^4\text{He}$, which behaves as a boson, this phenomenon where a large fraction of the helium atoms occupies the same ground state leads to collective behavior that manifests as frictionless flow.

The behavior of superfluid helium can be described using the two-fluid model, initially proposed by Laszlo Tisza and later refined by Landau [26]. In this model, Helium-II was postulated to consist of two components: a *superfluid* component, which flows without resistance, and a *normal* component—composed of quasiparticles namely phonons and rotons—that behaves like a typical viscous liquid. The superfluid component carries no entropy and flows irrotationally, meaning its velocity v_s satisfies the condition $\nabla \times v_s = 0$. In contrast, the normal component carries entropy and supports viscous flow. Based on these postulates, Landau predicted that, for superfluidity to persist without dissipation, the fluid’s velocity (more precisely the superfluid component of it) must be less than a critical value v_c , given by

$$v_c = \min \left(\frac{\varepsilon(p)}{|p|} \right) \tag{1.4}$$

Introduction

where $\varepsilon(p)$ is the excitation energy at momentum p . This critical velocity represents the maximum speed at which the superfluid component can flow without generating excitations that would lead to dissipation.

The theory also predicted the excitation spectrum to consist of two different contributions, one linear, due to phonons, and another quadratic due to rotons [26, 27]. Following Landau's phenomenological model, Bogoliubov demonstrated that the excitation spectrum of a weakly interacting Bose gas at low momenta takes on a phonon-like (linear) form, $\varepsilon(p) = cp$, where c is the speed of sound [28]. It explained why a weakly interacting Bose gas can exhibit superfluidity, thereby establishing a direct link between Bose-Einstein condensation (BEC) and superfluid behavior. However, it did not explain strongly interacting fluids like liquid helium-II. In 1956, Feynman and Cohen proposed a more accurate description of the excitation spectrum of liquid helium-II that could explain not only the low-momentum phonon excitations ($\varepsilon(p) = cp$) but also the higher-momentum roton spectrum ($\varepsilon(p) = \Delta + (p - p_0^2)/2m$) observed experimentally [29]. The figure 1.1 below compares the excitation spectra of a weakly interacting Bose gas (a) proposed by Bogoliubov and a strongly interacting Bose liquid (b). For the Bose gas, the spectrum is linear at low momenta, with the critical velocity equal to the sound speed c [30]. In the Bose liquid, the spectrum shows more complex features, including a roton dip, leading to a lower critical velocity $v_c < c$. The critical velocity decreases as particle-particle interactions weaken and vanishes in an ideal gas, where $v_c = \min_p \frac{\varepsilon(p)}{|p|} = 0$ for $\varepsilon(p) = \frac{p^2}{2m}$. Thus, particle-particle interactions are essential for superfluidity.

To describe the onset of superfluidity in three-dimensional systems, a key concept is *off-diagonal long-range order*, introduced by Oliver Penrose [31]. This concept is tied to the spontaneous breaking of gauge invariance symmetry (U(1)), leading to the emergence of a macroscopic wave function and the macroscopic occupation of a single-particle ground state, known as Bose-Einstein condensation [27, 32]. More specifically, the one-particle density matrix, $\rho_1(r - r') = \langle \hat{\psi}^\dagger(r) \hat{\psi}(r') \rangle$, characterizes this order. Here, $\hat{\psi}^\dagger$ and $\hat{\psi}$ are field operators for bosonic particles. The Fourier transform of this density matrix, $n_k = \langle \hat{\psi}^\dagger(k) \hat{\psi}(k) \rangle$, is the momentum distribution, where $\hat{\psi}(k)$ and $\hat{\psi}^\dagger(k)$ annihilate and create particles with momentum k . In a Bose-Einstein condensate, a single state (e.g., $k = 0$) is macroscopically occupied, so that $n_k = N_0 \delta(k) + f(k)$, where N_0 is proportional to the total number of particles N , and $f(k)$ is a smooth function of k . For the one-body density matrix, this implies that as $|r - r'| \rightarrow \infty$, $\rho_1(r - r') \rightarrow \frac{N_0}{V}$, where V is the system volume. This limiting behavior formally defines off-diagonal long-range order and captures the essence of Bose-Einstein condensation in superfluid systems.

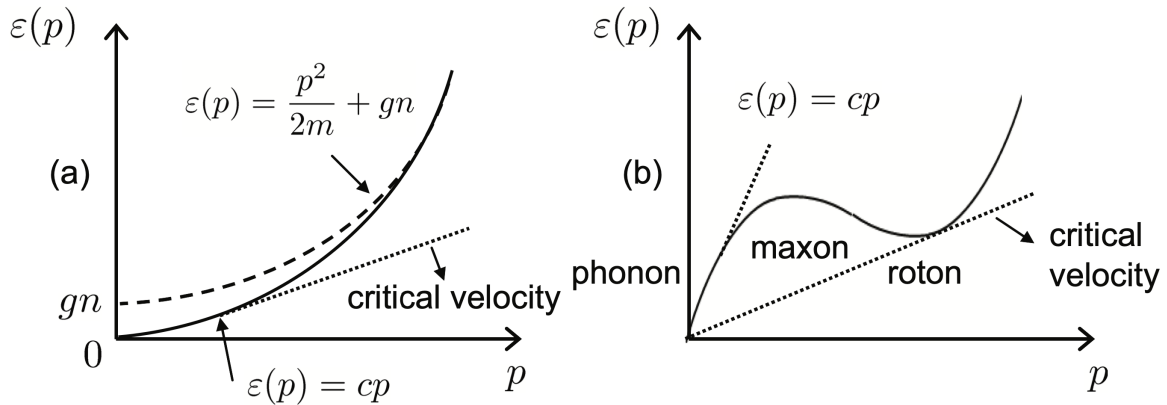


Fig. 1.1 (a) The excitation spectrum for a weakly interacting Bose gas, where the energy $\varepsilon(p)$ is given by $\varepsilon(p) = \frac{p^2}{2m} + gn$ (dashed curve), with a linear phonon-like dispersion $\varepsilon(p) = cp$ (solid line) at low momenta, indicating that the critical velocity v_c is equal to the sound velocity c . (b) The excitation spectrum for a strongly interacting Bose liquid such as ${}^4\text{He}$, showing a more complex structure with phonon, maxon, and roton branches. Here, the critical velocity v_c is less than the sound velocity c , reflecting the presence of a local minimum in the dispersion relation due to roton excitations. Taken from [30].

In uniform two-dimensional systems, conventional off-diagonal long-range order is disrupted by thermal fluctuations at any finite temperature, preventing Bose-Einstein condensation (BEC) in contrast to three-dimensional systems. This phenomenon is explained by the Mermin-Wagner-Hohenberg theorem [33, 34]. However, 2D systems can still form a quasi-condensate and exhibit superfluidity below a critical temperature, known as the Berezinskii–Kosterlitz–Thouless (BKT) phase transition (see Section 1.4) [35, 36]. A proposed phase diagram for a weakly interacting 2D Bose gas shown in figure 1.2 illustrates this behavior [37]. As temperature decreases below a certain point T_{MF} , macroscopic occupation of the ground state occurs, but free vortices remain as primary excitations. With further cooling below the BKT transition temperature T_{BKT} , superfluidity emerges through the pairing of vortices with opposite circulation. This vortex pairing reduces long-range phase fluctuations, allowing for the formation of topological order in the system. At an even lower temperature T_{BEC} , a crossover occurs from the superfluid phase to a true BEC state without free vortex pairs. The details of this phase transition remain an active area of research, with ongoing experimental studies needed to fully understand the scenario presented in the phase diagram.

In one-dimensional (1D) systems with repulsive inter-particle interaction, as in two-dimensional (2D) systems, true off-diagonal long-range order cannot emerge due to the pronounced role of quantum fluctuations. This limitation, resulting from the Mermin-Wagner-

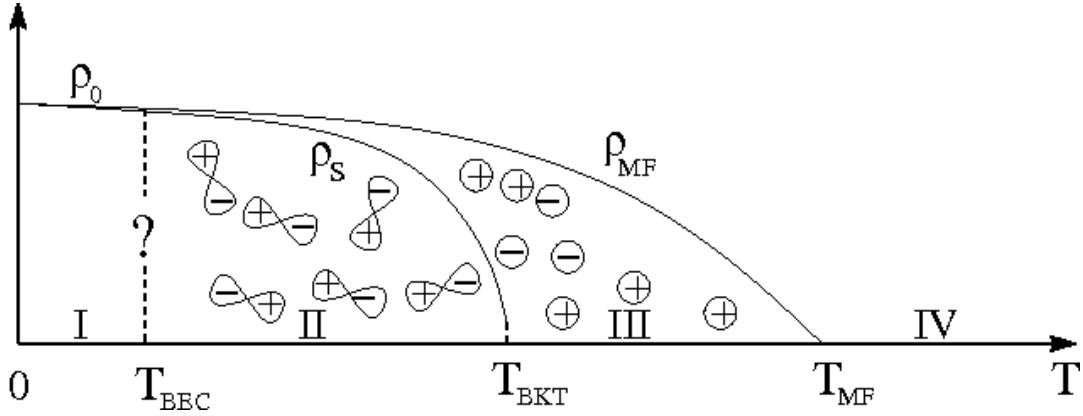


Fig. 1.2 Schematic phase diagram illustrating different phases of a two-dimensional trapped weakly interacting dilute Bose gas as a function of temperature T . Here, ρ_0 represents the density of the condensate, ρ_s denotes the superfluid density, and ρ_{MF} is the mean-field density, estimated through perturbative methods. The temperature T_{BEC} marks the crossover from the superfluid regime to a true Bose-Einstein condensate phase. T_{BKT} indicates the critical temperature of the Berezinskii-Kosterlitz-Thouless (BKT) transition, at which topological order emerges in the form of vortex-antivortex pairs. T_{MF} denotes the onset of the mean-field critical region. Regions I through IV depict different physical regimes: below T_{BEC} (Region I), the system exhibits condensation; between T_{BEC} and T_{BKT} (Region II), it transitions toward a superfluid state; between T_{BKT} and T_{MF} (Region III), the mean-field description becomes increasingly accurate; and above T_{MF} (Region IV), thermal fluctuations dominate [37].

Hohenberg theorem, is particularly severe in 1D, where quantum and thermal fluctuations are even more restrictive. Consequently, unlike in higher dimensions, a true Bose-Einstein Condensate (BEC) cannot form in 1D, not even at absolute zero temperature ($T=0$). Superfluid behavior in 1D is best understood through Luttinger liquid (LL) theory, which describes the low-energy physics of a wide range of interacting 1D systems. In this framework, instead of forming a BEC, particles exhibit quasi-long-range order characterized by correlations that decay algebraically. This quasi-order leads to a power-law decay in the single-particle density matrix, expressed as, $\rho_1(r-r') = \langle \hat{\psi}^\dagger(r) \hat{\psi}(r') \rangle \sim |r-r'|^{-1/2K}$, where K is the LL parameter. The power-law behavior extends to other correlation functions, such as the density-density correlation, with exponents that vary based on the Luttinger parameter K . This parameter, in turn, depends on the particle density and interaction strength, effectively making the exponents tunable [38]. The value of the Luttinger parameter K influences the system's tendency to different types of order at long distances. For instance, the single-component 1D Bose-Hubbard model exhibits two distinct phases: a Mott insulating phase and a superfluid (Luttinger liquid) phase (see Section 1.3). In the superfluid phase, $K > 1$, while at the superfluid-Mott transition, K approaches 1. A unique case arises at the tip of the Mott lobe, where the transition belongs

to the XY universality class [24], and the system undergoes a Berezinskii-Kosterlitz-Thouless (BKT) transition (see Section 1.4) [35, 36], with K approaching 2.

Interestingly, superfluidity is not restricted to bosonic systems. Below the much lower temperature of 3 mK, the fermionic isotope helium-3 (^3He) also exhibits superfluidity. In this case, superfluidity arises from Cooper pairing, a mechanism that enables fermions to behave collectively in a manner analogous to bosons, leading to a superfluid phase. Further insights into superfluidity have been gained through experiments on extremely dilute alkali gases confined in magnetic traps at nanokelvin temperatures. Starting with the observation of BEC in trapped atoms by Weiman, Cornell, and Ketterle in 1995, superfluid behavior has been observed in both bosonic and fermionic atoms within these ultracold atomic gases. Although these systems are not classified as condensed matter (being dilute vapors), they provide valuable experimental platforms to study fundamental aspects of superfluidity and quantum collective behavior.

Having explored the unique properties of superfluidity, we now turn to the Bose-Hubbard model, a foundational framework for understanding quantum phases in lattice systems. The Bose-Hubbard model is a powerful tool for investigating the interplay between particle interactions and mobility within a periodic potential. It is particularly valuable for describing the quantum phase transition between superfluid and Mott insulating states, which arises from the competition between kinetic energy, driving particle delocalization, and on-site interaction, promoting localization. In this section, we will outline the theoretical structure of the Bose-Hubbard model and explore the conditions for the superfluid-Mott insulator transition in one and higher dimensions.

1.3 Bose-Hubbard Model

Typically, models of bosonic systems are employed to describe superfluid states. In the presence of deep periodic potentials, atoms can transition between adjacent potential wells (lattice sites) through quantum tunneling, leading to the development of discrete lattice models. For a system of one-component, spinless bosons, the Bose-Hubbard model described by the Hamiltonian,

$$H = -t \sum_{\langle i,j \rangle} [\hat{b}_i^\dagger \hat{b}_j + \text{H.c.}] + U \sum_i \frac{\hat{n}_i(\hat{n}_i - 1)}{2} - \mu \sum_i \hat{n}_i \quad (1.5)$$

provides a robust framework, characterized by parameters such as the hopping amplitude t , which determines particle mobility within the lattice; the on-site interaction U , capturing local interactions between particles; and the chemical potential μ , which controls the particle density. Here \hat{b}_i and \hat{b}_i^\dagger are the bosonic annihilation and creation operators at lattice site i , and $\hat{n}_i = \hat{b}_i^\dagger \hat{b}_i$

Introduction

is the number operator that counts the bosons at site i . These operators obey the standard bosonic commutation relations: $[\hat{b}_i, \hat{b}_j^\dagger] = \delta_{ij}$ and $[\hat{b}_i, \hat{b}_j] = [\hat{b}_i^\dagger, \hat{b}_j^\dagger] = 0$. Initially introduced in a heuristic manner, this model aimed to distinguish the ground state and low-energy excitations of interacting bosons in a uniform space, capturing the density-dependent transitions between solid and superfluid phases in systems like ^4He [39–42]. Later, the Bose-Hubbard model was derived more formally within the context of solid-state physics [43], inspired by experimental studies of ^4He adsorbed in porous media and Cooper pairs in granular superconductors [24]. This model has since become a foundational tool for exploring phase transitions and the superfluid-insulator dynamics in various quantum systems.

A remarkable feature of the Bose-Hubbard model is its ability to capture the quantum phase transition from a superfluid to a Mott insulator state [24, 19], driven by the competition between kinetic energy t and on-site repulsive interactions U . The model’s ground state is inherently superfluid for any non-integer average filling n of the lattice, regardless of the interaction strength t/U . However, at integer lattice fillings, a quantum phase transition can occur between a weakly interacting superfluid and a strongly interacting Mott insulator. This can be understood as follows: for weak interactions (in the limit $U/t \rightarrow 0$, or $t \gg U$, bosons can move freely across the lattice, leading to a superfluid phase where particles are delocalized. Conversely, in the limit $t/U \rightarrow 0$ (where $U \gg t$), moving a boson to a neighboring site creates an energetically costly configuration, with an empty site and a doubly occupied site. This cost, on the order of U for a single filling $n = 1$, leads to a ground state where bosons are localized at individual lattice sites, resulting in the “Mott insulator” phase. This transition from superfluidity to the Mott insulating state, controlled by the ratio t/U , exemplifies the intricate balance between kinetic and potential energy in quantum systems.

Figure 1.3 presents the ground-state phase diagram of the one-dimensional ($d = 1$) Bose-Hubbard model, mapped in terms of the chemical potential-to-hopping ratio μ/t and the hopping-to-interaction ratio t/U . In the regime of strong interactions ($U \gg t$), the diagram reveals a Mott insulating region where the average lattice filling is an integer. This Mott region is surrounded by the superfluid phase, indicating a transition between localized and delocalized states as the interaction strength decreases relative to the hopping amplitude. In the superfluid phase, the excitation spectrum is gapless, and particle-number statistics follow a broad, Poisson-like distribution. Here, the one-body density matrix (the first-order two-point correlation function) displays off-diagonal long-range order in two and three dimensions and decays as a power law in one dimension. Conversely, in the Mott insulator phase, a finite excitation gap appears, particle-number fluctuations are suppressed, and the one-body density matrix decays exponentially across all dimensions. The superfluid-to-Mott insulator (SF-MI) transition is

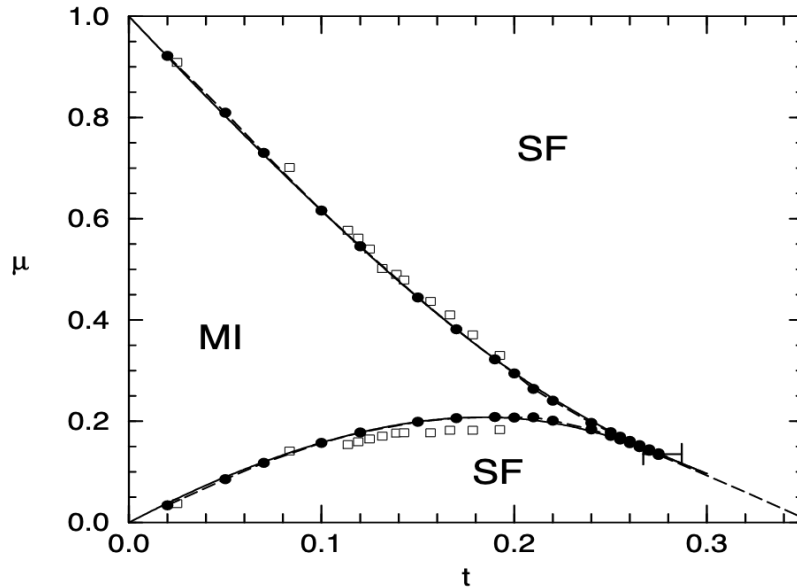


Fig. 1.3 The phase diagram of the one-dimensional Bose-Hubbard model displays the superfluid phase (SF) and the Mott insulator phase (MI) with density one. Solid lines represent a Padé analysis of 12th-order strong-coupling expansions, while the boxed regions indicate Quantum Monte Carlo (QMC) data. Circles denote Density Matrix Renormalization Group (DMRG) results, and dashed lines mark the regions of integer density. The error bars in the μ -direction are smaller than the circles, reflecting minimal uncertainty, while the error bars in the t -direction represent the uncertainty in determining the Berezinskii-Kosterlitz-Thouless (BKT) transition. [44]

described by an $O(2)$ rotor model that captures the dynamics of the condensate phase at fixed density, specifically at the tips of the Mott lobes in the phase diagram in higher dimensions. For $d=1$, instead the fixed density transition is of the Berezinskii-Kosterlitz-Thouless (BKT) type (see section 1.4). Outside these tips, where density fluctuates, the complex condensate density serves as the order parameter, and the transition aligns with the universality class of the dilute Bose gas [19]. Experimental realization of the SF-MI transition has been achieved in optical lattices, initially observed in three dimensions [45] and subsequently in one [46] and two dimensions [47].

Despite significant theoretical progress, a complete description of interacting quantum systems remains challenging. Even the seemingly simple Bose-Hubbard model lacks general analytical solutions, with exact results limited to special cases such as non-interacting or infinitely strong interactions. Approximate solutions, derived through systematic expansions in powers of small parameters, are valuable but inherently limited. Mean-field theory, based on the Gutzwiller ansatz [48], has been crucial in studying the Bose-Hubbard model. This approach

Introduction

considers local fluctuations but neglects inter-site quantum correlations, making it exact in infinite dimensions and insightful for high-dimensional systems, though less accurate in lower dimensions. Efforts to refine mean-field theory by including distance-dependent quantum correlations have led to methods such as random phase approximation [49], cluster Gutzwiller method [50], and dynamical mean-field theory (DMFT). DMFT, originally developed for fermions [51] and later adapted for bosons [52], is among the most successful approaches but is computationally intensive. It can be viewed as an expansion in the inverse coordination number [86], reducing the problem to solving an impurity model on a single site or cluster. This requires robust numerical techniques, including exact diagonalization, density matrix renormalization group (DMRG), and quantum Monte Carlo (QMC), due to the complexity of the computational problem.

Alongside analytical methods, exact numerical approaches have been developed, with exact diagonalization (ED) being the most widely used for systems with a few degrees of freedom. ED involves constructing and diagonalizing the Hamiltonian matrix in a specified basis, enabling precise control over calculation accuracy and providing access to the full energy spectrum. This spectrum forms the basis for simulating time dynamics, as demonstrated in recent studies on few-body systems [53–55]. However, ED is fundamentally constrained by the exponential growth of the Hilbert space with system size, limiting its feasibility to small systems. The largest example reported involves $L = N = 18$, where L and N denote the number of lattice sites and particles, respectively, with a maximum of four particles per site [56]. Although the Hamiltonian matrix is finite for systems with limited degrees of freedom, the “exponential curse”—the exponential increase in Hilbert space with system size—necessitates truncation to manage computational demands. To facilitate ED calculations, several open-source libraries, such as ALPS [57] and QuSpin [58], offer general-purpose solutions, simplifying the setup and execution of ED across various quantum models and enabling researchers to validate results from approximate and other numerical methods.

For larger systems, the density-matrix renormalization group (DMRG) [59, 60] offers a more efficient deterministic approach. DMRG leverages the fact that the system’s state often occupies a small subspace of the Hilbert space. It is quite effective in one dimension, where it can handle larger systems with $N, L \approx 1000$. However, it becomes less practical in higher dimensions and for finite temperature analysis, where quantum Monte Carlo (QMC) methods [61, 10] are preferred. QMC utilizes stochastic sampling to handle stationary states in experimentally realistic settings, accommodating up to $N \sim 10^5$ bosons in a three-dimensional lattice [62]. In this study, we utilize the Worm Algorithm [10], a Path Integral Monte Carlo method exact for unfrustrated bosonic systems, to investigate the ground-state phase diagram

1.4 Berezinskii–Kosterlitz–Thouless (BKT) transition

of a one-dimensional system of bosons with long-range hopping. In the following section, we examine the unique properties of long-range interactions, which can diverge significantly from those of short-range interactions and present intriguing avenues for study.

Building on the foundational insights provided by the Bose-Hubbard model, we now turn to the Berezinskii-Kosterlitz-Thouless (BKT) transition, a topological phase transition that emerges in low-dimensional systems, particularly in the superfluid-insulator transition in one and two dimensions. In these systems, true long-range order is suppressed by the Mermin-Wagner theorem, which prohibits conventional symmetry breaking due to strong fluctuations. The BKT transition is crucial for understanding the superfluid-insulator transition in 1D and 2D lattice systems, where quasi-long-range order arises as vortex-antivortex pairs bind and unbind at the transition point. In this section, we will first analyze the BKT transition through the 2D XY model and then delve into its theoretical mapping to the 2D Coulomb gas and sine-Gordon models. This approach provides a comprehensive view of topological phase transitions in low-dimensional quantum systems and clarifies the critical mechanisms driving phase behavior in the Bose-Hubbard model at low dimensions.

1.4 Berezinskii–Kosterlitz–Thouless (BKT) transition

The Berezinskii-Kosterlitz-Thouless (BKT) transition is a unique type of phase transition that appears in a range of physical systems. It underlies phenomena such as vortex-antivortex unbinding in the 2D XY model, dipole unbinding in the 2D Coulomb gas, metal-insulator transitions in 1D chains, and superfluid-insulator transitions in 1D bosonic systems. Although these phenomena may seem different, they share the same universality class and can be mapped onto one another. Unlike conventional transitions, which involve symmetry breaking—such as ferromagnetic to paramagnetic or liquid to solid—the BKT transition is marked by a shift in topological order. Kosterlitz, Thouless, and Haldane were awarded the Nobel Prize in 2016 for their contributions to understanding this remarkable transition.

A defining characteristic of the BKT transition in 2D systems is its dependence on vortex–antivortex pairs, rather than a conventional order parameter. In a 2D vector spin model, a vortex is a point around which spins rotate in a specific direction, either clockwise or counterclockwise, while an antivortex is a point where spins rotate in the opposite direction. At low temperatures, vortex-antivortex pairs remain bound, resulting in restricted fluctuations and quasi-long-range order, with correlations decaying algebraically. As the temperature reaches the critical BKT temperature, T_{BKT} , thermal energy unbinds these pairs, generating free vortices and causing a phase transition that disrupts quasi long-range order without symmetry breaking.

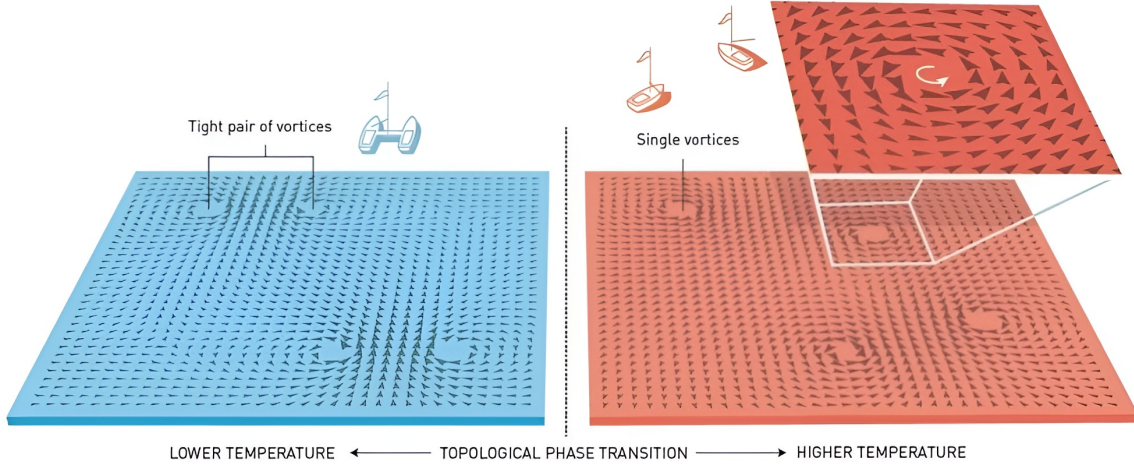


Fig. 1.4 Visualization of the Berezinskii–Kosterlitz–Thouless (BKT) transition: at low temperatures, vortex–antivortex pairs remain bound, maintaining quasi-long-range order. As temperature approaches the critical BKT temperature T_{BKT} , the pairs unbind, creating free vortices that disrupt quasi-ordered system and lead to a phase transition.

For example, in a 2D vector spin model, one finds that the the average magnetization (order parameter in 3D model) remains zero even below T_{BKT} (indicating no true long-range order), while the spin-spin correlation function decays algebraically (quasi long range order). The system’s $O(2)$ symmetry (i.e. turning all spins at their position) remains unbroken at the transition. Above T_{BKT} , the correlation function decays exponentially, marking a transition from quasi-ordered to a disordered phase. This transition, driven by the binding and unbinding of these topological defects (vortices), is illustrated in Fig. 1.4.

The finite-temperature superfluid-to-normal transition in 2D systems (and the 1D superfluid-Mott insulator transition at zero temperature) is governed by the Berezinskii-Kosterlitz-Thouless (BKT) phenomena. This transition results in a characteristic jump in the superfluid density, which drops from a finite value to zero at T_c in 2D. Despite this sharp change, the transition is not first-order, as all thermodynamic quantities remain continuous [63]. Renormalization group analysis by Kosterlitz and Thouless predicts the following behavior near the transition:

$$\rho_s(T) - \rho_s(T_c) \propto \sqrt{T_c - T} \quad (T \leq T_c) \quad (1.6)$$

$$\ln \xi(T) \propto |T_c - T|^{-1/2} \quad (1.7)$$

where ρ_s is the superfluid density, ξ the correlation length, and T_c the critical temperature. The exponential divergence of the correlation length ξ at the critical point ensures that all

1.4 Berezinskii–Kosterlitz–Thouless (BKT) transition

thermodynamic quantities remain continuous across the transition, underscoring the unique nature of the BKT transition.

In subsection 1.4.1, we discuss the BKT transition in the classical XY model, which describes Heisenberg interactions between two-component classical spins on a 2D lattice. This model captures the paramagnetic-ferromagnetic transition in 2D, providing a clear visualization of topological excitations as spin vortices. In subsection 1.4.2, we establish a formal mapping between this model and the 2D Coulomb gas screening transition. This analogy offers insight into how vortices in the XY model disrupt the “quasi-long-range” order of the low-temperature phase in a way similar to how charges screen each other in the Coulomb gas. Finally, we introduce a mapping to the sine-Gordon model, which, while describing a different physical scenario—a quantum field in one dimension—provides additional insight into the behavior of the system.

1.4.1 2D XY model

The Berezinskii-Kosterlitz-Thouless (BKT) transition is fundamentally tied to the behavior of two-dimensional systems where traditional long-range order is prohibited due to strong fluctuations. To understand this unique phase transition, we begin with the XY model—a theoretical framework that has been instrumental in exploring the BKT transition and topological ordering in low-dimensional systems. The XY model describes a 2D lattice of classical spins (rotors), each with a fixed magnitude ($|\mathbf{S}_i| = 1$) and free to rotate in the plane. Unlike the Ising model, where spins are constrained to discrete orientations, the XY model allows continuous angular variation, effectively modeling Heisenberg interactions for two-component spins in a plane. This model is represented by the following Hamiltonian:

$$H_{XY} = -J \sum_{\langle i,j \rangle} \mathbf{S}_i \cdot \mathbf{S}_j = -J \sum_{\langle i,j \rangle} \cos(\theta_i - \theta_j) \quad (1.8)$$

where $\sum_{\langle i,j \rangle}$ denotes a summation over nearest-neighbor spins, J is a positive coupling constant promoting ferromagnetic alignment, and θ_i is the angle that spin i makes with a reference axis. The angle θ_i , often referred to as a “phase” variable, is significant because it highlights the model’s connection to other physical systems, such as superfluids, where phase coherence plays a central role.

The XY model possesses two important symmetries:

1. **A continuous global $U(1)$ symmetry:** $\forall i, \theta_i \rightarrow \theta_i + c$, where c is a constant shift across all spins, reflecting the model’s invariance under uniform phase rotations.

Introduction

2. **A discrete local Z_n symmetry:** $\theta_i \rightarrow \theta_i + 2\pi n$, allowing phase shifts by integer multiples of 2π at each site.

These symmetries are essential to the model's phase behavior and play a defining role in the BKT transition (to be seen later), influencing the formation and dynamics of topological defects and the system's response to thermal fluctuations.

At low temperature, the difference in phase between neighboring spins is very small, so that we can rewrite the Hamiltonian (1.8) by expanding the cosine up to the second order in its argument.

$$H_{XY} = -J \sum_{\langle i,j \rangle} \left[1 - \frac{1}{2}(\theta_i - \theta_j)^2 + O((\theta_i - \theta_j)^4) \right] \quad (1.9)$$

Using a continuum approximation for small fluctuations in θ , such that the quantities of the order $(\theta_i - \theta_j)^4$ are negligible, the Hamiltonian can be approximated as,

$$H_{XY} \approx \frac{J}{2} \int d^2r (\nabla\theta(r))^2 = \frac{J}{2} \int \frac{dq}{(2\pi)^2} q^2 |\theta_q|^2 \quad (1.10)$$

where the scalar field $\theta(r)$ labels the angles of rotors at each point in the plane, $\nabla\theta(r)$ represents the phase gradient, and θ_q denotes the Fourier component of θ at wavevector q . $E_0 = -2JN$ is the energy of the system when all N rotors are aligned. This expression captures the energy associated with phase fluctuations in the system.

We begin by examining the global $U(1)$ symmetry. The minimum energy configuration corresponds to a situation when all spins are aligned in a single direction, say $\theta_i = 0$ for all spins, effectively breaking the $U(1)$ symmetry of the Hamiltonian. In such a fully aligned state, the system would exhibit finite macroscopic magnetization. However, the Mermin-Wagner theorem forbids spontaneous symmetry breaking of continuous symmetries in two-dimensional systems at finite temperature.

At finite temperatures, the phase θ_i at each site fluctuates around its ground-state value due to thermal effects. These phase fluctuations prevent the formation of macroscopic magnetization in the thermodynamic limit. Specifically, in the low-temperature phase, the expectation value of the magnetization, $\langle S_i \rangle$, is given by:

$$\langle S_i \rangle = e^{-\frac{T}{4\pi J} \ln(\frac{L}{a})} = \left(\frac{a}{L}\right)^{\frac{T}{4\pi J}} \xrightarrow{L \rightarrow \infty} 0, \quad (1.11)$$

where T is the temperature, L is the system's linear size, and a is the lattice spacing between neighboring spins. Thus, as L grows, the expectation value of the magnetization vanishes, preventing true long-range order in the thermodynamic limit (see [64] for further details). It

1.4 Berezinskii–Kosterlitz–Thouless (BKT) transition

is worth noting, however, that real systems sometimes do not reach the thermodynamic limit and may display finite magnetization at low temperatures. In other words, the observation of spontaneous symmetry breaking in a finite system does not imply a violation of the Mermin-Wagner theorem, but rather that the system is sufficiently far from the thermodynamic limit.

While a conventional order parameter is absent (with $\langle S_i \rangle = 0$ at any finite temperature), the spin correlation function reveals a transition between low- and high-temperature phases. The correlation function between two spins at sites i and j is defined as:

$$C(\mathbf{r}_i - \mathbf{r}_j) = \langle \mathbf{S}_i \cdot \mathbf{S}_j \rangle = \langle \cos(\theta_i - \theta_j) \rangle. \quad (1.12)$$

At low temperatures ($\beta J \ll 1$), using the approximated Gaussian Hamiltonian 1.10, the spin correlation function is given by

$$C(r) = \left\langle e^{i(\theta(r) - \theta(0))} \right\rangle = e^{-\frac{1}{2} \langle (\theta(r) - \theta(0))^2 \rangle} = e^{-\frac{T}{2\pi J} \ln(r/a)} = \left(\frac{a}{r} \right)^{\frac{T}{2\pi J}}. \quad (1.13)$$

This result shows that the correlation function decays algebraically with distance r , a hallmark of quasi-long-range order in the low-temperature phase. However, for high-temperature regime ($\beta J \gg 1$), one cannot make the assumption of small fluctuations in neighboring spins, and therefore spin correlation function has to be estimated using the full cosine structure of Hamiltonian 1.8. The correlation function estimated in this manner (see [65] for detailed calculations) is given by

$$C(\mathbf{r}_i - \mathbf{r}_j) \simeq e^{-|\mathbf{r}_i - \mathbf{r}_j|/\xi}, \quad \xi = \ln \frac{2T}{J}. \quad (1.14)$$

Thus, at high temperatures, the correlation function decays exponentially, with a correlation length ξ that depends on temperature.

For reference, we consider the results from standard Landau theory for a second-order phase transition. Below the critical temperature T_c , the correlation function is given by:

$$C(r) \approx m^2 + B e^{-r/\xi_-}, \quad T < T_c, \quad (1.15)$$

where $m = \langle S \rangle$ is the average order parameter. Above T_c , the correlation function takes the form:

$$C(r) \approx A e^{-r/\xi_+}, \quad T > T_c. \quad (1.16)$$

Introduction

Here, the correlation lengths ξ_+ and ξ_- diverge as T approaches T_c :

$$\xi_{\pm}(T) \sim \frac{1}{|T - T_c|^{\nu}}, \quad T \rightarrow T_c, \quad (1.17)$$

with $\nu = 1/2$ in mean-field theory. Thus, in the disordered phase, the correlation function decays to zero, while in the ordered phase, it decays to the square of the order parameter, m^2 .

In contrast, the results obtained for the XY model show significant differences. At high temperatures, we observe an exponential decay to zero, as in Eq. 1.14, but the correlation length does not diverge at any finite temperature. In the low-temperature regime, Eq. 1.13 shows that the correlation function decays algebraically with a power law rather than exponentially, suggesting $\xi \rightarrow \infty$ in the ordered state. This behavior aligns with the Mermin-Wagner theorem, as there is no finite-temperature order parameter. The sharp difference in correlation behavior between low and high temperatures thus signifies a phase transition, marked not by a non-zero order parameter, but by a shift in the scaling behavior of the correlation functions. At low temperatures, spin fluctuations (spin waves) display finite phase stiffness, reflected in the coefficient of the $(\nabla\theta)^2$ term in Eq. 1.10. This rigidity against phase fluctuations leads to the power-law decay of correlations in 1.13. Conversely, at high temperatures, the Hamiltonian's full cosine interaction recovers an exponential decay (1.14), and phase rigidity is lost. To fully understand this transition the role of vortices must be examined.

While going from original Hamiltonian 1.8 to approximated one 1.10, we have lost discrete local Z_n symmetry,

$$\theta_i \rightarrow \theta_i + 2\pi n \quad (1.18)$$

where $n \in \mathbb{Z}$, of the original XY model.

The presence of this discrete symmetry introduces a new type of phase excitations that are topological in nature and cannot be smoothly connected to the unperturbed ground state [64]. These excitations, known as vortices, are characterized by a phase winding of $\pm 2\pi$ around their center:

$$\oint \nabla\theta \cdot d\ell = 2\pi n. \quad (1.19)$$

The existence of a vortex invalidates the assumption of smooth phase variations between neighboring sites. As such, vortices are likely candidates responsible for driving the phase transition in the system. A critical question, then, is the energy required to introduce a vortex, as this determines the temperature scale at which vortex proliferation—and consequently, the phase transition—occurs. To estimate the energy cost of introducing vortices, we consider configurations $\theta(r)$ that include both smooth solutions θ_{SW} , representing longitudinal spin

1.4 Berezinskii–Kosterlitz–Thouless (BKT) transition

waves, and singular solutions θ_V (representing vortices), where the phase is allowed to be discontinuous at a point r_0 .

These solutions are obtained by applying a variational principle to the Hamiltonian 1.10, leading to the general equation $\delta H = 0$. This variational equation yields:

$$\nabla^2 \theta_{\text{SW}}(r) = 0, \quad (1.20)$$

for smooth spin waves throughout space, while vortices satisfy:

$$\nabla^2 \theta_V(r) = 2\pi q \delta(r - r_0), \quad (1.21)$$

where $q \in \mathbb{Z}$ is the vorticity of the topological excitation at r_0 . For a vortex with $q = 1$, the solution in 2D is:

$$\theta_V = \arctan \frac{y - y_0}{x - x_0}. \quad (1.22)$$

The energy associated with a vortex is then calculated by inserting this solution into the Hamiltonian 1.10, giving:

$$E = \pi J \ln \frac{L}{a}, \quad (1.23)$$

where a is the lattice spacing, and L is the system size. This logarithmic divergence with L shows that single vortices are energetically costly, disfavoring their existence in the thermodynamic limit at low temperatures.

However, at finite temperatures, we must also consider the entropy gain associated with forming vortices. The number of possible independent vortex locations scales as $(L/a)^2$, leading to an entropy contribution:

$$S = 2 \ln \frac{L}{a}. \quad (1.24)$$

The free energy F of a vortex configuration combines the energy and entropy contributions:

$$F = E - TS = \pi J \ln \frac{L}{a} - 2T \ln \frac{L}{a} = (\pi J - 2T) \ln \frac{L}{a}. \quad (1.25)$$

This expression shows that at temperatures $T > T_{\text{BKT}} = \pi J/2$, the entropy gain from creating vortices outweighs the energy cost, making vortex proliferation favorable and leading to a phase transition. The estimate of the transition temperature assumed a single, infinitely large vortex; however, in reality, the situation is more complex, with multiple vortex excitations

Introduction

typically occurring at shorter scales. For instance, if a vortex is located at r_+ and an antivortex with opposite vorticity at r_- , then at distances greater than $|r_+ - r_-|$, the phase configuration of the system remains essentially unaffected. This leads to a natural cutoff of the logarithmic divergence of the integral at a scale on the order of $|r_+ - r_-|$. This cutoff implies that such vortex “pairs” are energetically viable even below T_c and can alter the effective large-distance coupling J that determines the transition temperature.

1.4.2 Mapping of 2D XY model to 2D coulomb gas and 1D sine-Gordon model

To fully capture the transition dynamics, it’s crucial to account for vortex interactions, as Kosterlitz did in [66]. The Hamiltonian governing these vortex interactions is equivalent to that of a two-dimensional Coulomb gas [65]. In this analogy, each vortex in the 2D XY model represents a “charge,” where a vortex and an antivortex (with opposite phase winding) act as positive and negative charges, respectively. The interaction energy between two vortices at positions r_i and r_j , with vorticities q_i and q_j (where $q = \pm 1$), is analogous to the 2D Coulomb interaction:

$$E_{ij} = -\pi J q_i q_j \ln \frac{|r_i - r_j|}{a}. \quad (1.26)$$

For a system with multiple vortices, the total energy of a system of vortices is given by

$$H = -\pi J \sum_{i \neq j} q_i q_j \ln \left(\frac{|\vec{r}_i - \vec{r}_j|}{a} \right) + \mu \sum_i |q_i|, \quad (1.27)$$

where $\mu = \pi^2 J / 2$ is the vortex-core energy. Here, the first term describes interaction between vortices, and second term stands for sum of core energies. In this Coulomb gas model, vortices interact logarithmically, with the system obeying a global charge neutrality condition

$$\sum_i q_i = 0, \quad (1.28)$$

indicating that vortices and antivortices appear in equal numbers, forming bound pairs below the transition temperature. This pairing underlies the phase behavior characteristic of the low-temperature phase in the BKT transition. Below T_{BKT} , vortices and antivortices form tightly bound pairs, corresponding to a low-temperature “dielectric” phase where the system shows quasi-long-range order with algebraically decaying correlations. Above T_{BKT} , unbound vortices appear, leading to a “metallic” phase in the Coulomb gas analogy, where charges are

1.4 Berezinskii–Kosterlitz–Thouless (BKT) transition

free to move and screen each other. This screening behavior disrupts the quasi-long-range order and results in an exponential decay of correlations.

Using the neutrality condition, the partition function for the vortex system can be derived (see [64, 67] for details). For a system consisting of N vortex-antivortex pairs, the partition function takes the form:

$$Z = \sum_{N=1}^{\infty} \frac{1}{(N!)^2} y_0^N \int D\vec{r} \exp \left[\beta \pi J \sum_{i \neq j} q_i q_j \ln \left(\frac{|\vec{r}_i - \vec{r}_j|}{a} \right) \right] \quad (1.29)$$

where $y_0 = e^{-\beta\mu}$ is the fugacity associated with the vortex core energy μ .

This vortex system can be equivalently mapped to the sine-Gordon model, a quantum field theory where vortex and spin-wave excitations are represented as cosine potentials. For a 1D chain of length L , the sine-Gordon Hamiltonian is given by:

$$H_{\text{SG}} = \frac{v_s}{2\pi} \int_0^L dx \left(K(\partial_x \theta)^2 + \frac{1}{K}(\partial_x \phi)^2 - \frac{2g}{a^2} \cos(2\phi) \right) \quad (1.30)$$

where θ and $\partial_x \phi$ are canonically conjugated variables satisfying $[\theta(x'), \partial_x \phi(x)] = i\pi \delta(x' - x)$. Here, K is the Luttinger liquid (LL) parameter, v_s the velocity of 1D fermions, and g defines the strength of the sine-Gordon potential [68]. In this formulation, the role of the spin angle or phase is played by the field θ .

The partition function for ϕ assumes a similar form to Equation 1.29. Upon integrating over θ , the partition function for ϕ can be written as:

$$Z = \int D\phi e^{-W} \sum_{l=0}^{\infty} \frac{1}{n!} \int d\vec{r}_1 \cdots d\vec{r}_n \left(\frac{g}{2\pi} \right)^n \cos(2\phi(\vec{r}_1)) \cdots \cos(2\phi(\vec{r}_n)) \quad (1.31)$$

where

$$W = \frac{K}{2\pi} \int dx (\partial_x \theta)^2 \quad (1.32)$$

By decomposing cosines into exponential functions,

$$\cos(2\phi(\vec{r}_i)) = \frac{e^{2i\phi(\vec{r}_i)} + e^{-2i\phi(\vec{r}_i)}}{2} = \sum_{\varepsilon=\pm 1} \frac{e^{2i\varepsilon\phi(\vec{r}_i)}}{2} \quad (1.33)$$

and evaluating the partition function, we observe that it essentially involves averaging over exponential functions with Gaussian weights:

$$\left\langle \exp \left(2i \sum_i \varepsilon_i \phi(\vec{r}_i) \right) \right\rangle = \exp \left[2K \sum_{i < j} \varepsilon_i \varepsilon_j \ln \left(\frac{r_{ij}}{a} \right) \right] \quad (1.34)$$

The resulting partition function, with appropriate modifications of dummy variables, is expressed as:

$$Z = \sum_{N=1}^{\infty} \frac{1}{(N!)^2} \left(\frac{g}{2\pi} \right)^N \int D\vec{r} \exp \left[2K \sum_{i < j} \ln \left(\frac{|\vec{r}_i - \vec{r}_j|}{a} \right) \right] \quad (1.35)$$

By comparing equations 1.29 and 1.35, it becomes clear that the partition function of the sine-Gordon model shares the same structural form as the partition function of an interacting system of vortices, or equivalently, a 2D Coulomb gas, with the following parameter mappings:

$$K = \frac{\pi J}{T} \quad \text{and} \quad g = 2\pi e^{-\beta\mu}. \quad (1.36)$$

However, while the equations are formally equivalent, they describe distinct physical systems. In the one-dimensional case, we consider a quantum phase transition in $1 + 1$ dimensions, reflecting how the properties of a one-dimensional Luttinger liquid are modified by the interaction term controlled by g . Generally, as g increases, the ϕ field becomes confined within one of the minima of the $\cos(\phi)$ term, resulting in a “massive” field. Consequently, the correlation function of the Luttinger liquid loses the characteristic power-law decay of the “massless” phase, leading the system to transition into an ordered state, potentially exhibiting spin or charge order.

This mapping highlights an important insight: in the XY model, the vortex core energy μ is fundamentally linked to the interaction coupling constant J . After mapping to the sine-Gordon model, however, the core energy is governed by the strength g of the sine-Gordon potential, which can now be treated as a tunable parameter to fit the vortex core energy.

1.5 Long-range interactions

Long-range interacting systems refer to systems in which the interaction strength decays slowly with distance, often following a power-law $1/r^\alpha$, where r is the distance between microscopic elements and decay exponent α is small enough. Unlike short-range interactions, where effects are localized, long-range interactions influence the system globally, leading to collective behavior and complex, nontrivial dynamics. For the purpose of our study, we will use the classification of long-range systems based on decay exponent α proposed by [9].

For classical systems in d spatial dimensions, a key distinction arises depending on whether $\alpha < d$ or $\alpha > d$. To understand the distinction between these two regimes, we calculate the interaction energy ε of a particle placed at the centre of a d -dimensional sphere of radius R , interacting through a long-range interaction potential $V(r) \propto \mathcal{J}/r^\alpha$, where α determines the decay rate and \mathcal{J} is the coupling constant. Assuming a homogeneous particle distribution and excluding particles within a small radius δ around the center, the interaction energy is given by,

$$\varepsilon = \frac{\rho \mathcal{J} \Omega_d}{d - \alpha} \left(R^{d-\alpha} - \delta^{d-\alpha} \right), \quad (1.37)$$

where ρ is the density (such as charge, particle, or mass density), Ω_d is the d -dimensional solid angle, and $\alpha \neq d$ to avoid divergence. When the sphere radius R is allowed to grow, the energy ε remains finite if $\alpha > d$. In this regime, the total energy $E = V\varepsilon$ scales linearly with the volume size $V \propto R^d$, meaning the system is extensive. However, if the potential decays too slowly (i.e., $\alpha < d$), the total energy grows superlinearly with the volume at constant density, violating extensivity. Specifically, for $\alpha < d$, the energy ε diverges with the volume according to $V^{1-\alpha/d}$, and the system loses the property of additive energy [69]. Physically, this implies that when two identical copies of the system are placed adjacent to each other, interface energy becomes significant, leading to a non-linear scaling of energy with volume V [70]. This scenario corresponds to the *strong long-range regime*, where conventional definitions of internal energy become non-extensive, and traditional thermodynamics fail to apply. Such properties characterize a broad class of physical systems, including gravitational and plasma models [9]. Furthermore, the behavior of strong long-range systems extends to mesoscopic systems, where the interaction range, even if finite, is comparable to the system size, deviating from the thermodynamic limit.

While it is evident that long-range interactions significantly influence the physics of the system in the strong long-range regime, they can also affect the system's behavior for $\alpha > d$, though in a less pronounced manner. A key result for classical systems with power-law interactions [71] is that if α exceeds the critical threshold value α_* , then the critical behaviour becomes indistinguishable from that of a short-range model. The exact value of α_* depends on the specific system and the nature of phase transition under consideration. In the intermediate range when $d < \alpha < \alpha_*$, the energy is extensive yet long-range nature of the couplings affects the long-distance properties of the system. This intermediate region, known as the *weak long-range regime*, is the focus of our analysis, where we explore this regime in the extended Bose-Hubbard model with power-law hopping in 1D (see Chapters 3 and 4).

Introduction

Beyond the question of extensivity, a fundamental distinction between the strong and weak long-range regimes appears in their dynamical properties. Specifically, for $\alpha < d$, the thermalization timescale diverges with the system size N . Systems governed by gravitational interactions [72–74], for example, are known to become trapped in non-thermal quasi-stationary states, with lifetimes that increase with the number of particles, as seen in the Chandrasekhar relaxation timescale for stellar systems, which scales as $N/\ln N$ [75]. In contrast, while thermalization in the weak long-range regime resembles that of short-range systems, the non-local nature of interactions influences information propagation [76–78, 2], can lead to breaking of conformal symmetry [79, 80], breakdown of the MerminWagner theorem [33], and the emergence of new topological phases and phase transitions [79, 81, 82].

Symmetry is fundamental in physics, shaping system behavior across scales. Symmetries that are present at a system’s microscopic level can undergo spontaneous breaking at lower temperatures, giving rise to phases like crystals and magnets [83]. Sometimes, however, new symmetries emerge at low energies—known as emergent symmetry—even if absent at the microscopic level, as seen in materials like $\text{Li}_{0.9}\text{Mo}_6\text{O}_{17}$ [84]. At critical points in classical short-range models in two and three dimensions, scale invariance is often enhanced to a broader conformal symmetry (CS). This expanded symmetry includes not only scale invariance but also translations, rotations, and special conformal transformations that combine translations with spatial inversions [85, 86]. In 2D systems, CS allows exact solutions and predictions due to its infinite-dimensional nature [87], although it becomes finite-dimensional ($SO(d+1, 1)$) in higher dimensions, limiting analytical methods [88, 89]. Nevertheless, numerical studies in both two and three dimensions provide strong evidence for CS in short-range models, underscoring its role in describing universal features at critical points across dimensions [90–92]. In long-range models, a key question is whether their critical points exhibit conformal symmetry (CS) and how the interaction range influences this symmetry. As $\alpha \rightarrow \infty$, short-range models and their CS at criticality are recovered, so the key issue is to identify the values of α up to which CS persists. This is linked to a related question of identifying upper limit of α ($\alpha_* = d + \sigma_*$) at which critical exponents of short-range reappear [69, 71]. For instance, classical spin systems with long-range couplings exhibit the same critical exponents as short-range models for $\sigma > \sigma_*$, while for $d/2 < \sigma \leq \sigma_*$ distinct long-range exponents appear [69, 71]. Studies on the Kitaev chain with long-range pairings suggest that for $\alpha > 2$, CS remains intact, but for $\alpha < 2$, long-range interactions break CS, altering correlation behavior while preserving short-range critical exponents [80]. Exploring how long-range interactions influence CS and critical exponents remains an active research area [9].

In quantum mechanics, information propagation is fundamentally constrained by the Lieb-Robinson bound. This bound limits the speed at which information, correlations, and disturbances can propagate in systems with local interactions, defining an effective "light cone" where correlations decay exponentially outside the causal region [93–95]. However, in systems with long-range interactions, the picture is substantially altered since the traditional definition of group velocity does not apply, enabling correlations, information or entanglement to spread faster than the Lieb-Robinson bound predicts, often violating locality [78]. Experiments with trapped-ion quantum simulators have demonstrated violations of the local Lieb-Robinson bound for $0.6 \lesssim \alpha \lesssim 1.2$ [3, 2]. For example, Jurcevic et al. [3] observed accelerated correlation spread in a 15-ion chain under a long-range XY Hamiltonian, while Richerme et al. [2] noted propagation velocities exceeding the Lieb-Robinson limit in systems with long-range Ising and XY interactions. This faster propagation is due to direct coupling between distant particles, which can enable rapid information transfer and efficient quantum state preparation [9]. Most of our current understanding of correlations and entanglement in presence of long-range interactions has been based on insights on prototypical systems [76, 96, 77, 97, 98]. This research has produced a general qualitative framework for understanding propagation in long-range systems, which applies across a variety of models, observables, and interaction decay rates α :

1. High α ($\alpha \gg 3$): The system behaves similarly to a short-range system, with correlations confined within a light cone where they spread linearly over time.
2. Intermediate α : Correlations still exhibit light-cone-like behavior at shorter distances, but propagate faster over larger distances, distorting the light cone. This regime highlights the crossover between purely local and strongly long-range behavior.
3. Low α : The light cone concept breaks down entirely, allowing correlations to propagate faster than any defined group velocity.

Extending the Lieb-Robinson theorem to systems with power-law interactions poses significant challenges [99]. Hastings and Koma generalized the bound for long-range systems, but it fails to capture propagation dynamics accurately for large α [100]. Further refinements, like those proposed by Gong et al. [101], aim to tighten these bounds across different α values, though achieving a universally applicable bound remains an open area of research [102–104, 9].

1.6 Outline of the results

The central aim of this thesis is to investigate the ground state properties of strongly correlated bosonic systems with power-law decaying long-range hopping interactions.

Introduction

In Chapter 2, the working principles of the quantum Monte Carlo (QMC) methods are presented. First, we outline the fundamental concepts of classical Monte Carlo methods in Section 2.1. We then discuss the quantum Path Integral Monte Carlo (PIMC) method and the associated worm algorithm for lattice systems in Section 2.2. This modern approach offers an efficient way to obtain exact numerical results for many-body systems without approximations, with the only limitation being statistical uncertainties, which can be minimized given sufficient computation time.

In Chapter 3, I investigate the disorder-induced quantum phase transition between superfluid and insulating states of one-dimensional (1D) bosonic particles. Specifically, I explore hard-core bosons with a hopping interaction that decays with distance as $1/r^\alpha$, resembling an XY model with power-law couplings. Traditionally, such transitions in one-dimensional systems are expected to follow the Berezinskii-Kosterlitz-Thouless (BKT) transition, but my study reveals a non-BKT continuous phase transition for $\alpha \leq 3$. Using large-scale Quantum Monte Carlo simulations, I demonstrate that for $\alpha \leq 3$, the superfluid-to-insulator transition shows scale-invariant behavior—a characteristic of continuous phase transitions in higher dimensions rather than the expected BKT scenario. I determined the phase diagram for different values of the exponent α , and found that the disorder strength required to disrupt superfluidity decreases with increasing α reaching zero for $\alpha > 3$, indicating that the superfluid phase becomes unstable under infinitesimal disorder in the short-range hopping limit.

In Chapter 4, I focus on understanding the interaction-induced phase transition behavior of a one-dimensional Bose-Hubbard model with power-law hopping interactions. By tuning the decay exponent, α , and the ratio t/U (where t represents the hopping amplitude and U the on-site repulsion), I aim to explore the nature of the quantum phase transition when moving from a superfluid to a Mott insulator phase at a fixed density. For $1 < \alpha \leq 3$, the interaction-driven quantum phase transition from superfluid to Mott insulator at unit filling emerges as continuous and scale-invariant, deviating from the BKT framework, which applies only when $\alpha > 3$ — mirroring the disorder-induced transition findings of Chapter 3. Using large scale Quantum Monte Carlo simulations, I examined both the phase boundaries and the critical exponents that characterize the transition. Specifically, I study the effects of different α values on the behavior of the single-particle density matrix $G(\ell)$ which helps in understanding the presence of long-range or quasi-long-range order in the superfluid phase. My analysis reveals that for $\alpha \leq 2$, $G(\ell)$ exhibits a plateau at large distances, consistent with long-range order. This is further reflected in the condensate fraction, which attains a constant value, confirming the presence of long-range coherence. However, for $\alpha > 2$, $G(\ell)$ decays as a power law, aligning with quasi-long-range order, showing that the system's coherence properties are sensitive to the

interaction range. For $2 < \alpha \leq 3$, the system behaves in a way that bridges one-dimensional and higher-dimensional systems, displaying unique critical behavior and quasi-long-range order. The phase diagram in the $t/U - \mu/U$ plane reveals that as α decreases, the Mott insulating regions shrink, transitioning from pointed to more rounded lobes, indicating a dimensional crossover.

Overall, this research provides a foundation for experimental studies on systems like cold atoms, trapped ions, and Rydberg atoms, where power-law interactions can be engineered. It contributes a new benchmark in understanding one-dimensional systems with long-range interactions, particularly how dimensionality and long-range hopping impact quantum phase transitions.

Chapter 2

Quantum Monte Carlo Methods

Quantum Monte Carlo (QMC) methods are a natural extension of classical Monte Carlo techniques, adapted to solve quantum mechanical problems. The key distinction lies in the preliminary effort required to convert quantum degrees of freedom into a form that can be sampled classically, often through techniques like path integrals [105] or auxiliary fields [106]. This transformation encapsulates the quantum nature of the system, manifesting not only in explicit features like the non-commutativity of quantum operators and the symmetrization or antisymmetrization of the wavefunction but also in more subtle aspects such as the emergence of the sign problem [107]. This chapter provides a concise overview of the numerical techniques employed to derive the results presented in Chapters 3 and 4. We will outline the fundamental concepts of classical Monte Carlo methods in Section 2.1, which serve as the foundation for our discussion. In Section 2.2, we begin with an introduction to the Path Integral Monte Carlo (PIMC) method for quantum statistical physics. Following this, we delve into the Worm Algorithm, an advanced PIMC update technique renowned for its numerical exactness in simulating bosonic lattice systems.

2.1 Monte Carlo methods

Monte Carlo methods are a class of computational algorithms that rely on *random sampling* to obtain numerical results. They are particularly useful for problems with vast phase spaces, where deterministic approaches are either impractical or impossible—such as in high-dimensional integrals. The core idea is straightforward: by randomly sampling points within a d -dimensional volume, we can estimate an integral at the price of statistical error. However, the challenge lies in selecting these random samples strategically to minimize computational cost.

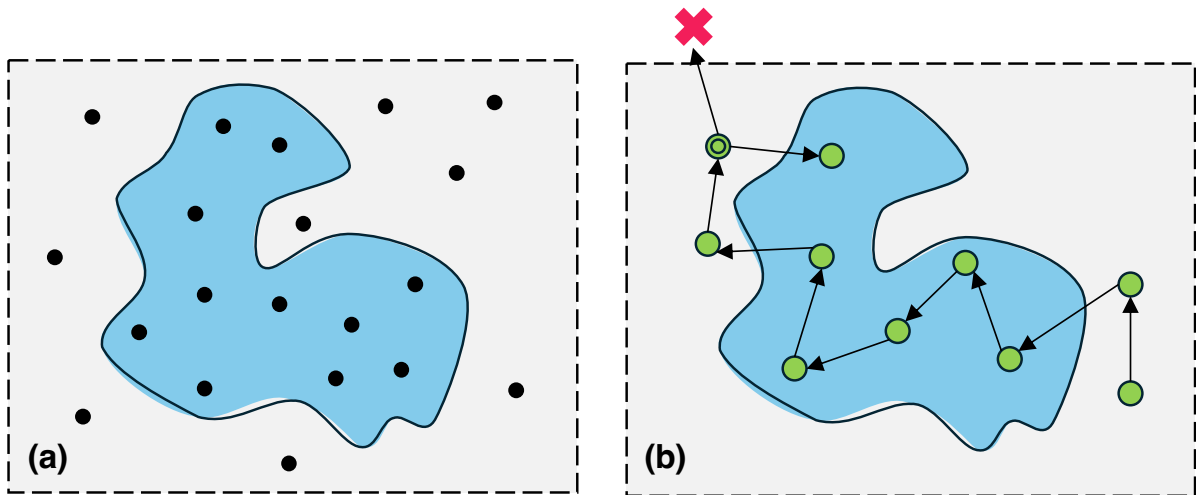


Fig. 2.1 Illustration of Monte Carlo integration to estimate the unknown area of a pond enclosed by a rectangle of known area A . (a) Direct sampling — random points are uniformly scattered across the entire rectangle. (b) Markov chain Monte Carlo sampling — a chain of correlated samples gradually explores the pond’s area, with each new point dependent on the previous one. The crossed-out point indicates an invalid step that was rejected.

To illustrate the sampling process, imagine you’re standing in a large field, trying to determine how much of it is covered by a pond [108]. After enclosing the pond with a rectangle of known area, one approach would be to randomly throw pebbles across the enclosed area and observe how many land in the pond. The ratio of pebbles that land in the pond to the total number of throws gives an estimate of the pond’s area. This technique is illustrated in figure 2.1(a) and is known as *direct sampling* in Monte Carlo methods—simple, unbiased, and based purely on chance. Importantly, each pebble’s position is independent of the others, and the more pebbles you throw, the more accurate your estimate becomes.

If, however, the pond is very large, randomly throwing pebbles from a fixed position becomes impossible. To explore the area more effectively, a targeted strategy like Markov Chain Monte Carlo (MCMC) is necessary. Instead of randomly scattering pebbles across the entire field, you start at a random position and throw a pebble in a random direction. After each throw, you walk to the new location and repeat the process. If a pebble lands outside the rectangular boundary, you reject the move and stay in the same spot, ensuring that the principle of detailed balance (discussed later) is maintained, making the Markov chain reversible. Over time, the pebbles will spread across the rectangular area, with clusters near the boundaries where moves were rejected. This technique is illustrated in figure 2.1(b) and reflects the logic of MCMC—a step-by-step, guided exploration where each new position is based on

the previous one. By focusing on areas of interest, such as the pond, this method enhances sampling efficiency, particularly in complex or high-dimensional spaces.

In a similar manner, random sampling of a function can be carried out to compute an estimate of its integral. To illustrate the Monte Carlo approach to numerical integration, let us try to integrate the one-dimensional function $f(x)$ from a to b :

$$F = \int_a^b f(x)dx. \quad (2.1)$$

The basic idea behind Monte Carlo integration is to estimate the integral by averaging the function's values over a set of random points uniformly distributed over the integration range. To do this, we generate N random samples (x_1, x_2, \dots, x_N) uniformly in the interval $[a, b]$. The Monte Carlo estimator for computing F using N samples is given by

$$F_N = \frac{b-a}{N} \sum_{i=1}^N f(x_i). \quad (2.2)$$

Here, $(b-a)/N$ represents the width of each subinterval if the samples were evenly spaced, but since we are using random points, this factor scales the average value of the function over the sampled points. As N increases, the estimate becomes more accurate due to the *Law of Large Numbers*, and for sufficiently large N , the Monte Carlo estimator converges to the true value of the integral, i.e., $\lim_{N \rightarrow \infty} F_N = F$. We could have easily computed this integral by standard integration methods like trapezoidal or Simpson's rule which converge much faster in one dimension. However, these standard methods suffer from the curse of dimensionality where the convergence rate becomes exponentially worse with increased dimensions and error scales as $\sim N^{-\kappa/d}$ [108], where N represents the number of subdivisions of the integration interval, d is the dimensionality of the integral, and κ is a method-specific constant. In contrast, the error in the Monte Carlo estimator decreases as $F_N \propto 1/\sqrt{N}$, independent of the dimensionality. This scaling makes Monte Carlo methods exceptionally useful for estimating integrals in high-dimensional spaces, where traditional methods become computationally prohibitive.

The general problem these methods aim to solve is determining the expectation value of an operator $A(\mathbf{x})$ over a probability distribution $\pi(\mathbf{x})$. To estimate the expectation value of an operator A with respect to a probability distribution $\pi(\mathbf{x})$, where \mathbf{x} is an n -dimensional vector, i.e., $\mathbf{x} \in \mathbb{R}^n$, we start by defining the expectation value. The expectation value of an operator A with respect to $\pi(\mathbf{x})$ is given by

$$\langle A \rangle = \int A(\mathbf{x}) \pi(\mathbf{x}) d\mathbf{x}. \quad (2.3)$$

Quantum Monte Carlo Methods

In the Monte Carlo approach, we approximate this integral by drawing N samples \mathbf{x}_i from the distribution $\pi(\mathbf{x})$. The expectation value $\langle A \rangle$ can then be estimated as

$$\langle A \rangle \approx \frac{1}{N} \sum_{i=1}^N A(\mathbf{x}_i), \quad (2.4)$$

where \mathbf{x}_i are independent random samples drawn from $\pi(\mathbf{x})$.

The Monte Carlo estimate of $\langle A \rangle$ has a statistical error that decreases as the number of samples N increases. The standard error of the mean for the Monte Carlo estimate is

$$\sigma_{\langle A \rangle} \approx \frac{\sigma_A}{\sqrt{N}}, \quad (2.5)$$

where σ_A is the standard deviation of $A(\mathbf{x})$ under the distribution $\pi(\mathbf{x})$:

$$\sigma_A = \sqrt{\langle A^2 \rangle - \langle A \rangle^2} = \sqrt{\int A(\mathbf{x})^2 \pi(\mathbf{x}) d\mathbf{x} - \left(\int A(\mathbf{x}) \pi(\mathbf{x}) d\mathbf{x} \right)^2}. \quad (2.6)$$

As $N \rightarrow \infty$, the Monte Carlo estimate converges to the true expectation value $\langle A \rangle$ due to the law of large numbers:

$$\lim_{N \rightarrow \infty} \frac{1}{N} \sum_{i=1}^N A(\mathbf{x}_i) = \langle A \rangle. \quad (2.7)$$

In summary, by generating samples from $\pi(\mathbf{x})$ and evaluating $A(\mathbf{x})$ at these sampled points, we can estimate $\langle A \rangle$ efficiently, with a statistical error that decreases with \sqrt{N} . This approach is particularly useful when direct integration is infeasible.

The key distinction between direct sampling and Markov Chain Monte Carlo (MCMC) methods lies in how the set of samples $\{\mathbf{x}_i\}$ is generated. In direct sampling, samples are drawn independently from the probability distribution $\pi(\mathbf{x})$, ensuring that each sample directly reflects the target distribution. In contrast, MCMC methods create a Markov chain that generates samples in a way such that the distribution $\pi(\mathbf{x})$ serves as the chain's equilibrium distribution, meaning that, as the chain progresses, the distribution of the generated samples converges to $\pi(\mathbf{x})$.

To understand MCMC further, we start by defining a Markov chain on a discrete set of states S as a sequence $X_1, X_2, X_3, \dots \in S$, where each transition $X_t \rightarrow X_{t+1}$ is independent of prior transitions except the immediate preceding state. This property is called the *Markov property*, where the state X_{t+1} depends only on X_t and not on any earlier states. Mathematically,

this property is expressed as

$$P(X_{t+1} = x | X_1, X_2, \dots, X_t) = P(X_{t+1} = x | X_t). \quad (2.8)$$

The transition probabilities of the chain are encoded in a *transition matrix* T , where each element $T_{\mu\nu} = P(\mu \rightarrow \nu) = P(X_{t+1} = \nu | X_t = \mu)$ represents the probability of moving from state μ to state ν in a single step. For a valid Markov process, these transition probabilities must be time-invariant, depend only on the current states μ and ν and satisfy the constraint

$$\sum_{\nu} T_{\mu\nu} = 1 \quad (2.9)$$

for each state μ .

For a Markov chain to have π as its equilibrium distribution it must meet the following conditions:

1. **Ergodicity:** From any starting state, it should be possible to reach any other state within a finite number of steps. This ensures the chain doesn't get "stuck" in one part of the state space and can explore the entire set of possible states.
2. **Balance:** The distribution π should be stable, meaning the flow of probability into each state balances the flow out of that state. This is called the "balance" condition and is expressed as:

$$\sum_{\nu} p_{\mu} P(\mu \rightarrow \nu) = \sum_{\nu} p_{\nu} P(\nu \rightarrow \mu). \quad (2.10)$$

where $p_{\mu} \equiv \pi(\mu)$ is the probability of state μ , and $P(\mu \rightarrow \nu) \equiv T_{\mu\nu}$ is the one-step transition probability from μ to ν . Simplifying using the sum rule, Eq. 2.9, we get

$$p_{\mu} = \sum_{\nu} p_{\nu} P(\nu \rightarrow \mu) \quad (2.11)$$

for each state μ .

Sometimes, instead of balance, a stricter condition called "Detailed Balance" is used:

3. **Detailed Balance:** This condition requires that the probability flow from μ to ν is exactly matched by the flow from ν to μ . This means:

$$p_{\mu} P(\mu \rightarrow \nu) = p_{\nu} P(\nu \rightarrow \mu) \quad (2.12)$$

Quantum Monte Carlo Methods

for all pairs of states μ and ν . Detailed balance ensures equilibrium by making sure there's no net flow between any two states.

If a Markov chain meets these conditions, it will converge to π over time. In MCMC, we design a Markov chain with transition probabilities so that the distribution converges to π . After running the chain for a certain number of steps (the *burn-in* period), the generated samples can be considered as draws from $\pi(\mathbf{x})$. This allows us to sample from π even if we don't know it explicitly.

A common method for constructing such a Markov chain is the *Metropolis-Hastings algorithm* [109, 110], where we generate a candidate state \mathbf{x}' from a proposal distribution $q(\mathbf{x}'|\mathbf{x}_t)$ based on the current state \mathbf{x}_t . The candidate state is then accepted with a probability α defined by

$$\alpha = \min \left(1, \frac{\pi(\mathbf{x}')q(\mathbf{x}_t|\mathbf{x}')}{\pi(\mathbf{x}_t)q(\mathbf{x}'|\mathbf{x}_t)} \right). \quad (2.13)$$

If the candidate is accepted, $\mathbf{x}_{t+1} = \mathbf{x}'$; otherwise, the chain remains at \mathbf{x}_t , so $\mathbf{x}_{t+1} = \mathbf{x}_t$. This accept-reject mechanism ensures that the chain will eventually produce samples distributed according to $\pi(\mathbf{x})$, even if direct sampling is not possible.

MCMC methods are widely used in statistical physics, where the goal is to compute expectation values of physical observables, such as energy, magnetization, specific heat, and other measurable quantities. These expectation values are derived from the partition function, which encapsulates the statistical properties of a system. For a system with Hamiltonian H , the partition function Z in the canonical ensemble (where the temperature T is fixed) is given by

$$Z = \text{Tr}[e^{-\beta H}], \quad (2.14)$$

where $\beta = \frac{1}{k_B T}$ is the inverse temperature, and k_B is the Boltzmann constant.

To compute the thermal average (or expectation value) of an observable O , we use the following formula:

$$\langle O \rangle = \frac{1}{Z} \sum_{\text{states}} O_i e^{-\beta E_i}, \quad (2.15)$$

where E_i is the energy of state i , and the sum is taken over all possible states of the system. The factor $e^{-\beta E_i}$ is the Boltzmann weight, which assigns a higher probability to lower-energy states at a given temperature. The partition function Z acts as a normalizing factor, ensuring that the sum of probabilities over all states is 1. This formalism allows us to calculate physical observables by averaging them across all possible states, each weighted by its Boltzmann factor $e^{-\beta E_i}$.

In practice, direct evaluation of this sum is often infeasible for large systems due to the exponential growth of possible states. MCMC methods address this by generating a representative sample of states according to their Boltzmann weights, enabling efficient computation of thermal averages without summing over every state explicitly.

In the next section, we introduce the Path Integral Monte Carlo (PIMC) approach, which extends MCMC methods to quantum statistical physics. We then explore the Worm Algorithm, an advanced PIMC update technique that enables efficient sampling of states and highly accurate calculation of off-diagonal observables, such as Green's functions.

2.2 Path Integral Monte Carlo methods

Path Integral Monte Carlo (PIMC) methods represent a specialized class of quantum Monte Carlo (QMC) algorithms that utilize a worldline graphical representation to compute the partition function Z . These methods rely on the imaginary time path integral formalism, a powerful framework for quantum statistical calculations. This formalism is especially useful in finite-temperature quantum systems, as it allows for a systematic treatment of quantum fluctuations and thermal effects by mapping the quantum system onto a classical system in an additional imaginary time dimension.

Consider a Hamiltonian H with exact eigenvalues E_i and eigenfunctions ψ_i . In thermal equilibrium, the probability of a given state i being occupied is $e^{-E_i/k_B T}$, where $\beta = \frac{1}{k_B T}$ represents the inverse temperature (with k_B being the Boltzmann constant and T the temperature). Using this formalism, the thermodynamic expectation value of an observable O for a general quantum system is given by:

$$\langle O \rangle = Z^{-1} \sum_i \langle \psi_i | O | \psi_i \rangle e^{-\beta E_i} = \frac{\text{Tr} \left(O e^{-\beta H} \right)}{Z}, \quad (2.16)$$

where $\rho = e^{-\beta H}$ is the statistical operator, and Z is the partition function, defined as $Z = \text{Tr} \left(e^{-\beta H} \right)$. The partition function Z serves as a normalization factor and encapsulates the statistical properties of the system at thermal equilibrium. To facilitate numerical calculations, the Hamiltonian H is often decomposed into two parts:

$$H = H_0 + V \quad (2.17)$$

Quantum Monte Carlo Methods

where H_0 is diagonal in the computational basis, while V being off-diagonal induces transitions between different basis states. The computational basis is specifically the Fock basis, defined by the set of occupation numbers for each lattice site, $\{|n_1, \dots, n_{N_{sites}}\rangle\}$, where N_{sites} denotes the total number of sites, and $n_j \in \mathbb{Z}_{\geq 0} = \{0, 1, 2, \dots\}$ represents any non-negative integer. The diagonal part H_0 typically includes contributions from terms like the chemical potential and the potential energy, which do not induce state transitions. In contrast, V involves hopping or interaction terms that enable particles to move between different states or lattice sites, thus altering the basis state.

In this formalism, the statistical operator $\rho = e^{-\beta H}$ can be related to the Matsubara evolution operator σ in the interaction picture. Specifically, we can write:

$$\rho = e^{-\beta H} = e^{-\beta H_0} \sigma, \quad (2.18)$$

where σ is given by the series expansion:

$$\begin{aligned} \sigma &= 1 - \int_0^\beta d\tau V(\tau) + \dots + (-1)^m \int_0^\beta d\tau_m \dots \int_0^{\tau_2} d\tau_1 V(\tau_m) \dots V(\tau_1) + \dots \\ &= \sum_{m=0}^{\infty} (-1)^m \int_{0 < \tau_1 < \dots < \tau_m < \beta} d\tau_m \dots d\tau_1 V(\tau_m) \dots V(\tau_1) \end{aligned} \quad (2.19)$$

where $V(\tau) = e^{\tau H_0} V e^{-\tau H_0}$ is the interaction potential in imaginary time τ . By introducing complete sets of states $I = \sum_\psi |\psi\rangle \langle \psi|$ between each non-diagonal operator, we can expand the partition function Z as follows,

$$\begin{aligned} Z(\beta) &= \text{Tr} \rho \\ &= \sum_{m=0}^{\infty} (-1)^m \int_{0 < \tau_1 < \dots < \tau_m < \beta} d\tau_m \dots d\tau_1 \langle \psi_0 | e^{-\beta H_0} V(\tau_m) | \psi_{m-1} \rangle \\ &\quad \times \langle \psi_{m-1} | V(\tau_{m-1}) | \psi_{m-2} \rangle \dots \langle \psi_1 | V(\tau_1) | \psi_0 \rangle \end{aligned} \quad (2.20)$$

This expansion provides a systematic way to express partition function Z as a series of integrals over imaginary time. Using the notation E_k for the eigen values of H_0 in the eigenstate $|\psi_k\rangle$, such that $E_k = \langle \psi_k | H_0 | \psi_k \rangle$, each matrix element in above equation becomes

$$\langle \psi_k | V(\tau) | \psi_l \rangle = \langle \psi_k | e^{\tau H_0} V e^{-\tau H_0} | \psi_l \rangle = e^{\tau E_k} \langle \psi_k | V | \psi_l \rangle e^{-\tau E_l} \quad (2.21)$$

With this we can rewrite the partition function as

$$Z(\beta) = \sum_{m=0}^{\infty} (-1)^m \int_{0 < \tau_1 < \dots < \tau_m < \beta} d\tau_m \dots d\tau_1 e^{-(\beta + \tau_1 - \tau_m)E_0} \langle \psi_0 | V | \psi_{m-1} \rangle \times e^{-(\tau_m - \tau_{m-1})E_{m-1}} \langle \psi_{m-1} | V | \psi_{m-2} \rangle \dots e^{-(\tau_2 - \tau_1)E_1} \langle \psi_1 | V | \psi_0 \rangle \quad (2.22)$$

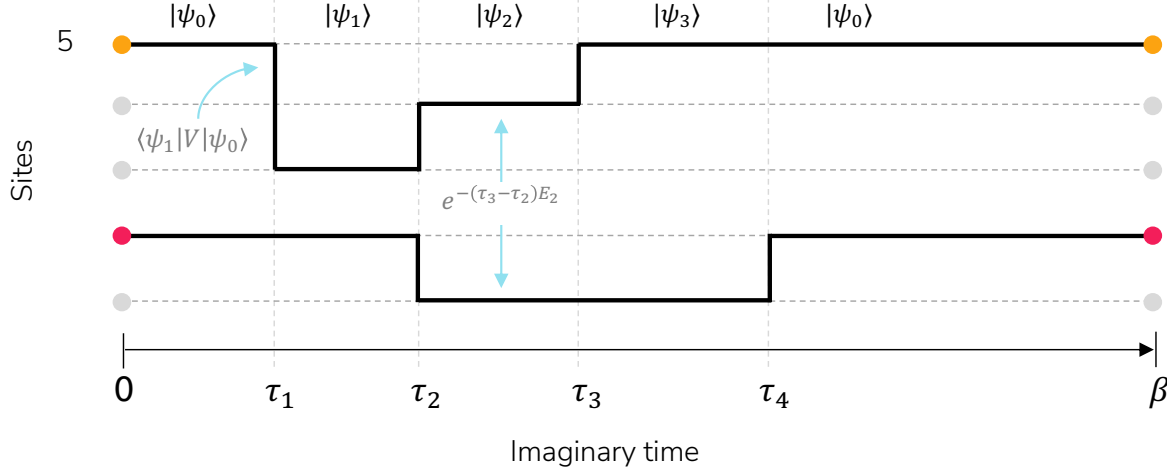


Fig. 2.2 A worldline representation of a term in the partition function from Eq. (1), illustrating state evolution across lattice sites in imaginary time. The horizontal axis spans imaginary time from 0 to β , with discrete time points τ_1 through τ_4 marking instances of state transitions. The vertical axis represents different lattice sites. The system begins in state $|\psi_0\rangle$ at imaginary time $\tau = 0$, evolves to $|\psi_3\rangle$ at time τ_3 , and subsequently returns to $|\psi_0\rangle$. Bold horizontal lines indicate imaginary time evolution of states, while vertical jumps signify transitions between states. Off-diagonal Hamiltonian terms, such as $\langle \psi_1 | V | \psi_0 \rangle$, enable these transitions, while exponential terms like $e^{-(\tau_3 - \tau_2)E_2}$ describe imaginary-time evolution governed by diagonal components of the Hamiltonian.

This expression allows us to visualize the partition function as a sum over configurations of *worldlines*. In this context, the off-diagonal terms in the Hamiltonian (e.g., $\langle \psi_m | V | \psi_{m-1} \rangle$) correspond to hopping of particles between different sites happening at times $0 < \tau_1 < \dots < \tau_m < \beta$. Meanwhile, the diagonal terms (e.g., $e^{-(\tau_m - \tau_{m-1})V E_{m-1}}$) describe the evolution of the system in imaginary time. Thus, each term in this expansion contributes to a particular "worldline" configuration in imaginary time, where transitions between states are punctuated by intervals of diagonal evolution. For instance, Figure 2.2 shows worldline representation of

2.2 Path Integral Monte Carlo methods

The total partition function is obtained by summing over all possible configurations of the system, and is expressed as,

$$\begin{aligned}
 Z &= \sum_{\psi_i} \underbrace{\langle \psi_i | e^{-\beta H_0} | \psi_i \rangle}_{\text{weight}} \\
 &\quad - \sum_{\psi_i} \sum_{\psi_{i'}} \int_0^\beta d\tau_1 \underbrace{\langle \psi_i | e^{-(\beta-\tau_1)H_0} | \psi_{i'} \rangle \langle \psi_{i'} | V e^{-\tau_1 H_0} | \psi_i \rangle}_{\text{weight}} \\
 &\quad + \sum_{\psi_i} \sum_{\psi_{i'}} \sum_{\psi_{i''}} \dots
 \end{aligned} \tag{2.24}$$

In this context, worldlines represent the paths that particles trace in imaginary time. Due to the expansion in Equation 2.24, these worldlines are periodic in imaginary time, meaning that a configuration starting in state $|\psi_0\rangle$ at $\tau = 0$ must return to the same state at $\tau = \beta$. For systems with periodic boundary conditions, the worldlines are also periodic in the spatial dimensions, allowing them to wrap around the spatial boundaries multiple times. As we will demonstrate, the winding numbers—representing the number of times worldlines wind around the system—are directly related to the estimator for superfluid density. An example of a configuration with winding number $\mathcal{W} = 1$ is shown in Fig. 2.3.

To streamline the notation, we define a configuration C_m of order m as a sequence of m states $\{|\psi_0\rangle, |\psi_2\rangle, \dots, |\psi_{m-1}\rangle\}$ along with a corresponding set of times $\{\tau_1, \dots, \tau_m\}$. We associate with each configuration a weight,

$$\begin{aligned}
 W(C_m) &= W(\psi_0, \dots, \psi_{m-1}, \tau_1, \dots, \tau_m) \\
 &= e^{-(\beta + \tau_1 - \tau_m)E_0} \langle \psi_0 | V | \psi_{m-1} \rangle \\
 &\quad \times e^{-(\tau_m - \tau_{m-1})E_{m-1}} \langle \psi_{m-1} | V | \psi_{m-2} \rangle \\
 &\quad \times \dots e^{-(\tau_2 - \tau_1)E_1} \langle \psi_1 | V | \psi_0 \rangle
 \end{aligned} \tag{2.25}$$

This weight $W(C_m)$ represents the contribution of each configuration to the partition function. Consequently, the expansion of the partition function in Eq. 2.24 can be interpreted as a sum over the weights of all possible configurations. The partition function Z can therefore be expressed as,

$$Z(\beta) = \sum_{m=0}^{\infty} \sum_{C_m} W(C_m). \tag{2.26}$$

The thermodynamic expectation value of an observable O can then be calculated as follows

$$\langle O \rangle = \frac{1}{Z} \text{Tr} \left(O e^{-\beta H} \right) = \frac{1}{Z} \sum_{m=0}^{\infty} \sum_{C_m} \langle O \rangle_{C_m} W(C_m), \quad (2.27)$$

where $\langle O \rangle_{C_m}$ denotes the imaginary-time average of the observable O for a given configuration C_m .

Expectation values, as shown in Eq. 2.27, can be evaluated using Monte Carlo methods by stochastically sampling configurations C_m from the distribution $W(C_m)/Z$. This is typically achieved using various algorithms, with Markov Chain Monte Carlo (MCMC) sampling being especially effective for generating the desired configurations. In the following, we will discuss the *worm algorithm*, an MCMC based Path Integral Monte Carlo method which is numerically exact¹ for unfrustrated bosonic systems.

2.2.1 Worm Algorithm

The worm algorithm, first introduced by Prokof'ev, Svistunov, and Tupitsyn in [10], is a scheme of performing updates of PIMC configurations. It is among the earliest Path Integral Monte Carlo (PIMC) methods capable of efficiently calculating the imaginary time dependent Green's function in large systems. The algorithm accomplishes this by extending the configuration space from the physical partition-function space Z to a Green's function space \mathcal{G} , introducing a discontinuity within the worldlines. This enables the direct sampling of Green's functions alongside the partition function.

The Green's function in the expanded space is defined as,

$$\mathcal{G} = \text{Tr} \left\{ T_{\tau} \left(\hat{b}_i^{\dagger}(\tau_M) \hat{b}_j(\tau_I) e^{-\beta H} \right) \right\} \quad (2.28)$$

where T_{τ} is the time-ordering operator in imaginary time, and the operators $\hat{b}_i^{\dagger}(\tau_M)$ and $\hat{b}_j(\tau_I)$ correspond to creation and annihilation at two points of discontinuity. These discontinuities in the worldline are referred to as *Masha* and *Ira*, representing the two endpoints, or "worm heads," of the disconnected segments in the extended configuration. The algorithm is named the "worm algorithm" because these disconnected worldline segments visually resemble the shape of a worm.

The worm algorithm operates on the principle of utilizing the worm heads, within the extended Green's function space \mathcal{G} to more efficiently sample a variety of configurations in

¹The uncertainty in the estimated expectation values arises solely from stochastic error due to finite sampling. This error is known to decrease as $1/\sqrt{m}$, where m is the number of samples.

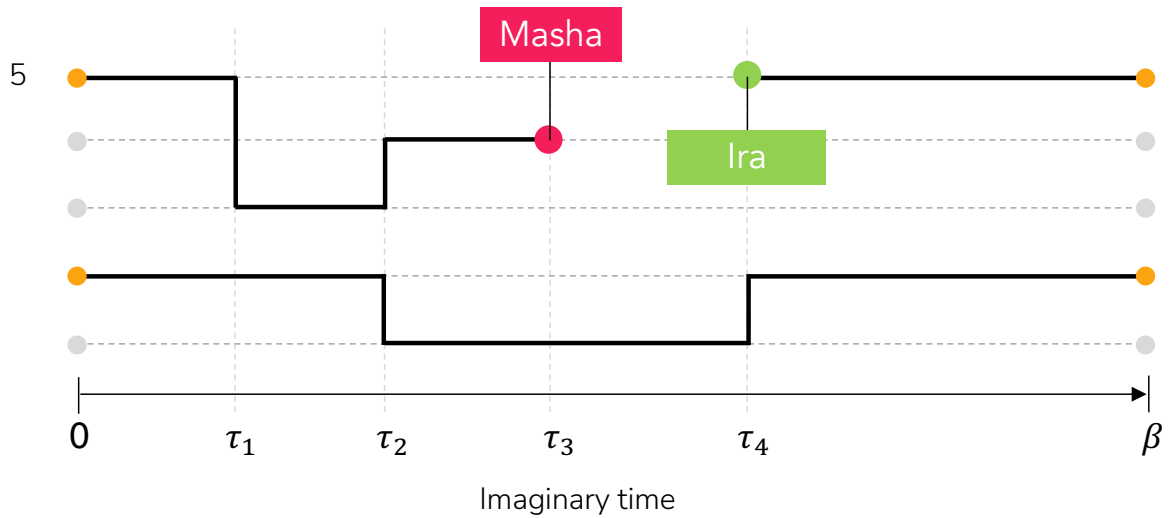


Fig. 2.4 Graphical representation of an extended worldline configuration in the \mathcal{G} sector which includes the worm heads named *Ira* (green) and *Masha* (red).

the partition-function space Z . This approach is implemented through a series of Monte Carlo moves, which include:

1. **Opening and Closing the Discontinuity:** This move introduces or removes a discontinuity in the worldline, thereby switching between configurations in the Z and \mathcal{G} spaces. Opening the discontinuity corresponds to creating a worm by adding the two worm heads (*Masha* and *Ira*) at a chosen site and time, while closing the discontinuity merges the heads to return the configuration to the partition function space.
2. **Moving a Worm Head in Imaginary Time:** This move enables the worm heads to traverse in imaginary time, altering the configuration while maintaining the discontinuity. This also allows adjustments in the number of particles and the length of the worldline.
3. **Moving a Worm Head in Space:** This move enables one worm head to hop along spatial dimensions, allowing for the insertion or removal of kinks in the worldlines.

Through these moves, the worm algorithm performs a random walk in the configuration space, sampling both physical and Green's function configurations according to their respective weights. This random walk follows a Markov Chain, ensuring that the resulting samples represent an equilibrium distribution which in this case is the Boltzmann distribution. Figure 2.4 illustrates an example of a disconnected worldline with worm heads, named *Ira* and *Masha*. The update process begins by selecting the location these two heads and opening the path, thus transitioning to a configuration in the \mathcal{G} sector. The worm heads then move through

space and imaginary time, altering the configuration until they eventually meet at the same site and time. At this convergence point, the discontinuity is closed, returning the configuration to the \mathcal{L} space, where thermodynamic expectation values of physical observables can be computed. The algorithm's capacity to efficiently sample configurations with discontinuities is particularly important in systems exhibiting superfluidity where particle correlations play a crucial role. Remarkably, the worm algorithm is a local Metropolis-based method but exhibits an efficiency comparable to, or even exceeding, that of cluster algorithms at critical points. It avoids the problem of critical slowing down, making it exceptionally useful in simulations near phase transitions. Furthermore, it is capable of generating winding loops around the system, supporting efficient simulations of off-diagonal correlations, grand canonical ensembles, disordered systems, and other complex configurations [111].

2.2.2 Observables

In this subsection, we outline the types of observables that can be directly measured using Path Integral Monte Carlo (PIMC) methods. These observables include quantities such as particle density, energy, and superfluid density, which are evaluated within the Z sector. Additionally, we discuss observables like the one-body density matrix and dynamic structure factor, which are statistically estimated using configurations in the \mathcal{G} sector. Collectively, these quantities provide deep insights into the properties and behavior of quantum systems.

1. **Density:** The density at a specific site j is an important observable, often represented by the expectation value of the density operator n_j . For a given configuration C_n , the density $n_j(C_n)$ can be computed by summing over all time intervals within the configuration. The time intervals are decided based on kinks produced by off-diagonal Hamiltonian terms. This is expressed as:

$$n_j(C_n) = \frac{1}{\beta} \sum_{k=1}^n \langle \psi_k | n_j | \psi_k \rangle (\tau_k - \tau_{k-1}), \quad (2.29)$$

where β is the inverse temperature, and $t_k - t_{k-1}$ represents the duration of each time interval between successive time points t_{k-1} and t_k within the configuration. Here, $\langle \psi_k | n_j | \psi_k \rangle$ gives the matrix element of the density operator at site j for the state $|\psi_k\rangle$ in the configuration, thus allowing us to compute the average occupancy at that site over the imaginary-time path.

2. **Energy:** The total energy $E = \langle H \rangle$ of a configuration C_n is derived from the sum of the potential energy U and the kinetic energy K . The kinetic energy K is estimated by

counting the number of hopping events (or transitions) in the configuration, as each hop corresponds to kinetic energy contributions from the Hamiltonian's off-diagonal terms. The potential energy U , on the other hand, is calculated by considering the contributions from the Hamiltonian's diagonal elements, represented by H_0 . The potential energy for a configuration C_n is given by:

$$U(C_n) = \frac{1}{\beta} \sum_{k=1}^n \langle \psi_k | H_0 | \psi_k \rangle (\tau_k - \tau_{k-1}), \quad (2.30)$$

where $\langle \psi_k | H_0 | \psi_k \rangle$ is the matrix element of the potential energy operator in state $|\psi_k\rangle$ at time τ_k .

3. **Superfluid Density:** The superfluid density ρ_s is a crucial observable for characterizing quantum phases like superfluidity. Estimators for ρ_s depend on the form of the hopping term in the Hamiltonian H_1 and the dimensionality of the system. Detailed derivations of these estimators can be found in [112]. In two-dimensional systems with uniform nearest-neighbor hopping of strength t , the superfluid density is intimately connected to the fluctuations of the winding numbers in the path integral representation. These winding numbers arise due to the periodic boundary conditions imposed on the system and reflect the topological properties of particle trajectories in imaginary time.

The estimator for the superfluid density is given by:

$$\rho_s = \frac{1}{4t\beta} \langle W_x^2 + W_y^2 \rangle,$$

where W_x and W_y are the winding numbers along the x and y spatial dimensions, and $\langle \dots \rangle$ denotes the expectation value over all configurations. The winding numbers W_x and W_y quantify the net number of times particles wrap around the system in each spatial direction due to the periodic boundaries. Physically, large fluctuations in these winding numbers indicate the presence of long-range phase coherence—a hallmark of the superfluid phase. Thus, by measuring ρ_s , we gain direct insight into the superfluid properties of the system.

4. **Density-Density Correlation Function:** Correlation functions are fundamental tools for understanding spatial and temporal correlations in quantum systems. They reveal how particles at different sites or times influence each other, shedding light on phenomena like ordering, excitations, and collective behavior. The density-density correlation function S_{ij} measures the correlation between particle densities at sites i and j :

$$S_{ij} = \langle n_i n_j \rangle,$$

where n_i and n_j are the particle number operators at sites i and j , respectively. In PIMC simulations, an estimator for S_{ij} for a single configuration C_n is calculated as:

$$S_{ij}(C_n) = \frac{1}{\beta} \sum_{k=1}^n \langle \psi_k | n_i | \psi_k \rangle \langle \psi_k | n_j | \psi_k \rangle (\tau_k - \tau_{k-1}),$$

where $\langle \psi_k | n_i | \psi_k \rangle$ is the expectation value of the number operator at site i in state $|\psi_k\rangle$, and the sum runs over all segments k of the worldline configuration C_n .

This estimator effectively averages the product of local densities over imaginary time, weighted by the duration of each state. By accumulating these contributions over many sampled configurations, one obtains an accurate estimate of S_{ij} , revealing how particle densities at different sites are correlated.

5. **One-Body Density Matrix:** The one-body density matrix $\mathcal{G}(\ell)$ characterizes the off-diagonal long-range order in the system, which is essential for understanding quantum coherence and superfluidity:

$$\mathcal{G}(\ell) = \langle \hat{b}_i^\dagger \hat{b}_{i+\ell} \rangle,$$

In the worm algorithm framework, the one-body density matrix is efficiently estimated using configurations in the \mathcal{G} sector. The discontinuities introduced by the worm heads (Masha and Ira) allow for direct sampling of off-diagonal correlation functions. By tracking how the worm propagates through space and imaginary time, one can compute $\mathcal{G}(\ell)$ and thus gain insights into the coherence properties of the system.

6. **Dynamic Structure Factor:** The dynamic structure factor $S(\mathbf{k}, \omega)$ provides information about the excitations and response of the system to external perturbations, as a function of momentum \mathbf{k} and frequency ω :

$$S(\mathbf{q}, \omega) = \int_{-\infty}^{\infty} dt e^{i\omega t} \sum_{i,j} e^{-i\mathbf{q} \cdot (\mathbf{r}_i - \mathbf{r}_j)} \langle n_i(t) n_j(0) \rangle,$$

where $n_i(t)$ is the density operator at site i and time t , \mathbf{r}_i and \mathbf{r}_j are the position vectors of sites i and j . The sum over i, j and the time integral capture spatial and temporal

correlations. In PIMC simulations, direct calculation of $S(\mathbf{q}, \omega)$ is challenging due to the analytic continuation required from imaginary to real time. However, one can compute its imaginary-time counterpart:

$$S(\mathbf{q}, \tau) = \sum_{i,j} e^{-i\mathbf{q}\cdot(\mathbf{r}_i - \mathbf{r}_j)} \langle n_i(\tau) n_j(0) \rangle,$$

which can then be analytically continued to obtain $S(\mathbf{q}, \omega)$ using methods like the method of consistent constraints [113, 114]. This allows the study of excitation spectra and dynamic properties within the PIMC framework.

By measuring these observables, PIMC methods provide a powerful toolkit for investigating the rich physics of quantum many-body systems. The ability to compute quantities in both the Z and \mathcal{L} sectors enables comprehensive analyses of both diagonal and off-diagonal properties, essential for understanding phenomena like superfluidity, Bose-Einstein condensation, and quantum phase transitions.

Chapter 3

Scale invariant phase transition of disordered bosons in one dimension

The disorder-induced quantum phase transition between superfluid and non-superfluid states of bosonic particles in one dimension is generally expected to be of the Berezinskii-Kosterlitz-Thouless (BKT) type. Here, we show that hard-core lattice bosons with power-law hopping decaying with distance as $1/r^\alpha$ with finite integral over space – corresponding in spin language to a XY model with power-law couplings – undergo a non-BKT continuous phase transition instead. We use exact quantum Monte-Carlo methods to determine the phase diagram for different values of the exponent α , focusing on the regime $\alpha > 2$. We find that the scaling of the superfluid stiffness with the system size is scale-invariant at the transition point for any $\alpha \leq 3$ – a behavior incompatible with the BKT scenario and typical of continuous phase transitions in higher dimension. By scaling analysis near the transition point, we find that our data are consistent with a correlation length exponent satisfying the Harris bound $\nu \geq 2$ and demonstrate a new universal behavior of disordered bosons in one dimension. For $\alpha > 3$ our data are consistent with a BKT scenario where the liquid is pinned by infinitesimal disorder.

Bosonic particles with local interactions in one dimension (1D) are described by a universal harmonic theory, known as Luttinger liquid (LL). The latter corresponds to quantized superfluid hydrodynamics (including instantons) and is fully characterized by the superfluid velocity, $v = \sqrt{Y_s/\kappa}$, and LL parameter, $K = \pi\sqrt{\kappa Y_s}$, with κ the compressibility and Y_s the superfluid stiffness. Diagonal disorder induces an instability in LL towards a non-superfluid Bose glass (BG) phase – a compressible insulator displaying exponential decay of off-diagonal correlations. In their seminal paper [6], Giamarchi and Schulz found by means of a perturbative renormalization group (RG) analysis that the LL-BG transition is of the Berezinskii-Kosterlitz-Thouless (BKT) type that takes place at the universal value $K = K_c = 3/2$ (this result holds at

Scale invariant phase transition of disordered bosons in one dimension

the two-loop level [115]). In the strong-disorder limit, real-space RG treatments [116, 117] and the “scratched-XY” criticality [118] also predict a BKT-type transition but at a non-universal value of $K_c > 3/2$. These considerations exhaust known scenarios for the disorder-induced superfluid to non-superfluid phase transitions in 1D.

In this work, we consider the disorder-induced localization transition in 1D superfluids of bosons with power-law hopping decaying with distance as $1/r^\alpha$. We utilize numerically exact large scale Quantum Monte-Carlo simulations based on the Worm Algorithm [10] to determine the ground-state superfluid phases and phase transitions for different values of $\alpha > 2$. We find that the superfluid phases can be approximately characterized by an effective LL parameter K that reproduces the decay of correlation functions. However, contrary to existing theories, we find that the disorder-induced quantum phase transition is generically scale-invariant and incompatible with the BKT scenario with the effective $K_c \leq 3/2$ for all $\alpha \leq 3$. As far as critical exponents are concerned, the data is consistent with the correlation length exponent satisfying the Harris bound $\nu \geq 2$ for all values of $\alpha \leq 3$. Thus, our results reveal a new universal behavior of bosons with power-law hopping in one dimension with finite integral over space. For $\alpha > 3$ our results are instead consistent with a scenario where the superfluid is pinned by an infinitesimal disorder in the thermodynamic limit, similar to a BKT-like scenario for hard-core particles with short-range coupling. Our predictions are directly relevant for experiments with dipolar atoms and molecules, exciton materials, and cold ions.

We consider the following 1D lattice Hamiltonian for hard-core bosons

$$\mathcal{H} = -t \sum_{i < j} \frac{a^\alpha}{|r_{ij}|^\alpha} \left[b_i^\dagger b_j + \text{H.c.} \right] + \sum_i \varepsilon_i n_i, \quad (n_i \leq 1). \quad (3.1)$$

We employ standard notations for bosonic creation and annihilation operators on site i and restrict the maximal occupation number, $n_i = b_i^\dagger b_i$, to unity. The nearest-neighbor hopping amplitude, t , and the lattice spacing, a , are taken as units of energy and length, respectively. We choose random on-site energies ε_i uniformly distributed between $-W$ and W , and check that a different (gaussian) choice of distribution does not affect the results. In spin language, Eq. (4.1) is equivalent to an XY Hamiltonian with power-law exchange couplings, which, in the absence of disorder, can be realized in experiments with cold polar molecules [1], trapped ions [2–4] and Rydberg atoms [5, 119–123] (the latter can also be disordered [124]).

For ideal system with $W/t = 0$, the spectra and low-energy phases of Hamiltonian (4.1) have been investigated by a variety of approaches. Using linear spin-wave theory, Ref. [125] identified $\alpha > 3$ as a regime where main properties reproduce those observed in the $\alpha = \infty$ limit of finite-range interactions; $1 < \alpha < 3$ as an intermediate regime with the XY phase

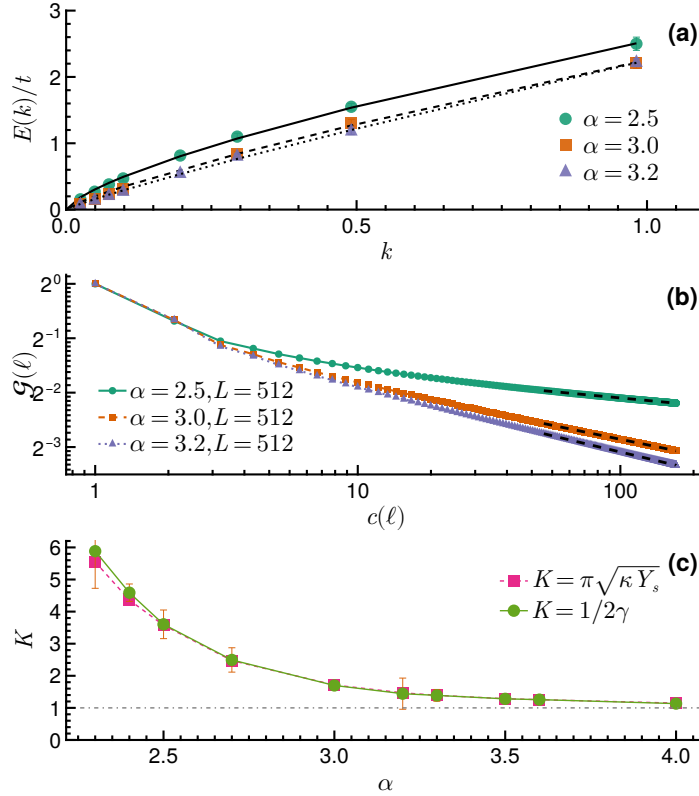


Fig. 3.1 Characterization of the superfluid phase for $W/t = 0$: (a) Dispersion relations $E(k)$ vs k for $\alpha = 2.5, 3.0$ and 3.2 chosen in the intermediate and short-range regimes, respectively (see text) for $L = 256$. (b) Single particle density matrix $\mathcal{G}(\ell)$ vs chord distance $c(\ell) = \sin(\pi\ell/L)/\sin(\pi/L)$ showing an algebraic decay for all α for $L = 512$. Dashed lines indicate the best fit with $A \cdot c(\ell)^{-\gamma}$ where A, γ are fitting parameters. (c) Numerical evaluation of the Luttinger liquid parameter K as a function of α from the power-law decay $\mathcal{G} \propto \ell^{-1/(2K)}$ (green dots) and from the relation $K = \pi\sqrt{\kappa_s Y_s}$ (red squares) extrapolated to the thermodynamic limit via a polynomial scaling in $1/L$.

characterized by a continuously varying dynamical exponent $z = (\alpha - 1)/2$ (it governs the $k \rightarrow 0$ limit of the dispersion relation); and $\alpha < 1$ as a long-range regime with dispersionless excitations and properties similar to the infinite-range $\alpha = 0$ case in the thermodynamic limit. In this harmonic approach, $\alpha = 3$ is the boundary between the intermediate and short-range regimes. Using a bosonization approach supplemented by an RG analysis, Ref. [13] predicts that power-law couplings are relevant in the RG sense for $\alpha < 3 - 1/(2K)$, with $K > 1$ to be determined numerically for each given α . In the following, we study the ground-state superfluid phases and phase transitions of Eq. (4.1) for $\alpha > 2$ using large scale path-integral quantum Monte-Carlo simulations based on the Worm algorithm [10]. Without loss of generality, we focus on the particle density $\rho = 1/2$.

Scale invariant phase transition of disordered bosons in one dimension

We start our analysis by first characterizing the bosonic liquid in the absence of disorder ($W/t = 0$). Figure 3.1(a) shows the dispersion relation $E(k)$ vs k for three values of $\alpha = 2.5, 3.0,$ and 3.2 where k is the quasi-momentum. It was deduced numerically from spectral peaks after analytic continuation of the imaginary-frequency dynamic structure factor [114, 113]. The chosen values of α correspond to values in the expected intermediate ($\alpha = 2.5$), boundary ($\alpha = 3.0$) and short-range ($\alpha = 3.2$) limits of the spin-wave analysis, respectively. The dispersion relation is non-linear in k for $\alpha = 2.5$ (dots) and the data can be fit well by $E(k) \sim k^{z_*}$, with $z_* \simeq 0.74$, in good agreement with the $z = 0.75$ prediction of spin-wave analysis (continuous black line). In the short-range regime, instead, the dispersion relation is consistent with the linear law and a small negative quadratic contribution, also in agreement with literature. We checked that $E(k)$ for different system sizes agree with each other for the same values of k . [The dispersion relation in the superfluid phase for $\alpha = 2.5$ in the presence of disorder is sub-linear, as presented in Appendix A¹.]

For a 1D superfluid ground state, the single-particle density matrix $\mathcal{G}(\ell) = \langle b_i^\dagger b_{i+\ell} \rangle$ is expected to show an algebraic decay with the distance ℓ with diverging integral over space. Our data for \mathcal{G} are shown in Fig. 3.1(b), for the same values of α as in panel (a) for a system with $L = 512$ sites and inverse temperature $\beta = L/t$. We observe algebraic decay $\mathcal{G} \sim \ell^{-\gamma}$ for all α .

Despite the non-linear dispersion relation demonstrated above, we attempt a comparison with expectations from LL theory by extracting an effective LL parameter K as a function of α from two standard methods: the power-law decay $\mathcal{G} \sim \ell^{-\gamma}$ via the bosonization relation $\gamma = 1/(2K)$ (green dots) and the relation $K = \pi\sqrt{\kappa Y_s}$ (red squares). Both κ and Y_s can be conveniently computed by quantum Monte Carlo through mean-square particle, N , and winding number, \mathcal{W} , fluctuations using the Pollock–Ceperley relation $Y_s = L\langle \mathcal{W}^2 \rangle / \beta$. Figure 3.1(c) shows that the two methods produce similar estimates of K for all α , within the error bars, which is surprising, given the non-linear dispersion relation demonstrated above. Moreover, K decreases monotonically and continuously with α from a large value $K \gtrsim 5$ at $\alpha \sim 2.3$ to $K \approx 1$ at $\alpha = 4$. Within an approximate LL scenario, this behavior may be explained by the fact that power-law hopping in Hamiltonian (4.1) allows for large-scale particle exchanges for small enough $\alpha < 3$, mimicking the behavior of soft-core bosons, for which one can easily get $K \gg 1$. The $K = 1$ value (dashed dotted line) corresponds to the short-range case of hard-core bosons with the nearest neighbor hopping, a limit that is here asymptotically approached at $\alpha > 3$ [7]. In the following we analyse the situation at finite disorder strength and, in particular, explore the nature of the transition point, which is expected to be of the BKT type for Luttinger liquids.

¹See Appendix A for the supplemental material including the dispersion relation in the superfluid phase with finite disorder. The supplemental material includes Refs. [126, 114, 113].

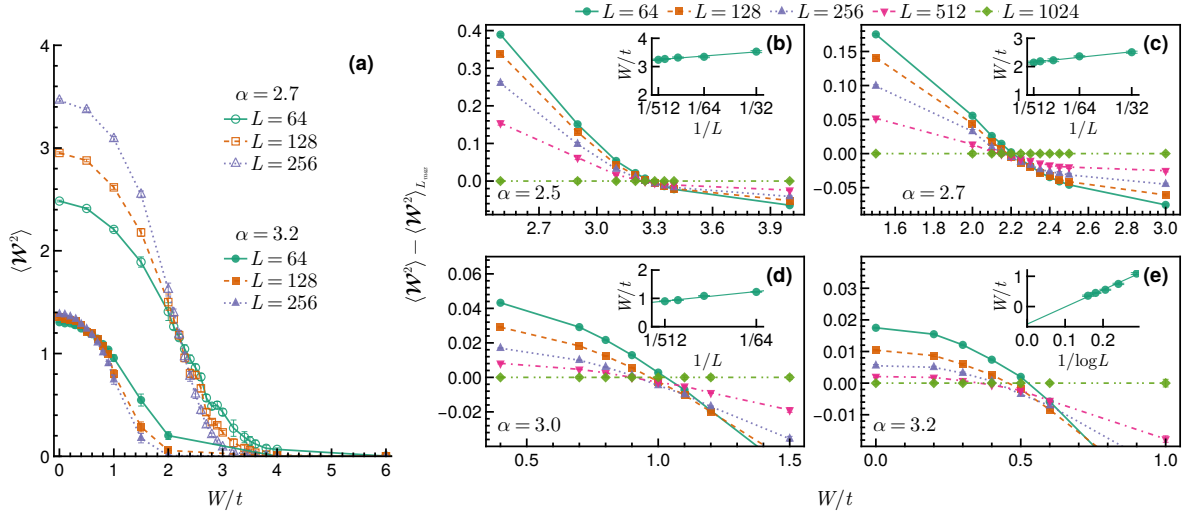


Fig. 3.2 Characterization of the superfluid to non-superfluid phase transition: (a) Mean-square winding number $\langle \mathcal{W}^2 \rangle$ vs disorder strength W/t for $\alpha = 2.7$ (empty symbols) and 3.2 (full symbols) for system sizes $L = 64, 128, 256$. (b)-(e) Zoom-in on the area near phase transitions for $\alpha = 2.5, 2.7, 3.0$ and 3.2 , showing crossing between the curves; the curve corresponding to the largest size $L = 1024$ is subtracted from all data for clarity. Vertical error bars indicate the estimated uncertainty from the Monte Carlo simulations and disorder-averages. Insets: Finite-size scaling of crossings points between curves for system sizes L_1 and $L_2 = 2L_1$ as a function of $L = L_1$.

However, we note that this may not be the case here: BKT transition and its asymptotically exact RG flow are rooted in logarithmic interactions between vortex excitations. The latter originates from the kinetic energy of the flow around vortices $E \sim \int (n_s/m) dr/r$, where m is the particle mass and n_s the superfluid density. The single particle spectrum in our model is not parabolic and formally corresponds to a scale dependent “mass” $m(r) \sim r^{3-\alpha}$, implying that vortices in the superfluid phase should be bound by a power-law, not logarithmic, potential. It may thus be expected that BKT physics no longer applies for $\alpha \lesssim 3$.

We characterize the transition via the winding number fluctuations $\langle \mathcal{W}^2 \rangle$ since they are a scale invariant quantity, differently from the superfluid stiffness Y_s . Figure 3.2(a) shows the evolution of superfluid properties measured by $\langle \mathcal{W}^2 \rangle$ with disorder, W/t , for two example cases $\alpha = 2.7$ (empty symbols) and 3.2 (full symbols) and for several values of $L = 64, 128, 256$. In both cases, $\langle \mathcal{W}^2 \rangle$ decrease monotonically with increasing W/t , until they reach near zero values. This behavior signals the transition between the superfluid and non-superfluid states. In the short-range case $\alpha = 3.2$, the behavior at larger values of disorder is reminiscent of what is expected for a BKT transition when in the infinite system $\langle \mathcal{W}^2 \rangle$ displays a jump to zero at the critical point [7]. However, surprisingly, for $\alpha = 2.7$ there is a clear crossing point of

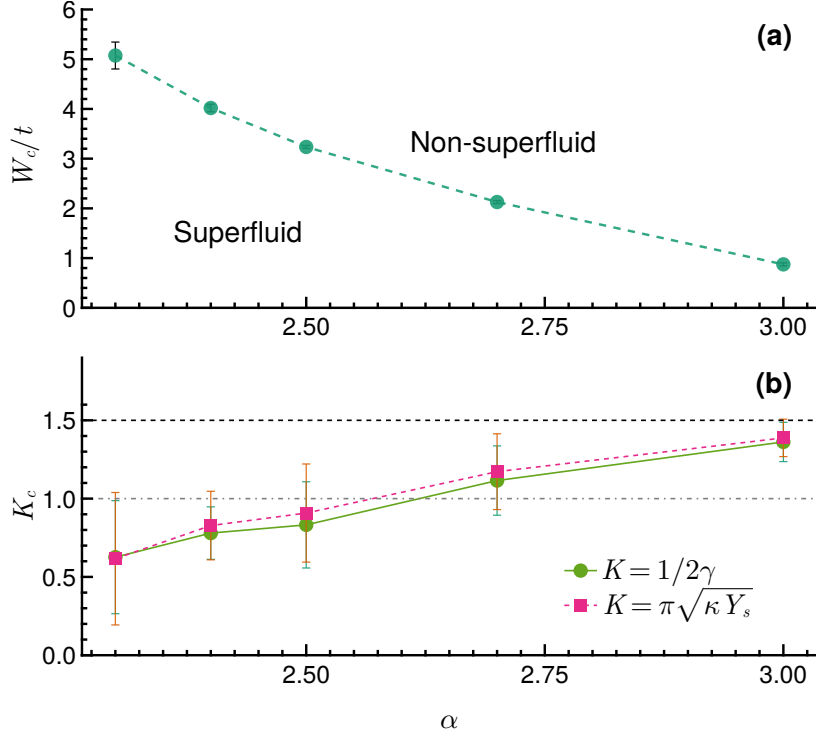


Fig. 3.3 (a) Phase diagram, W_c vs α , of the superfluid and non-superfluid quantum phases for model (4.1). (b) Critical values of LL parameter K_c at W_c vs α , as estimated from the power-law decay of \mathcal{G} (green dots) and from $K = \pi\sqrt{\kappa Y_s}$ (red squares) for $L = 256$.

$\langle \mathcal{W}^2 \rangle$ around $W/t \sim 2$. This is inconsistent with the BKT criticality and is, instead, a signature of continuous scale-invariant phase transitions. This fact can be used to pinpoint the critical disorder strength W_c where superfluidity is lost by the crossing point of $\langle \mathcal{W}^2 \rangle$ -vs- W curves for different values of L . The panels (b)-(e) in Fig. 3.2 present data in the vicinity of transition points for $\alpha = 2.5, 2.7, 3.0$ and 3.2 using $\beta = L/(8t)$ [even for $\alpha = 3.2$ our temperature is a factor of two smaller than the lowest phonon mode]. Crossing points are very pronounced in (b) and (c) for intermediate exponents α , leaving no doubt that we are dealing with generic continuous transitions at $W/t = 3.24(5)$ for $\alpha = 2.5$ and at $W/t = 2.12(5)$ for $\alpha = 2.7$. The crossings appear to persist when transitioning to the short-range regime $\alpha \gtrsim 3$, see panels (d) and (e) in Fig. 3.2 with crossings around $W/t = 0.87(5)$ for $\alpha = 3.0$ and around $W/t = 0.5(5)$ for $\alpha = 3.2$, contrary to all expectations. However a careful finite-size scaling up to large system sizes $L = 1024$ shows that the transition point for $\alpha > 3$ scales to $W/t \rightarrow 0$ in the thermodynamic limit, see Inset in Fig. 3.2(e), implying the absence of a continuous phase transition at finite W in the thermodynamic limit. This is different from $\alpha \leq 3$, where the transition point scales to a finite value of W/t , see Insets in Fig. 3.2(b-d). The breakdown of

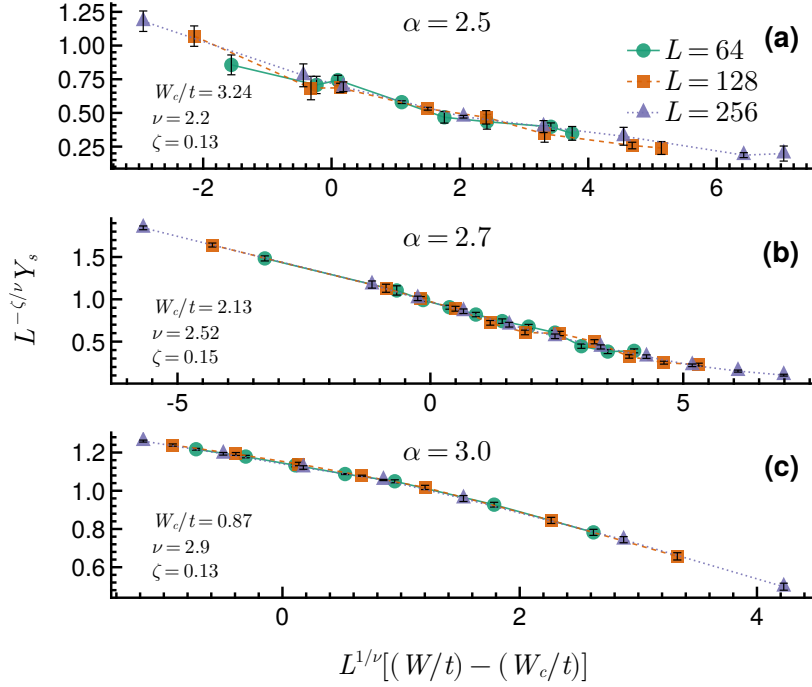


Fig. 3.4 (a)-(c) Data collapse for the scaled superfluid stiffness $L^{-\zeta/\nu} Y_s$ vs $L^{1/\nu}[(W/t) - (W_c/t)]$ for $\alpha = 2.5, 2.7$ and 3.0 using $L = 64, 128, 256$. The fitted values of the correlation length exponent ν and ζ are reported directly in the figure. They satisfy $\nu \gtrsim 2$ for all α .

the BKT scenario for all values $2 < \alpha \leq 3$ in Eq. (4.1) is surprising and is the main result of this work.

Figure 3.3(a) summarizes the ground state phase diagram of Hamiltonian (4.1) in terms of W_c and α . Here, for each $\alpha \leq 3$, the critical point W_c is determined from the scale-invariant crossing point as described above. The critical disorder strength W_c/t decreases monotonically from a large value $W_c/t \sim 5.1$ to ~ 0.9 for $\alpha = 3$. For $\alpha > 3$ the transition in the thermodynamic limit occurs at $W_c/t = 0^+$. The limiting value $W_c/t = 0^+$ would correspond to the strictly short-range limit of hard-core bosons with short-range hopping, which are known to be localized by an infinitesimal disorder [7].

Figure 3.3(b) shows the critical LL parameter K_c computed at W_c/t for each value of α assuming that the approximate LL scenario properly describes the system. We find that, for $\alpha \lesssim 3$, K_c remains smaller than the critical BKT value of $3/2$ for short-range hopping models with weak disorder [7], confirming that LL theory should not be used to describe the localization transition in the whole range $\alpha \leq 3$. In contrast, for $\alpha > 3$ our results are in agreement with conclusion that ideal systems with $K < 3/2$ are ultimately pinned by disorder, leading to an insulating BG phase for any finite value of W/t .

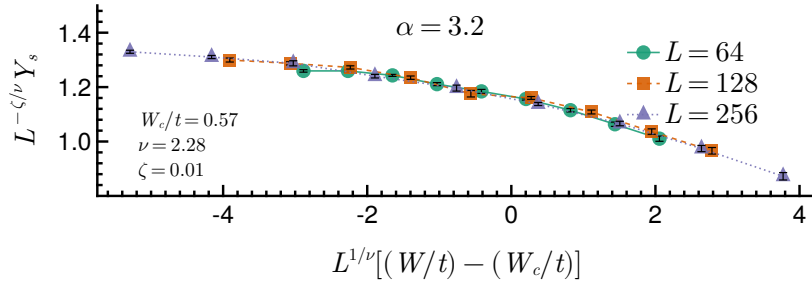


Fig. 3.5 Data collapse for the scaled superfluid stiffness $L^{-\zeta/\nu} Y_s$ vs $L^{1/\nu}[(W/t) - (W_c/t)]$ for $\alpha = 3.2$ using $L = 64, 128, 256$. The fitted values of the correlation length exponent ν and ζ are reported directly in the figure. Unlike for $\alpha < 3$, this scaling corresponds here to a finite-size effect, as the transition is not located at $W_c/t = 0.57$ and slowly shifts to $W_c/t = 0$, see Fig. 3.2(e).

We complete our characterization of quantum phase transition in Fig. 3.3(a) by determining the correlation length exponent ν using data collapse analysis near the critical points [127]. For each α , the results of Monte Carlo simulations are rescaled by $L^{-\zeta/\nu} Y_s$ and collapsed on a single master curve using $L^{1/\nu}[(W/t) - (W_c/t)]$ as a variable. Critical values W_c/t are taken from the crossing points in Fig. 3.2, while ν and ζ are treated as fitting parameters and obtained using a Nelder-Mead algorithm [128] with a cost function based on the Kawashima-Ito-Houdayer-Hartmann quality metric [129, 130]. Example results for $\alpha = 2.5, 2.7, 3.0$ and $\alpha = 3.2$ are shown in Figs. 3.4 and 3.5, respectively. We observe good collapse of all data near the critical points for $\alpha \geq 2$, and the obtained correlation length exponents always satisfy the so-called Harris bound $\nu \gtrsim 2$, see [131]. In fact, this result is expected from general arguments for a large class of d -dimensional disordered systems where an appropriately defined correlation length diverges [132]. Data collapse for $\alpha > 3$ using $W_c/t = 0.57$ is a finite-size effect given that this value of α is close to the boundary between the intermediate and short-range regimes and crossing points slowly shift to zero with increasing the system size. However, this effect will likely be observed in experiments dealing with finite systems.

In conclusion, we have demonstrated that the disorder-induced superfluid to non-superfluid quantum phase transition for models with power-law hopping is a scale-invariant transition if $2 < \alpha \leq 3$, ruling out the expected BKT scenario for interacting one-dimensional bosons in this regime. Our work opens up multiple other research directions, including whether the finite-temperature BKT scenario is generally inconsistent with power-law hopping models also in two dimensions [133, 134, 9]. Another open question is the nature of the non-superfluid quantum phase for general values of α . In Ref. [135] it was conjectured that for $\alpha = 3$ this phase is a non-superfluid Bose metal phase with finite zero-frequency optical conductivity and

algebraic decay of correlations. It is an open question whether similar behavior can be found for other α values. Our predictions should be directly testable in experiments for XY models realized via internal excitations of cold dipolar atoms and molecules, cold ions chains, and Rydberg atoms.

Chapter 4

Bose-Hubbard model with power-law hopping in one dimension

We investigate the zero-temperature phase diagram of the one-dimensional Bose-Hubbard model with power-law hopping decaying with distance as $1/r^\alpha$ using exact large scale Quantum Monte-Carlo simulations. For all $1 < \alpha \leq 3$ the quantum phase transition from a superfluid and a Mott insulator at unit filling is found to be continuous and scale invariant, in a way incompatible with the Berezinskii-Kosterlitz-Thouless (BKT) scenario, which is recovered for $\alpha > 3$. We characterise the new universality class by providing the critical exponents by means of data collapse analysis near the critical point for each α and from careful analysis of the spectrum. Large-scale simulations of the grand canonical phase diagram and of the decay of correlation functions demonstrate an overall behavior akin to higher dimensional systems with long-range order in the ground state for $\alpha \leq 2$ and intermediate between one and higher dimensions for $2 < \alpha \leq 3$. Our exact numerical results provide a benchmark to compare theories of long-range quantum models and are relevant for experiments with cold neutral atom, molecules and ion chains.

The Bose-Hubbard (BH) model describes the dynamics of interacting bosons confined in a lattice potential with nearest-neighbor hopping energy t and local interactions U . It features a localization quantum phase transition from a gapless superfluid to a gapped Mott insulator as a function of the ratio t/U [24, 136–138]. The BH model has been successfully used to describe quantum phase transitions in systems as diverse as cold atoms trapped in optical lattices, superfluid ^4He , and superconductors. In one dimension, the BH quantum phase transition at constant integer density ρ belongs to the Berezinskii-Kosterlitz-Thouless (BKT) [35, 36, 139, 66, 140, 68] universality class. The latter has been experimentally demonstrated

Bose-Hubbard model with power-law hopping in one dimension

in cold atom experiments in Refs. [141, 142] and is widely believed to underpin all localization transitions in one dimension.

In the last few years, advances in engineering Hamiltonians with Rydberg atoms, cold dipolar atoms and molecules, trapped ions coupled to motional degrees of freedom and neutral atoms coupled to photonic modes [143–147] have sparked significant interest in the many-body physics of quantum models with long-range couplings. Theory and experiments have provided evidence for novel static and dynamic phenomena in these systems [9], such as, e.g., the non-local propagation of correlations [76–78, 2, 3], breaking of conformal symmetry [79, 80], new topological phases of matter and phase transitions [79, 81, 82]. The most interesting regime is that of so-called "weak long-range interactions" with $d < \alpha < \alpha_*$, which is intermediate between the limit of infinite-range "strong interactions" for $\alpha < d$ and short-range-like interactions for $\alpha > \alpha_*$, with d the dimension and α_* a threshold value that depends on the system and transition under study [9]. While integrable models provide a guidance in some situations [79] and despite an intense theoretical effort, it remains an open challenge to precisely characterize quantum phases and phase transitions in non-integrable quantum models with long-range couplings. It is thus of fundamental importance to obtain exact results for these systems, to which theories can be compared.

In this work, we investigate the phase diagram of the $1d$ BH model with power-law hopping that decays with distance as $1/r^\alpha$ in the regime of weak long-range couplings $\alpha > 1$. We use exact large-scale Quantum Monte Carlo simulations based on the Worm Algorithm [10] to determine the ground state phase diagram and to characterize the superfluid phases. Qualitatively, the phase diagram in the grand-canonical ensemble shows a shrinking of the MI lobes in the t/U - μ/U plane (μ is the chemical potential) with respect to short-range models for all $\alpha < 3$ [148] and a rounding of the lobes akin to higher-dimensional models for $\alpha < 2$. Interestingly, for constant $\rho = 1$ a finite-size scaling analysis of the winding number fluctuations, measuring superfluid properties, shows that the superfluid-Mott insulator quantum phase transition is incompatible with the BKT universality class for any $1 < \alpha \leq 3$. It corresponds instead to a new continuous scale-invariant phase transition in the whole parameter range of weak long-range couplings. We characterize this new universality class for bosons in one dimension by determining the critical exponents by data collapse at the critical point and the energy spectrum. For $\alpha > 3$ the system resembles short-range models, which fixes α_* to $\alpha_* = 3$. From a large-scale analysis of correlation functions, we confirm that long-range order exists for $\alpha < 2$ in the superfluid phase, in agreement with literature, while we find no evidence of such order for $\alpha > 2$. These exact results provide benchmarks for theories and experiments.

The 1d BH model with power-law hopping reads

$$\mathcal{H} = -t \sum_{i < j} \frac{a^\alpha}{|r_{ij}|^\alpha} \left[b_i^\dagger b_j + \text{H.c.} \right] + \frac{U}{2} \sum_i n_i (n_i - 1) - \mu \sum_i n_i \quad (4.1)$$

Here, b_i^\dagger , b_i , and $n_i = b_i^\dagger b_i$ are the bosonic creation, annihilation and particle number operators on site i , respectively; t , U and μ are the hopping energy, the on-site interaction energy and the chemical potential, respectively, with a the lattice spacing. The energy and length scales are set by choosing $t = 1$ and $a = 1$. For nearest neighbor hopping ($\alpha \rightarrow \infty$) and density $\rho = 1$, Eq. (4.1) displays a zero-temperature quantum phase transition of the BKT type from a superfluid to a Mott insulator at a critical value $(t/U)_c = 0.300 \pm 0.025$ [149–151, 44]. For finite α and $U/t \rightarrow \infty$ (hard-core bosons), Eq. (4.1) maps into a long-range XY model, for which spin-wave and semi-analytical renormalization group analyses predict a continuously varying dynamical exponent $z = (\alpha - 1)/2$ for $\alpha < 3$ as well as a breaking of $U(1)$ symmetry, and ensuing long-range order, for a given $\alpha_c < 3$, to be determined numerically. In Ref. [13], α_c was estimated to be $\alpha_c \simeq 2.8$ using a density matrix renormalization group approach for system sizes up to $L \simeq 100$. In this work, we investigate Eq. (4.1) for $1 < \alpha \leq 3$ and all values t/U via large scale quantum Monte Carlo simulations of up to $L = 1024$ sites and inverse temperature $\beta = L^{z_*}$, small enough to probe ground state properties. We focus first on the superfluid-Mott insulator quantum phase transition at varying and constant densities and then discuss the correlation functions in the liquid phase.

Figure 4.1 shows the ground state phase diagram as a function of μ/U and t/U for different $\alpha \leq 3$. For each α , the figure shows the existence of a lobe, corresponding to a MI phase at unit filling surrounded by a SF phase. For each ratio t/U , the boundaries in μ of the lobe are determined by computing the energy gap in the MI phase from the Green function $G(k=0, \tau)$, which is obtained via the spatial averaging of the Matsubara Green function, $G(i, \tau) = \langle b_i^\dagger(\tau) b_0(0) \rangle$, with $\tau \in [-\beta/2, \beta/2]$ the imaginary time and k the quasi momentum. By employing the Lehmann expansion, the Green function behaves as $G(k, \tau) \propto e^{-\varepsilon_\pm(k)|\tau|}$ for $\tau \rightarrow \pm\infty$, where ε_\pm denote the particle and hole energies, respectively [152, 153] (see also example in Inset of Fig. 4.2 and below): For $\tau > 0$, $G(k, \tau)$ describes a particle excitation, whereas for $\tau < 0$, it represents a hole excitation in the MI phase. By fitting the asymptotic behavior of $G(k=0, \tau)$ to an exponential form, the particle and hole excitation energies are extracted from the slopes. These excitation energies are measured relative to the chemical potential in the grand canonical ensemble. The insulating gap, Δ , is then determined as $\Delta = \mu_+ - \mu_-$, where $\mu_\pm = \mu \pm \varepsilon_\pm$ and μ is the chemical potential used in the simulation.

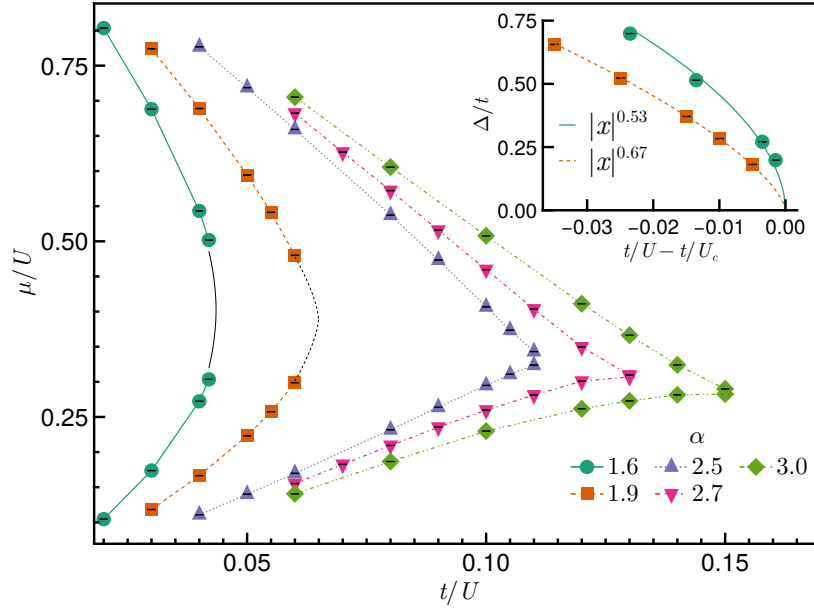


Fig. 4.1 Ground state phase diagram of the 1D Bose-Hubbard model with power-law hopping for $\alpha = 1.6, 1.9, 2.5, 2.7,$ and 3.0 , showing the boundary between the Mott insulator (at unity filling) and superfluid phases as a function of chemical potential μ/U and hopping amplitude t/U . Markers represent simulation data, while the solid black line (for $\alpha = 1.6$) and the dashed black line (for $\alpha = 1.9$) are obtained from fitting the energy gap Δ/t near the critical point as $\Delta/t \sim |t/U - t/U_c|^{-z^* \nu}$ (see also Fig. 4.2 and text). Inset: Gap Energy Δ/t fitted as a function of $t/U - t/U_c$

Figure 4.1 shows two distinct behaviours of the lobe structure for $\alpha < 2$ and $\alpha > 2$. Surprisingly, for $\alpha < 2$ the Mott lobes are smooth and rounded, similar to those observed for corresponding MI phases in higher dimensions [154, 153]. For $\alpha > 2$, instead, the MI phase exhibits a progressively more pointed and asymmetric structure with increasing α and the critical point at constant density (i.e. the tip of the lobe) shifts to larger values of t/U . This behavior is reminiscent of the pointy lobe structure of the short-range hopping model associated to a BKT transition at $\rho = 1$, indicating a behavior intermediate between higher dimensions and one dimension. We come back below to the precise nature of the critical point.

We further investigate the properties of the superfluid phase near the transition point at constant density by computing the excitation spectrum. Figure 4.2 shows the dispersion relation $E(k)$ vs k for different $1 < \alpha < 3$, where quantum Monte-Carlo data for $E(k)$ (symbols) are obtained by fitting the large- τ decay of the Green's function $G(k, \tau)$ to an exponential form (see Inset for examples). The resulting dispersion relations are sub-linear in k , in excellent agreement

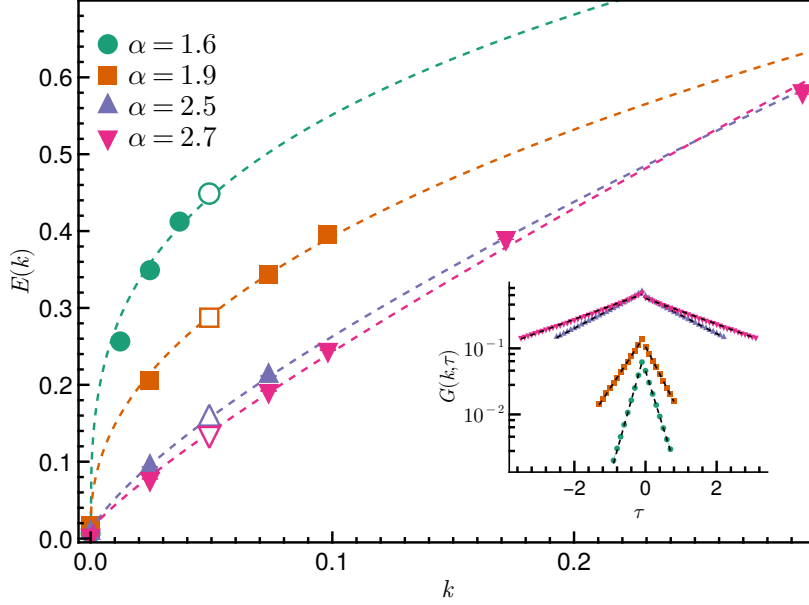


Fig. 4.2 Dispersion relation $E(k)$ vs. k for $\alpha = 1.6, 1.9, 2.5,$ and 2.7 in the superfluid phase near the transition along the commensurate density line. Symbols denote numerical data obtained from fitting the long-time exponential decay of $G(k, \tau)$, while lines show the spin-wave analysis prediction $E(k) \sim k^{z_*}$, with $z_* = (\alpha - 1)/2$ [125]. Inset: Single-particle Green function $G(k, \tau)$ for $k = \pi/64$ (represented by empty markers) and $\alpha = 1.6, 1.9, 2.5,$ and 2.7 . The black dashed line represents the numerical fit to the exponential decay.

with the predicted scaling $E(k) \sim k^{z_*}$ from spin-wave theory for all α , with $z_* = (\alpha - 1)/2$ [125].

We characterize the SF-MI quantum phase transition at constant density $\rho = 1$ by computing the mean-squared winding number fluctuations $\langle \mathcal{W}^2 \rangle$ – a scale-invariant quantity proportional to the superfluid stiffness Y_s as $\langle \mathcal{W}^2 \rangle = Y_s/(LT)$ – up to sizes $L = 1024$. $\langle \mathcal{W}^2 \rangle$ is expected to have a finite value and a zero value in the SF and MI phases, respectively. Figures 4.3(a) and (b) present example results for $\langle \mathcal{W}^2 \rangle$ as a function of t/U for two power-law exponents $\alpha < 2$ and $\alpha > 2$ in Eq. (4.1), respectively, and for different system sizes L . In the figures, the values of $\langle \mathcal{W}^2 \rangle_{L_{\max}}$ for the largest sizes L_{\max} used in the computations have been subtracted for clarity. Panels (a) and (b) show a clear crossing of $\langle \mathcal{W}^2 \rangle$ vs t/U when plotted for different L at values $(t/U)_c = 0.043 \pm 0.005$ and $(t/U)_c = 0.131 \pm 0.008$, respectively. These crossings correspond to a quantum phase transition at the respective values of the critical ratio $(t/U)_c$ (see Insets for further extrapolation to thermodynamic limit). Interestingly, the very presence of a crossing in the $\langle \mathcal{W}^2 \rangle - (t/U)$ curves rules out the Berezinskii-Kosterlitz-Thouless universality class for these power law models, in contrast to familiar short-range models in one dimension [7]

Bose-Hubbard model with power-law hopping in one dimension

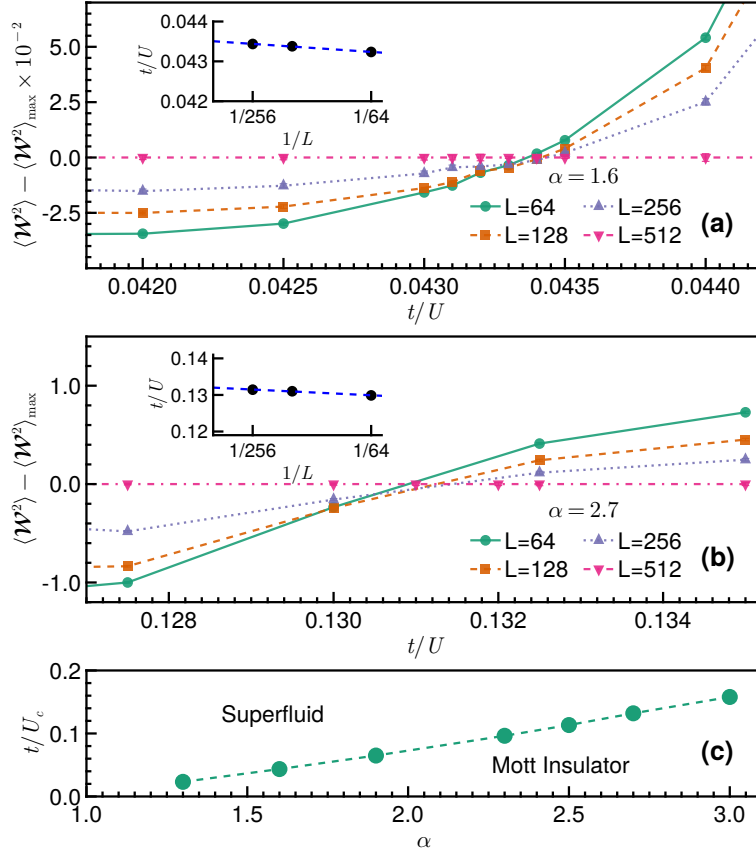


Fig. 4.3 Characterization of the Mott insulator to superfluid phase transition: (a)-(b) Mean-square winding number $\langle \mathcal{W}^2 \rangle$ vs t/U for $\alpha = 1.6$ and 2.7 near phase transitions, showing crossing between the curves; the curve corresponding to the largest lattice size is subtracted from all data for clarity. Vertical error bars indicate the estimated uncertainty from the Monte Carlo simulations. Insets: Finite-size scaling of crossings points between curves for system sizes L_1 and $L_2 = 2L_1$ as a function of $L = L_1$. (c) Phase diagram, t/U_c vs α of the Mott insulator and superfluid quantum phases for model (4.1).

and long-range models with power-law density-density interactions [155, 156, 7]. Similar crossings are observed for all $1 < \alpha \leq 3$, implying a continuous scale-invariant phase transition in this whole range of α . For $\alpha > 3$ the transition is instead of the BKT type, consistent with short-range models. This fixes $\alpha_* = 3$ for the model (4.1).

Figure 4.3(c) summarizes the ground state phase diagram of Eq. (4.1) as a function of $(t/U)_c$ and $1 < \alpha \leq 3$. In this diagram, $(t/U)_c$ for each value of α is identified based on the scale-invariant crossing point, as previously detailed. The discovery of this family of scale-invariant phase transitions is a key result of this work.

We further characterize the SF-MI quantum phase transitions at commensurate density by determining the correlation length exponent ν associated to the continuous transition using data

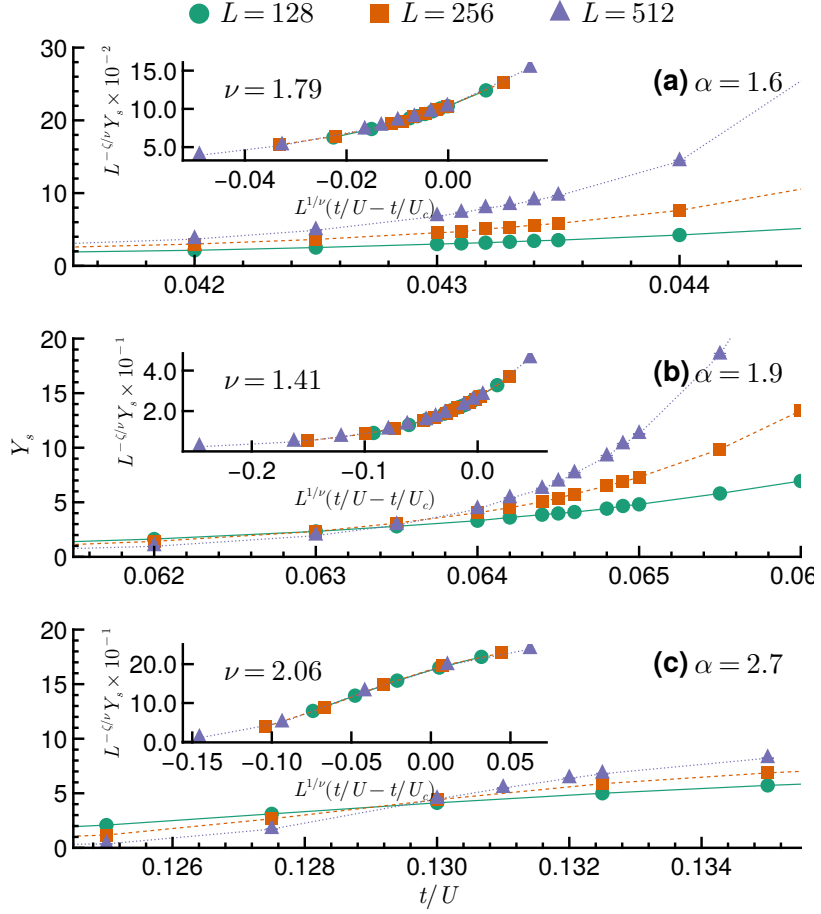


Fig. 4.4 Superfluid stiffness Y_s near the critical interaction strength t/U_c for $\alpha = 1.6, 1.9$ and 2.7 and lattice size $L = 128, 256, 512$. Inset: Data collapse for the scaled superfluid stiffness $L^{-\zeta/\nu} Y_s$ vs $L^{1/\nu} [(t/U) - (t/U)_c]$. The fitted values of the correlation length exponent ν are directly reported in the inset. For $\alpha = 1.6$ and 1.9 , ν is consistent with the value derived by fitting energy gap Δ . (see Figure 4.1)

collapse analysis near the critical points. For each α , we rescale the superfluid stiffness using $L^{-\zeta/\nu} Y_s$ as a function of $L^{1/\nu} [(t/U) - (t/U)_c]$, where ν and ζ are fitting parameters (see Insets). These parameters are determined through optimization using the Nelder-Mead algorithm [128], with a cost function based on the Kawashima-Ito-Houdayer-Hartmann quality metric [129, 130]. Example results for $\alpha = 1.6, 1.9$, and 2.7 are shown in Figure 4.4, demonstrating good data collapse near the critical points for all $\alpha \geq 1$.

For consistency, we further estimate the correlation length exponent ν by using the expected expression for the gap energy $\Delta/t \sim |t/U - t/U_c|^{-z_*\nu}$ near the critical point (see Fig. 4.1), with z_* obtained numerically from the energy dispersion relation, as discussed above. As an example, for $\alpha = 1.6$ and 1.9 we obtain $\nu = 1.77 \pm 0.03$ and $\nu = 1.49 \pm 0.04$, respectively, in

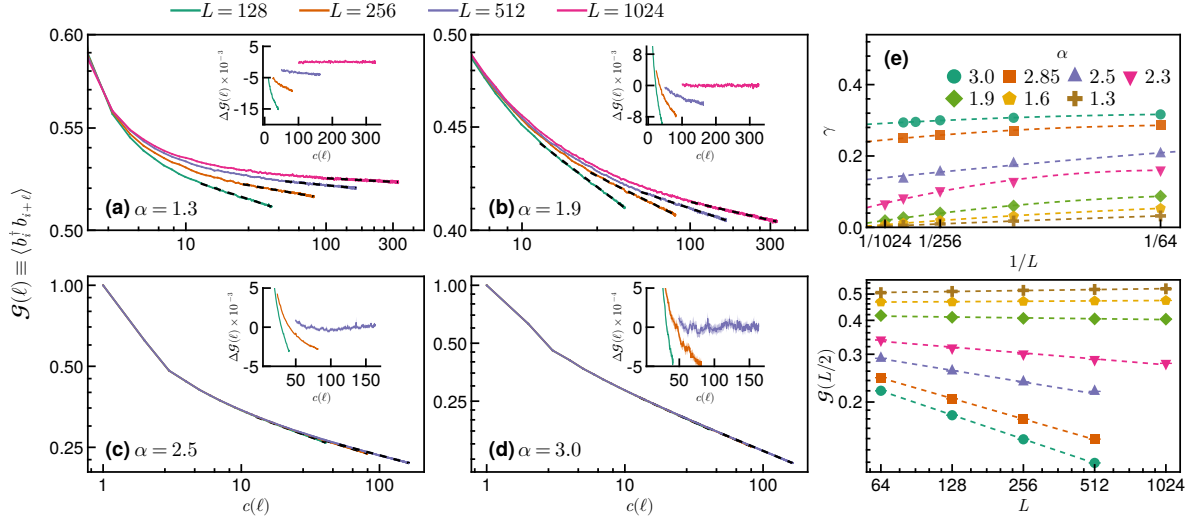


Fig. 4.5 Characterization of the superfluid phase: (a)-(d) Single-particle density matrix, $\mathcal{G}(\ell)$, plotted against ℓ for $\alpha = 1.3, 1.6, 2.5$, and 2.7 . The dashed line represents the best fit to $A \cdot c(\ell)^{-\gamma}$, where $c(\ell) = \sin(\pi\ell/L)$ is the chord distance, and A and γ are fitting parameters. For $\alpha = 1.3$ and 1.9 , $\mathcal{G}(\ell)$ saturates to a constant as $\ell \rightarrow \infty$. For $\alpha = 2.5$ and 2.7 , $\mathcal{G}(\ell)$ exhibits algebraic decay. Insets: Difference $\Delta \mathcal{G}(\ell)$ between $\mathcal{G}(\ell)$ for system size L and the numerical fit for $L = L_{\max}$, plotted as a function of the chord distance $c(\ell)$. The difference indicates an upward trend of $\mathcal{G}(\ell)$ for increasing lattice size. (e) Finite-size scaling of the power-law exponent γ to the thermodynamic limit.

good agreement with the estimate from data collapse. Our results for different α values show that ν decreases monotonically in the range $1 < \alpha < 2$, with $\nu(\alpha = 2) \simeq 1.4$, and then grows again to $\nu \simeq 2.0$ for $\alpha = 3$ (see Supplemental Material in Appendix B).

We conclude by discussing the behavior of the single-particle density matrix $\mathcal{G}(\ell) = \langle b_i^\dagger b_{i+\ell} \rangle$ as a function of distance ℓ near the critical point. Example results are shown in Fig. 4.5(a-d) as a function of the chord distance $c(\ell) = \sin(\pi\ell/L)$ to account for periodic boundary conditions. In the figure, we present results for Eq. (4.1) for hard-core bosons ($t/U \rightarrow 0$) at half-filling, which allows us to explore the behavior of $\mathcal{G}(\ell)$ up to sizes as large as $L = 1024$ and to directly compare to existing predictions for the long-range XY model [13, 126]. Figure 4.5 shows that $\mathcal{G}(\ell)$ decays with increasing $c(\ell)$ up to the largest sizes considered, for all $1 < \alpha \leq 3$. Interestingly, for each α and given size L , this large-distance decay is very well approximated by a simple power-law as $\mathcal{G}(\ell) \sim c(\ell)^{-\gamma}$ (see Supplemental Material). However, in contrast to familiar 1D quantum liquids with short-range hopping, the value of γ is dependent on L , and in fact it *decreases* with L (see also Insets). The fitted values of γ are plotted vs $1/L$ in panel (e), showing values consistent with $\gamma = 0$ for $1 < \alpha \lesssim 2$ and $\gamma > 0$ for $2 \lesssim \alpha \leq 3$ in the thermodynamic limit. For $1 < \alpha \lesssim 2$, this is a clear sign of long-range order, a result

consistent with literature. For $2 \lesssim \alpha \leq 3$ instead, our results can be fitted essentially equally well by the simple power law and a power-law with an additional constant (see Supplemental Material). Since the former fit is marginally better and produces cleaner results, we term this region $2 \lesssim \alpha \leq 3$ as *anomalous quasi-long-range-order*, departing from expectations from literature. This analysis is further corroborated by a computation of $\mathcal{G}(\ell)$ at distance $\ell = L/2$ in Fig. 4.5(f). The latter, corresponding to the condensate fraction in the presence of a condensate, is expected to be L -independent in the presence of long-range order and to decay as a power-law with increasing L in the presence of quasi-long-range order. Figure 4.5(f) shows that $\mathcal{G}(L/2)$ is constant for $\alpha < 2$ and it decays as a power-law with increasing L for $\alpha > 2$. While it remains possible that long-range order appears at even larger scales, we find no evidence of such behavior up to the large sizes computed here. In the Supplemental Material we present corresponding data for $\mathcal{G}(\ell)$ for soft-core bosons computed up to distances $L = 512$, showing identical behavior of correlations to Fig. 4.5.

In summary, our results depart from existing approximate results based on bosonization theory and medium-scale numerical approaches [13] in identifying the region of α where long-range effects are dominant as $\alpha \leq \alpha_* = 3$. For $\alpha > 3$ we find a pure power-law decay with γ independent of L , as expected from short-range hopping models. This is consistent with recent results for disordered induced localization transition in $1d$ [8]. Interestingly, we demonstrate and characterize a new universality class of one dimensional bosons in the whole weak long-range limit $d < \alpha < \alpha_*$, a result incompatible with the usual BKT scenario. Large-scale simulations of the grand canonical phase diagram, of the constant density phase transition and of the decay of correlation functions demonstrate an overall behavior akin to higher dimensional systems with long-range order in the ground state for $\alpha < 2$ and intermediate between one and higher dimensions in the range $2 < \alpha \leq 3$.

Our predictions for the superfluid dispersion relation and the correlation functions can be directly measured in experiments with dipolar atoms and molecules ($\alpha = 3$, [145, 45, 157, 158]) and cold ions ($1 < \alpha \lesssim 3$, [147, 2, 3]). Our work provides exact results to benchmark theories for long-range quantum models and opens up multiple other research directions, including the nature of the groundstate in higher dimensions.

Chapter 5

Conclusions and Outlook

In my Ph.D. work, I investigated the emergence of exotic phenomena in strongly correlated models that hold direct experimental relevance for ultracold atomic gases and trapped-ion systems. My research specifically focused on one-dimensional many-body systems of bosonic particles with long-range, power-law decaying hopping, where quantum coherence and collective effects produce unique behaviors not found in short-range interacting systems. By leveraging state-of-the-art numerical techniques, detailed in Chapter 2, I have explored the ground-state properties of these systems, with a particular attention on how long-range hopping influences phase transitions.

In Chapter 3, we studied the influence of disorder on the phase transition between superfluid and non-superfluid states in a one-dimensional model of hard-core bosons, where the hopping amplitude falls off with distance as $1/r^\alpha$. By mapping out the phase diagram for various α values, we observe a clear trend: as α increase, the superfluid phase becomes progressively more sensitive to disorder. Specifically, the critical disorder strength required to disrupt the superfluid phase decreases with increasing α , ultimately reaching zero when $\alpha > 3$. This behavior is consistent with the short-range scenario where the superfluid is pinned by an infinitesimal disorder in the thermodynamic limit. For $2 < \alpha \leq 3$, we observed a clear crossing in the mean-square winding number $\langle \mathcal{W}^2 \rangle$ versus disorder W/t for different system sizes, revealing that the disorder-induced localization transition is continuous and scale-invariant. This finding is incompatible with the expected Berezinskii-Kosterlitz-Thouless (BKT) scenario, suggesting instead the emergence of a novel universal behavior in disordered bosons under these conditions. These results broaden our understanding of quantum phase transitions in one-dimensional bosonic systems, especially in cases where long-range hopping and disorder are involved.

Conclusions and Outlook

In Chapter 4, we examined the interaction-driven phase transition in a one-dimensional Bose-Hubbard model with power-law hopping. In this context, I have analyzed the behaviour of the superfluid-to-Mott-insulator (SF-MI) transition as both the decay exponent α and the hopping-to-interaction ratio t/U are varied. Our findings challenge previous approximate results from bosonization theory and mid-scale numerical studies by pinpointing $\alpha \leq \alpha_* = 3$ as the range where long-range interactions are dominant. We found that for $1 < \alpha \leq 3$, the interaction-driven quantum phase transition from superfluid to Mott insulator at unit filling emerges as continuous and scale-invariant, deviating from the conventional BKT framework, which applies only when $\alpha > 3$. This is consistent with our insights from disorder-induced localization in one dimension [8] (discussed in Chapter 3). When $\alpha \leq 2$, the single-particle density matrix $\mathcal{G}(\ell)$ remains finite at large distances, indicating long-range order. On the other hand, for $\alpha > 3$, the system exhibits algebraic decay in $\mathcal{G}(\ell) \propto \ell^{-\gamma}$ with power-law exponent γ independent of system size L , aligning with quasi long-range order expected in short-range models. For the intermediate regime $2 < \alpha \leq 3$, the system behaves in a way that bridges one-dimensional and higher-dimensional systems, displaying unique critical behavior and quasi-long-range order. Through large scale Quantum Monte Carlo simulations, we have established a new universality class for one-dimensional bosons within the weak long-range interaction regime ($d < \alpha < \alpha_*$). Additionally, we have mapped the phase diagram in the t/U vs. μ/U plane, showing that as α decreases, Mott insulating regions contract, transitioning from pointed to rounded lobes—a reflection of dimensional crossover effects.

This work challenges the standard BKT transition expected in one-dimensional bosonic systems when power-law hopping is present, proposing a continuous, scale-invariant transition as a new paradigm. This discovery has significant implications for future theoretical and experimental research. Several interesting avenues for further research arise from this work: one is to investigate if the finite-temperature BKT framework, typically applied to short-range systems, fails similarly in two-dimensional power-law hopping models. Another key question centers on the characteristics of the non-superfluid quantum phase for different values of α . Previous studies suggest that for $\alpha = 3$, this phase could manifest as a non-superfluid Bose metal with finite optical conductivity at zero frequency and correlations that decay algebraically [135]. Whether this behavior extends to other α values remains an open question.

The implications of our findings are experimentally accessible, particularly in platforms where XY models with power-law couplings can be realized, such as in systems with internal excitations of cold dipolar atoms and molecules and Rydberg atom arrays (for $\alpha = 3$), and chains of cold ions ($1 < \alpha \lesssim 3$). These systems provide a promising landscape for experimentally validating our predictions regarding correlation functions and superfluid dispersion relation,

and further exploring the nature of scale-invariant phase transitions in one-dimensional systems with power-law interactions. Our work provides exact benchmarks for theories on long-range quantum models and paves the way for further exploration into the characteristics of ground states in higher dimensions, potentially expanding the understanding of quantum phase transitions and scaling behaviors in low-dimensional systems with engineered long-range interactions. It establishes a benchmark for understanding the impact of dimensionality and long-range hopping on phase transitions in one-dimensional systems, highlighting how these factors shape the unique quantum behavior observed.

In addition to the work presented in this thesis, I am collaborating with Tom Hartweg on an ongoing project studying a Bose polaron system within a Bose-Hubbard bath on a 2D square lattice. A Bose polaron forms when an impurity particle moves through a bosonic lattice, attracting nearby bosons and forming a localized “cloud,” effectively creating a quasiparticle. These polarons are of great interest because they can significantly affect material properties in various systems, such as superfluid mixtures of helium isotopes (^3He and ^4He) [159], nuclear matter [160], and ultracold atomic gases [161]. Investigating impurities in quantum-critical environments like the Bose-Hubbard bath provides valuable insights into how these impurities interact with their surroundings. For instance, in certain continuous systems, the polaron’s energy can abruptly shift across specific phase transitions, such as the Berezinskii-Kosterlitz-Thouless transition [162], or Bose polarons may even disappear when the system undergoes Bose-Einstein condensation [163]. Recent work by Colussi et al. [164], using the quantum Gutzwiller method, demonstrated that when interaction between bath and impurity is weak, the impurity serves as an effective probe of bath states with polaron’s properties like bath-induced energy shifts and effective mass ratio changing notably across phase transitions. Building on this, we are using Quantum Monte Carlo simulations with a modified worm algorithm [165] to study the Bose-Hubbard bath and impurity interactions more precisely, addressing the limitations of existing Gutzwiller-based approach near the superfluid-to-Mott-insulator transition.

Appendix A

Supplemental Material: Scale-invariant phase transition of disordered bosons in one dimension

In this work, we study a one-dimensional disordered lattice boson model with hopping amplitude decaying with distance as $1/r^\alpha$ using large scale quantum Monte-Carlo simulations. A recent work [126] based on approximate functional renormalization group methods (submitted to the archive after our work was published online) proposes that in the stable superfluid phase at finite disorder strength ($W/t > 0$), a density mode with linear dispersion (dynamical exponent $z = 1$) should emerge and the superfluid–Bose-glass transition follows the BKT universality class for any α , in contradiction to our results. In this Supplemental Material we check the predictions of [126]. Our analysis based on large scale numerical simulations confirms the picture that we present in the main text.

A.1 Dispersion relation in the superfluid phase with finite disorder

The study presented in [126] proposes, using approximate functional renormalization group methods, that in the stable superfluid phase a density mode with linear dispersion (dynamical exponent $z = 1$) should emerge, and that the superfluid–Bose-glass transition follows the BKT universality class. To test these predictions, we performed large scale quantum Monte Carlo simulations for $\alpha = 2.5$ and disorder strength $W/t = 2.0$ to determine the dispersion relation

Supplemental Material: Scale-invariant phase transition of disordered bosons in one dimension

by numerically analyzing the spectral peaks after performing an analytic continuation of the imaginary-frequency dynamic structure factor [114, 113].

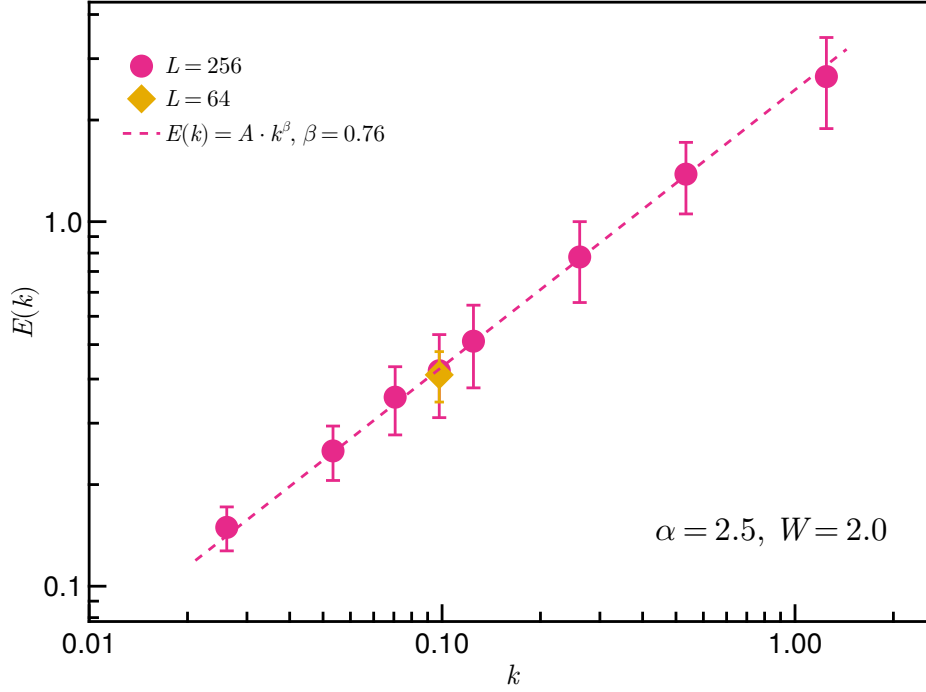


Fig. A.1 Dispersion relation $E(k)$ vs k for $\alpha = 2.5$ in the superfluid phase at finite disorder strength $W/t = 2.0$.

Our results, presented in Figure A.1 of this Supplemental Material, demonstrate that the spectrum is non-linear in k for $\alpha = 2.5$ at $W = 2.0$ and the data is well described by $E(k) \sim k^{z_*}$, with $z_* \simeq 0.76$. We checked for finite size effects (e.g., $L = 64$ in the figure), founding no significant impact. These results contradict the theoretical predictions of linear dispersion proposed in [126].

Appendix B

Supplemental Material: Bose-Hubbard model with power-law hopping in one dimension

In this chapter, we provide a detailed discussion of the single-particle density matrix, $\mathcal{G}(\ell)$, for a system of hardcore bosons confined to a one-dimensional (1D) lattice with power-law hopping for $1 < \alpha \leq 3$. Here, we focus on the condensate fraction, which we estimate by analyzing the behavior of the asymptotic tail of $\mathcal{G}(\ell)$. Furthermore, we present the large- ℓ asymptotic behavior of $\mathcal{G}(\ell)$, comparing two distinct fitting models: a pure power-law decay characterized by the expression $A \cdot \ell^{-\gamma}$, and a more complex model combining a constant term with a power-law decay, expressed as $A + B \cdot \ell^{-\gamma}$. Additionally, we extend our analysis by providing data for $\mathcal{G}(\ell)$ in the case of a 1D system of softcore bosons at unit filling in the superfluid phase near Mott insulator-superfluid (MI-SF) phase transition.

B.1 One-body density matrix for hardcore bosons on 1D lattice

In dimensions, $d \geq 3$, superfluidity is accompanied by Bose-Einstein condensation (BEC) where a finite fraction of bosons occupy a single particle state. The off-diagonal elements of the one-body density matrix (OBDM) $\mathcal{G}(\ell) = \langle b_i^\dagger b_{i+\ell} \rangle$, therefore, develop a long tail and approach a constant for large distances ℓ . In BEC, the condensate fraction, n_0 , is proportional to the limiting value of the $\mathcal{G}(\ell)$ at large distances, $n_0 \sim \lim_{\ell \rightarrow \infty} \mathcal{G}(\ell)$. For systems exhibiting long-range order (LRO), $\mathcal{G}(\ell)$ approaches a constant as ℓ increases, signifying a finite condensate

Supplemental Material: Bose-Hubbard model with power-law hopping in one dimension

fraction. For one dimension systems, the low energy phenomenon is expected to follow predictions of Luttinger Liquid (LL) theory [166] and undergo a Berezinskii–Kosterlitz–Thouless (BKT) transition [35, 36, 66, 140]. The OBDM for short-range interactions in 1D superfluids algebraically decays as a power-law $\langle b_i^\dagger b_{i+l} \rangle \sim l^{-K/2}$ showing quasi long-range order (QLRO). In such scenario, condensate fraction n_0 also decays to zero as a power-law. If the decay of the interaction is sufficiently slow, long-range (LR) effects can influence the universal critical properties and may even induce spontaneous symmetry breaking (SSB) in low-dimensional systems. This occurs because the well-known Hohenberg-Mermin-Wagner theorem, which prohibits SSB in low dimensions with short-range interactions, does not apply when LR couplings are present[167].

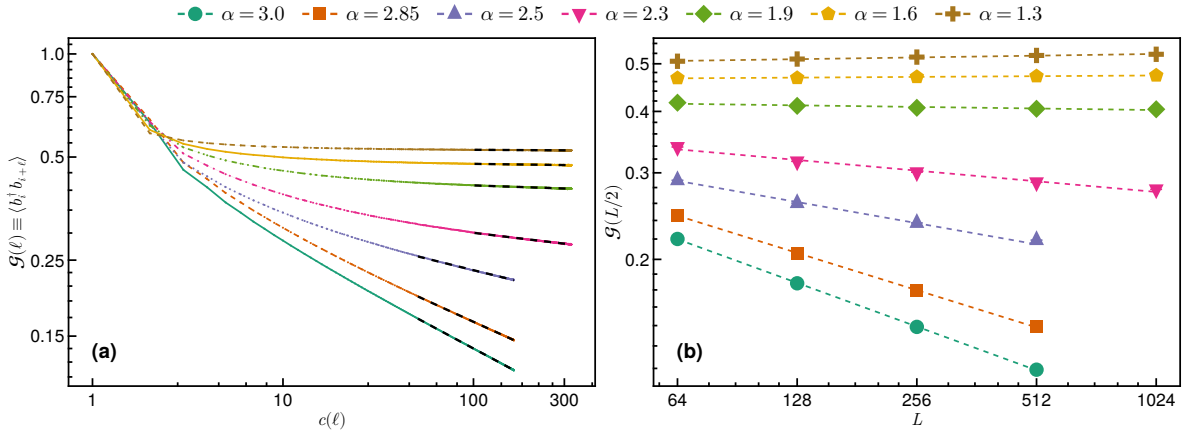


Fig. B.1 (a) Correlation function or single-particle density matrix $\mathcal{G}(\ell)$ vs chord distance $c(\ell)$. The black dashed line represents the best fit to $A \cdot c(\ell)^{-\gamma}$ showing long-range order for $\alpha \leq 2.0$ and an algebraic decay for $\alpha > 2.0$. (b) $\mathcal{G}(L/2)$ vs L showing power-law decay for $\alpha > 2$.

B.1.1 Condensate Fraction

We perform large scale quantum Monte Carlo simulations of a 1D system of hardcore bosons with power-law hopping $1/r^\alpha$ in the path-integral representation in the grand-canonical ensemble using the worm algorithm for system sizes as large as $L = 1024$. Worm algorithm allows for efficient sampling $\mathcal{G}(\ell)$. Figure B.1(a) shows the single-particle density matrix $\mathcal{G}(\ell)$ as a function of the chord distance $c(\ell) = \sin(\pi\ell/L)$, which is used to take care of periodic boundary conditions. It confirms the power-law decay of the Green function for $\alpha > 2$ and long-range order for $\alpha \leq 2.0$. The condensate fraction for a finite size system is given by the tail of (ℓ) given by $n_0 = \mathcal{G}(L/2)$. Figure B.1(b) represents $\mathcal{G}(L/2)$ as a function of lattice size

B.1 One-body density matrix for hardcore bosons on 1D lattice

L showing that the tail of the Green function decays to zero in the thermodynamic limit for $\alpha > 2$, further confirming that there is no long-range order in the system – at least up to the considered lengths. For $\alpha \leq 2$, the condensate fraction reaches a constant value indicating long-range order.

B.1.2 Fitting of $\mathcal{G}(\ell)$

Figure B.2 illustrates the single-particle density matrix, $\mathcal{G}(\ell)$, as a function of $c(\ell)$ for the case where $\alpha = 2.3$. This figure provides a comprehensive comparison of two distinct fitting methodologies: a standard power-law fit and a power-law fit with an additional constant term. In panel (a), the dashed black line represents a power-law fit to the data, expressed as $A \cdot c(\ell)^{-\gamma}$. This form attempts to capture the decay of $\mathcal{G}(\ell)$ over the range of distances, with the inset providing an estimate of the power-law exponent γ . This exponent is determined by fitting $\mathcal{G}(\ell)$ over the interval from $\ell = x_{\min}$ to $\ell = L/2$, where x_{\min} is defined as a fraction of the total system size, i.e., $x_{\min} = x_{\min} \text{ fraction} \times L/2$. In panel (b), a more elaborate fitting model is considered, where the power-law is supplemented by a constant term, resulting in the functional form $A \cdot c(\ell)^{-\gamma} + B$. The dashed black line illustrates this fit to the data, and the inset again shows the estimated power-law exponent γ , obtained by fitting the same range of ℓ .

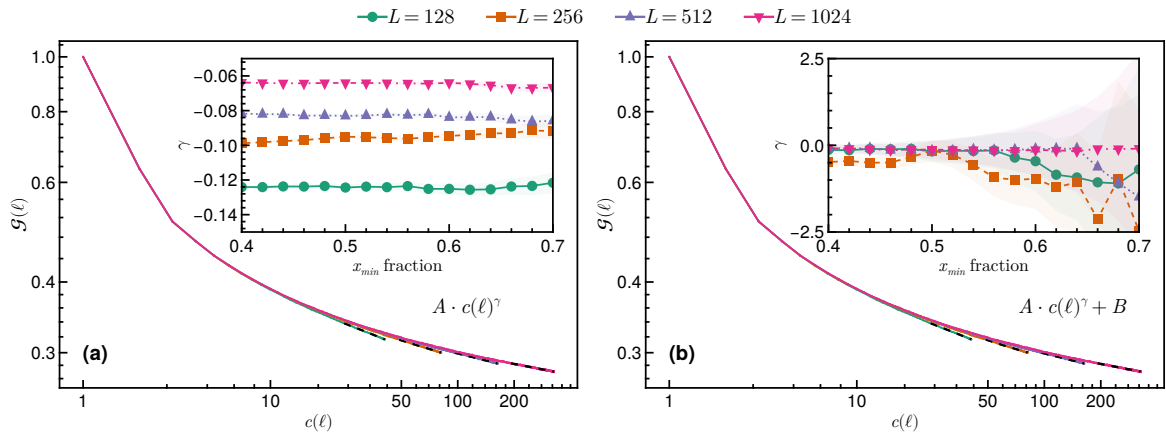


Fig. B.2 Single-particle density matrix, $\mathcal{G}(\ell)$, plotted against $c(\ell)$ for $\alpha = 2.3$. (a) The dashed black line represents the power-law fit $A \cdot c(\ell)^{-\gamma}$ to $\mathcal{G}(\ell)$. Inset: Power-law exponent γ estimated by fitting $\mathcal{G}(\ell)$ from $\ell = x_{\min}$ to $\ell = L/2$ where $x_{\min} = x_{\min} \text{ fraction} \times L/2$. (b) The dashed black line represents the power-law fit with additional constant $A \cdot c(\ell)^{-\gamma} + B$ to $\mathcal{G}(\ell)$. Inset: Power-law exponent γ estimated by fitting $\mathcal{G}(\ell)$ from $\ell = x_{\min}$ to $\ell = L/2$.

Both the simple power-law and the extended constant-plus-power-law fits are found to be equally effective in describing the overall behavior of $\mathcal{G}(\ell)$. However, the simple power-law fit

Supplemental Material: Bose-Hubbard model with power-law hopping in one dimension

demonstrates significantly greater stability and robustness. It fits the tail of the data equally well over a broad range of x_{\min} fractions, from 0.2 to 0.8, indicating that the exponent γ derived from this fit remains consistent and reliable across various fitting windows. In contrast, the extended fit that includes the additional constant term introduces instability in the estimation of the exponent. The value of γ fluctuates substantially depending on the choice of x_{\min} , and in the large- ℓ limit, the fit becomes unreliable. This variability renders the constant-plus-power-law fit impractical for accurately capturing the asymptotic, long-range behavior of $\mathcal{G}(\ell)$.

B.2 Single particle density matrix for softcore bosons on 1D lattice

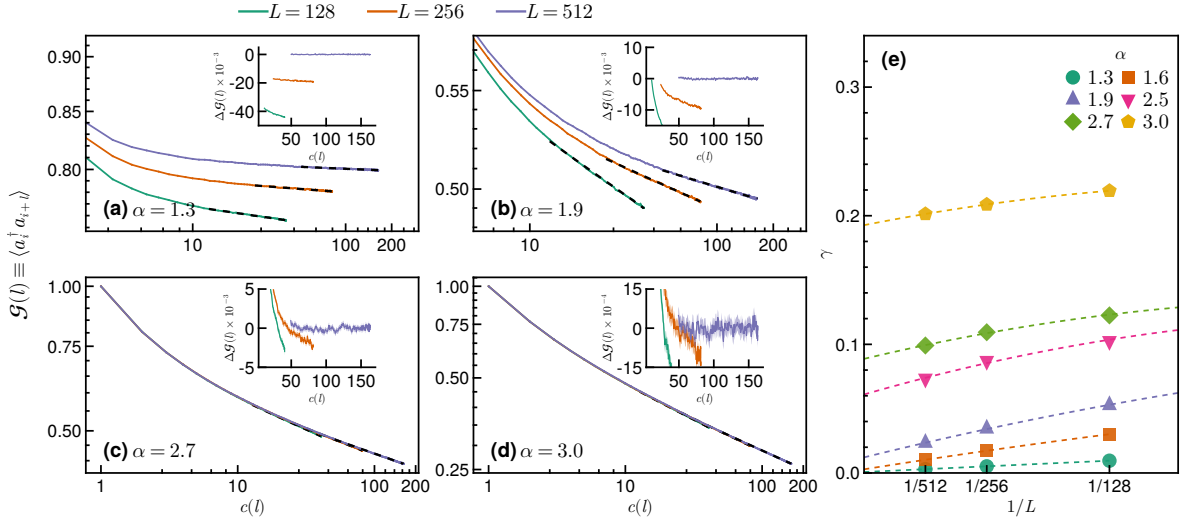


Fig. B.3 Characterization of the superfluid phase near MI-SF phase transition: (a)-(d) Single-particle density matrix, $\mathcal{G}(\ell)$, plotted against ℓ for $\alpha = 1.3, 1.9, 2.7,$ and 3.0 . The dashed line represents the best fit to $A \cdot c(\ell)^{-\gamma}$, where $c(\ell) = \sin(\pi\ell/L)$ is the chord distance, and A and γ are fitting parameters. For $\alpha = 1.3$ and 1.9 , $\mathcal{G}(\ell)$ saturates to a constant as $\ell \rightarrow \infty$. For $\alpha = 2.7$ and 3.0 , $\mathcal{G}(\ell)$ exhibits algebraic decay. Insets: Difference $\Delta \mathcal{G}(\ell)$ between $\mathcal{G}(\ell)$ for system size L and the numerical fit for $L = L_{\max}$, plotted as a function of the chord distance $c(\ell)$. The difference indicates an upward trend of $\mathcal{G}(\ell)$ for increasing lattice size. (e) Finite-size scaling of the power-law exponent γ to the thermodynamic limit.

In order to characterize the superfluid phase of a system of softcore bosons on a 1D lattice with power-law hopping, $\mathcal{G}(\ell)$ is estimated for $1 < \alpha \leq 3$ for lattice sizes upto $L = 512$. In Figure B.3, panels (a)-(d) display the single-particle density matrix, $\mathcal{G}(\ell)$, plotted as a function of ℓ for values of $\alpha = 1.3, 1.9, 2.7,$ and 3.0 . The dashed lines represent the best fit to the

B.2 Single particle density matrix for softcore bosons on 1D lattice

form $A \cdot c(\ell)^{-\gamma}$, where $c(\ell)$ is the chord distance, and A and γ are the fitting parameters. For $\alpha = 1.3$ and 1.9 , $\mathcal{G}(\ell)$ saturates to a constant as ℓ approaches infinity, indicating long-range order. In contrast, for $\alpha = 2.7$ and 3.0 , $\mathcal{G}(\ell)$ exhibits an algebraic decay, reflecting quasi-long-range order. The insets in each panel display the difference $\Delta\mathcal{G}(\ell)$ between $\mathcal{G}(\ell)$ for a system size L and the numerical fit for the maximum system size $L = L_{\max}$, plotted as a function of the chord distance $c(\ell)$. This difference reveals an upward trend in $\mathcal{G}(\ell)$ with increasing lattice size. Panel (e) illustrates the finite-size scaling of the power-law exponent γ as it approaches the thermodynamic limit. The fitted values of γ are plotted vs $1/L$, showing values consistent with $\gamma = 0$ for $1 < \alpha \lesssim 2$ and $\gamma > 0$ for $2 \lesssim \alpha \leq 3$ in the thermodynamic limit.

List of figures

- 1 Caractérisation de la phase superfluide pour $W/t = 0$: (a) Matrice de densité à une particule $\mathcal{G}(\ell)$ en fonction de la distance ℓ , montrant une décroissance algébrique pour toutes les valeurs de α avec $L = 256$. Les lignes pointillées indiquent le meilleur ajustement avec $A \cdot c(\ell)^{-\gamma}$, où $c(\ell) = \sin(\pi\ell/L)/\sin(\pi/L)$ est la distance de corde et A, γ sont des paramètres d'ajustement. (c) Évaluation numérique du paramètre de liquide de Luttinger K en fonction de α , à partir de la décroissance en loi de puissance $\mathcal{G} \propto \ell^{-1/(2K)}$ (points verts) et de la relation $K = \pi\sqrt{\kappa Y_s}$ (carrés rouges), extrapolée à la limite thermodynamique via une mise à l'échelle polynomiale en $1/L$ xii
- 2 Caractérisation de la transition de la phase superfluide à la phase non-superfluide pour \mathcal{H}_1 : (a) Nombre moyen des carrés d'enroulement $\langle \mathcal{W}^2 \rangle$ en fonction de la force du désordre W/t pour $\alpha = 2.7$ (symboles vides) et 3.2 (symboles pleins) pour les tailles de système $L = 64, 128, 256$. (b)-(e) Zoom sur la zone près des transitions de phase pour $\alpha = 2.5, 2.7, 3.0$ et 3.2, montrant le croisement entre les courbes ; la courbe correspondant à la plus grande taille est soustraite de toutes les données pour plus de clarté. Les barres d'erreur verticales indiquent l'incertitude estimée provenant des simulations Monte Carlo et des moyennes sur le désordre. Insets : Mise à l'échelle de la taille finie des points de croisement entre les courbes pour les tailles de système L_1 et $L_2 = 2L_1$ en fonction de $L = L_1$ xiii

List of figures

- 3 Caractérisation de la phase superfluide : (a)-(d) Matrice de densité à une particule $\mathcal{G}(l)$ en fonction de l pour $\alpha = 1.3, 1.9, 2.5,$ et 2.7 . La ligne en pointillés indique le meilleur ajustement avec $A \cdot c(l)^{-\gamma}$ où $c(l) = \sin(\pi l/L)$ est la distance de corde et A, γ sont les paramètres d'ajustement. Inset : $\Delta\mathcal{G}(l) = \mathcal{G}(l) - \mathcal{G}_{fit}$ est la différence entre les valeurs réelles de la matrice de densité à une particule et l'ajustement théorique G_{fit} pour L_{max} . La différence indique une tendance à la hausse de $\mathcal{G}(l)$ avec l'augmentation de la taille du réseau. (e) Échelle thermodynamique de l'exposant de loi de puissance γ , indiquant un véritable Ordre de Longue Portée (LRO) pour $\alpha \leq 2 \pm 0.1$ xiv
- 4 Diagramme de phase de l'état fondamental du modèle de Bose-Hubbard en 1D avec des sauts suivant une loi de puissance (Equation (2)) pour $\alpha = 1.6, 1.9, 2.5, 2.7,$ et 3.0 , montrant la frontière entre les régions d'isolant de Mott (avec une densité unitaire) et de superfluide en fonction du potentiel chimique μ/U et de l'amplitude de saut t/U xvi
- 1.1 (a) The excitation spectrum for a weakly interacting Bose gas, where the energy $\varepsilon(p)$ is given by $\varepsilon(p) = \frac{p^2}{2m} + gn$ (dashed curve), with a linear phonon-like dispersion $\varepsilon(p) = cp$ (solid line) at low momenta, indicating that the critical velocity v_c is equal to the sound velocity c . (b) The excitation spectrum for a strongly interacting Bose liquid such as ${}^4\text{He}$, showing a more complex structure with phonon, maxon, and roton branches. Here, the critical velocity v_c is less than the sound velocity c , reflecting the presence of a local minimum in the dispersion relation due to roton excitations. Taken from [30]. 7

1.2	Schematic phase diagram illustrating different phases of a two-dimensional trapped weakly interacting dilute Bose gas as a function of temperature T . Here, ρ_0 represents the density of the condensate, ρ_s denotes the superfluid density, and ρ_{MF} is the mean-field density, estimated through perturbative methods. The temperature T_{BEC} marks the crossover from the superfluid regime to a true Bose-Einstein condensate phase. T_{BKT} indicates the critical temperature of the Berezinskii-Kosterlitz-Thouless (BKT) transition, at which topological order emerges in the form of vortex-antivortex pairs. T_{MF} denotes the onset of the mean-field critical region. Regions I through IV depict different physical regimes: below T_{BEC} (Region I), the system exhibits condensation; between T_{BEC} and T_{BKT} (Region II), it transitions toward a superfluid state; between T_{BKT} and T_{MF} (Region III), the mean-field description becomes increasingly accurate; and above T_{MF} (Region IV), thermal fluctuations dominate [37].	8
1.3	The phase diagram of the one-dimensional Bose-Hubbard model displays the superfluid phase (SF) and the Mott insulator phase (MI) with density one. Solid lines represent a Padé analysis of 12th-order strong-coupling expansions, while the boxed regions indicate Quantum Monte Carlo (QMC) data. Circles denote Density Matrix Renormalization Group (DMRG) results, and dashed lines mark the regions of integer density. The error bars in the μ -direction are smaller than the circles, reflecting minimal uncertainty, while the error bars in the t -direction represent the uncertainty in determining the Berezinskii-Kosterlitz-Thouless (BKT) transition. [44]	11
1.4	Visualization of the Berezinskii–Kosterlitz–Thouless (BKT) transition: at low temperatures, vortex–antivortex pairs remain bound, maintaining quasi-long-range order. As temperature approaches the critical BKT temperature T_{BKT} , the pairs unbind, creating free vortices that disrupt quasi-ordered system and lead to a phase transition.	14
2.1	Illustration of Monte Carlo integration to estimate the unknown area of a pond enclosed by a rectangle of known area A . (a) Direct sampling — random points are uniformly scattered across the entire rectangle.(b) Markov chain Monte Carlo sampling — a chain of correlated samples gradually explores the pond’s area, with each new point dependent on the previous one. The crossed-out point indicates an invalid step that was rejected.	30

List of figures

- 2.2 A worldline representation of a term in the partition function from Eq. (1), illustrating state evolution across lattice sites in imaginary time. The horizontal axis spans imaginary time from 0 to β , with discrete time points τ_1 through τ_4 marking instances of state transitions. The vertical axis represents different lattice sites. The system begins in state $|\psi_0\rangle$ at imaginary time $\tau = 0$, evolves to $|\psi_3\rangle$ at time τ_3 , and subsequently returns to $|\psi_0\rangle$. Bold horizontal lines indicate imaginary time evolution of states, while vertical jumps signify transitions between states. Off-diagonal Hamiltonian terms, such as $\langle\psi_1|V|\psi_0\rangle$, enable these transitions, while exponential terms like $e^{-(\tau_3-\tau_2)E_2}$ describe imaginary-time evolution governed by diagonal components of the Hamiltonian. 37
- 2.3 Example of a worldline configuration with periodic boundary conditions, showing a winding number $\mathcal{W} = 1$. This winding is characterized by the particle path (boson depicted as yellow dot) looping around the spatial boundary in imaginary time, starting and ending at the same lattice site while maintaining periodicity in imaginary time. Horizontal segments represent imaginary time evolution on the same lattice site, and vertical segments indicate boson jumping between sites, illustrating how the worldline completes a loop through the boundary conditions. 38
- 2.4 Graphical representation of an extended worldline configuration in the \mathcal{G} sector which includes the worm heads named *Ira* (green) and *Masha* (red). 41
- 3.1 Characterization of the superfluid phase for $W/t = 0$: (a) Dispersion relations $E(k)$ vs k for $\alpha = 2.5, 3.0$ and 3.2 chosen in the intermediate and short-range regimes, respectively (see text) for $L = 256$. (b) Single particle density matrix $\mathcal{G}(\ell)$ vs chord distance $c(\ell) = \sin(\pi\ell/L)/\sin(\pi/L)$ showing an algebraic decay for all α for $L = 512$. Dashed lines indicate the best fit with $A \cdot c(\ell)^{-\gamma}$ where A, γ are fitting parameters. (c) Numerical evaluation of the Luttinger liquid parameter K as a function of α from the power-law decay $\mathcal{G} \propto \ell^{-1/(2K)}$ (green dots) and from the relation $K = \pi\sqrt{\kappa\bar{Y}_s}$ (red squares) extrapolated to the thermodynamic limit via a polynomial scaling in $1/L$ 49

3.2	Characterization of the superfluid to non-superfluid phase transition: (a) Mean-square winding number $\langle \mathcal{W}^2 \rangle$ vs disorder strength W/t for $\alpha = 2.7$ (empty symbols) and 3.2 (full symbols) for system sizes $L = 64, 128, 256$. (b)-(e) Zoom-in on the area near phase transitions for $\alpha = 2.5, 2.7, 3.0$ and 3.2, showing crossing between the curves; the curve corresponding to the largest size $L = 1024$ is subtracted from all data for clarity. Vertical error bars indicate the estimated uncertainty from the Monte Carlo simulations and disorder-averages. Insets: Finite-size scaling of crossings points between curves for system sizes L_1 and $L_2 = 2L_1$ as a function of $L = L_1$	51
3.3	(a) Phase diagram, W_c vs α , of the superfluid and non-superfluid quantum phases for model (4.1). (b) Critical values of LL parameter K_c at W_c vs α , as estimated from the power-law decay of \mathcal{G} (green dots) and from $K = \pi\sqrt{\kappa Y_s}$ (red squares) for $L = 256$	52
3.4	(a)-(c) Data collapse for the scaled superfluid stiffness $L^{-\zeta/\nu} Y_s$ vs $L^{1/\nu} [(W/t) - (W_c/t)]$ for $\alpha = 2.5, 2.7$ and 3.0 using $L = 64, 128, 256$. The fitted values of the correlation length exponent ν and ζ are reported directly in the figure. They satisfy $\nu \gtrsim 2$ for all α	53
3.5	Data collapse for the scaled superfluid stiffness $L^{-\zeta/\nu} Y_s$ vs $L^{1/\nu} [(W/t) - (W_c/t)]$ for $\alpha = 3.2$ using $L = 64, 128, 256$. The fitted values of the correlation length exponent ν and ζ are reported directly in the figure. Unlike for $\alpha < 3$, this scaling corresponds here to a finite-size effect, as the transition is not located at $W_c/t = 0.57$ and slowly shifts to $W_c/t = 0$, see Fig. 3.2(e).	54
4.1	Ground state phase diagram of the 1D Bose-Hubbard model with power-law hopping for $\alpha = 1.6, 1.9, 2.5, 2.7$, and 3.0, showing the boundary between the Mott insulator (at unity filling) and superfluid phases as a function of chemical potential μ/U and hopping amplitude t/U . Markers represent simulation data, while the solid black line (for $\alpha = 1.6$) and the dashed black line (for $\alpha = 1.9$) are obtained from fitting the energy gap Δ/t near the critical point as $\Delta/t \sim t/U - t/U_c ^{-z_*\nu}$ (see also Fig. 4.2 and text). Inset: Gap Energy Δ/t fitted as a function of $t/U - t/U_c$	60

List of figures

- 4.2 Dispersion relation $E(k)$ vs. k for $\alpha = 1.6, 1.9, 2.5,$ and 2.7 in the superfluid phase near the transition along the commensurate density line. Symbols denote numerical data obtained from fitting the long-time exponential decay of $G(k, \tau)$, while lines show the spin-wave analysis prediction $E(k) \sim k^{z_*}$, with $z_* = (\alpha - 1)/2$ [125]. Inset: Single-particle Green function $G(k, \tau)$ for $k = \pi/64$ (represented by empty markers) and $\alpha = 1.6, 1.9, 2.5,$ and 2.7 . The black dashed line represents the numerical fit to the exponential decay. 61
- 4.3 Characterization of the Mott insulator to superfluid phase transition: (a)-(b) Mean-square winding number $\langle \mathcal{W}^2 \rangle$ vs t/U for $\alpha = 1.6$ and 2.7 near phase transitions, showing crossing between the curves; the curve corresponding to the largest lattice size is subtracted from all data for clarity. Vertical error bars indicate the estimated uncertainty from the Monte Carlo simulations. Insets: Finite-size scaling of crossings points between curves for system sizes L_1 and $L_2 = 2L_1$ as a function of $L = L_1$. (c) Phase diagram, t/U_c vs α of the Mott insulator and superfluid quantum phases for model (4.1). 62
- 4.4 Superfluid stiffness Y_s near the critical interaction strength t/U_c for $\alpha = 1.6, 1.9$ and 2.7 and lattice size $L = 128, 256, 512$. Inset: Data collapse for the scaled superfluid stiffness $L^{-\zeta/\nu} Y_s$ vs $L^{1/\nu} [(t/U) - (t/U_c)]$. The fitted values of the correlation length exponent ν are directly reported in the inset. For $\alpha = 1.6$ and 1.9 , ν is consistent with the value derived by fitting energy gap Δ . (see Figure 4.1) 63
- 4.5 Characterization of the superfluid phase: (a)-(d) Single-particle density matrix, $\mathcal{G}(\ell)$, plotted against ℓ for $\alpha = 1.3, 1.6, 2.5,$ and 2.7 . The dashed line represents the best fit to $A \cdot c(\ell)^{-\gamma}$, where $c(\ell) = \sin(\pi\ell/L)$ is the chord distance, and A and γ are fitting parameters. For $\alpha = 1.3$ and 1.9 , $\mathcal{G}(\ell)$ saturates to a constant as $\ell \rightarrow \infty$. For $\alpha = 2.5$ and 2.7 , $\mathcal{G}(\ell)$ exhibits algebraic decay. Insets: Difference $\Delta\mathcal{G}(\ell)$ between $\mathcal{G}(\ell)$ for system size L and the numerical fit for $L = L_{\max}$, plotted as a function of the chord distance $c(\ell)$. The difference indicates an upward trend of $\mathcal{G}(\ell)$ for increasing lattice size. (e) Finite-size scaling of the power-law exponent γ to the thermodynamic limit. 64
- A.1 Dispersion relation $E(k)$ vs k for $\alpha = 2.5$ in the superfluid phase at finite disorder strength $W/t = 2.0$ 72

B.1	(a) Correlation function or single-particle density matrix $\mathcal{G}(\ell)$ vs chord distance $c(\ell)$. The black dashed line represents the best fit to $A \cdot c(\ell)^{-\gamma}$ showing long-range order for $\alpha \leq 2.0$ and an algebraic decay for $\alpha > 2.0$. (b) $\mathcal{G}(L/2)$ vs L showing power-law decay for $\alpha > 2$	74
B.2	Single-particle density matrix, $\mathcal{G}(\ell)$, plotted against $c(\ell)$ for $\alpha = 2.3$. (a) The dashed black line represents the power-law fit $A \cdot c(\ell)^{-\gamma}$ to $\mathcal{G}(\ell)$. Inset: Power-law exponent γ estimated by fitting $\mathcal{G}(\ell)$ from $\ell = x_{\min}$ to $\ell = L/2$ where $x_{\min} = x_{\min} \text{ fraction} \times L/2$. (b) The dashed black line represents the power-law fit with additional constant $A \cdot c(\ell)^{-\gamma} + B$ to $\mathcal{G}(\ell)$. Inset: Power-law exponent γ estimated by fitting $\mathcal{G}(\ell)$ from $\ell = x_{\min}$ to $\ell = L/2$	75
B.3	Characterization of the superfluid phase near MI-SF phase transition: (a)-(d) Single-particle density matrix, $\mathcal{G}(\ell)$, plotted against ℓ for $\alpha = 1.3, 1.9, 2.7$, and 3.0 . The dashed line represents the best fit to $A \cdot c(\ell)^{-\gamma}$, where $c(\ell) = \sin(\pi\ell/L)$ is the chord distance, and A and γ are fitting parameters. For $\alpha = 1.3$ and 1.9 , $\mathcal{G}(\ell)$ saturates to a constant as $\ell \rightarrow \infty$. For $\alpha = 2.7$ and 3.0 , $\mathcal{G}(\ell)$ exhibits algebraic decay. Insets: Difference $\Delta\mathcal{G}(\ell)$ between $\mathcal{G}(\ell)$ for system size L and the numerical fit for $L = L_{\max}$, plotted as a function of the chord distance $c(\ell)$. The difference indicates an upward trend of $\mathcal{G}(\ell)$ for increasing lattice size. (e) Finite-size scaling of the power-law exponent γ to the thermodynamic limit. .	76

Bibliography

- [1] Bo Yan, Steven A Moses, Bryce Gadway, Jacob P Covey, Kaden RA Hazzard, Ana Maria Rey, Deborah S Jin, and Jun Ye. Observation of dipolar spin-exchange interactions with lattice-confined polar molecules. *Nature*, 501(7468):521–525, 2013.
- [2] Philip Richerme, Zhe-Xuan Gong, Aaron Lee, Crystal Senko, Jacob Smith, Michael Foss-Feig, Spyridon Michalakis, Alexey V. Gorshkov, and Christopher Monroe. Non-local propagation of correlations in quantum systems with long-range interactions. *Nature*, 511(7508):198–201, July 2014.
- [3] P. Jurcevic, B. P. Lanyon, P. Hauke, C. Hempel, P. Zoller, R. Blatt, and C. F. Roos. Quasiparticle engineering and entanglement propagation in a quantum many-body system. *Nature*, 511(7508):202–205, July 2014.
- [4] Lei Feng, Or Katz, Casey Haack, Mohammad Maghrebi, Alexey V. Gorshkov, Zhexuan Gong, Marko Cetina, and Christopher Monroe. Continuous symmetry breaking in a trapped-ion spin chain, 2022.
- [5] Johannes Zeiher, Jae-yoon Choi, Antonio Rubio-Abadal, Thomas Pohl, Rick van Bijnen, Immanuel Bloch, and Christian Gross. Coherent many-body spin dynamics in a long-range interacting ising chain. *Phys. Rev. X*, 7:041063, Dec 2017.
- [6] T. Giamarchi and H. J. Schulz. Anderson localization and interactions in one-dimensional metals. *Phys. Rev. B*, 37:325–340, Jan 1988.
- [7] Thierry Giamarchi. *Quantum Physics in One Dimension*. Oxford University Press, December 2003.
- [8] Tanul Gupta, Guido Masella, Francesco Mattiotti, Nikolay V. Prokof'ev, and Guido Pupillo. Scale-invariant phase transition of disordered bosons in one dimension, 2023.
- [9] Nicolò Defenu, Tobias Donner, Tommaso Macrì, Guido Pagano, Stefano Ruffo, and Andrea Trombettoni. Long-range interacting quantum systems. *Reviews of Modern Physics*, 95(3):035002, August 2023.
- [10] N. V. Prokof'ev, B. V. Svistunov, and I. S. Tupitsyn. Exact, complete, and universal continuous-time worldline Monte Carlo approach to the statistics of discrete quantum systems. *Journal of Experimental and Theoretical Physics*, 87(2):310–321, August 1998.
- [11] Werner Krauth. *Statistical Mechanics: Algorithms and Computations*. Oxford University PressOxford, September 2006.

Bibliography

- [12] Tanul Gupta, Nikolay V. Prokof'ev, and Guido Pupillo. Bose-Hubbard model with power-law hopping in one dimension, 2024.
- [13] Mohammad F. Maghrebi, Zhe-Xuan Gong, and Alexey V. Gorshkov. Continuous Symmetry Breaking in 1D Long-Range Interacting Quantum Systems. *Physical Review Letters*, 119(2):023001, July 2017.
- [14] Mark B. Hindmarsh, Marvin Lüben, Johannes Lumma, and Martin Pauly. Phase transitions in the early universe. 2020.
- [15] S. L. Sondhi, S. M. Girvin, J. P. Carini, and D. Shahar. Continuous quantum phase transitions. *Reviews of Modern Physics*, 69(1):315–333, January 1997.
- [16] R. M. Bradley and S. Doniach. Quantum fluctuations in chains of Josephson junctions. *Physical Review B*, 30(3):1138–1147, August 1984.
- [17] M.-S. Choi, J. Yi, M. Y. Choi, J. Choi, and S.-I. Lee. Quantum phase transitions in Josephson-junction chains. *Physical Review B*, 57(2):R716–R719, January 1998.
- [18] M. Bard, I. V. Protopopov, I. V. Gornyi, A. Shnirman, and A. D. Mirlin. Superconductor-insulator transition in disordered Josephson-junction chains. *Physical Review B*, 96(6):064514, August 2017.
- [19] Subir Sachdev. *Quantum Phase Transitions*. Cambridge University Press, Cambridge New York, second edition edition, 2011.
- [20] N.F. Mott. Doped antiferromagnetic insulators : A model for high temperature superconductivity. *Journal de Physique*, 50(18):2811–2822, 1989.
- [21] Tianxing Ma, Da Wang, and Congjun Wu. Doping-driven antiferromagnetic insulator-superconductor transition: A quantum Monte Carlo study. *Physical Review B*, 106(5):054510, August 2022.
- [22] Masatoshi Imada, Atsushi Fujimori, and Yoshinori Tokura. Metal-insulator transitions. *Reviews of Modern Physics*, 70(4):1039–1263, October 1998.
- [23] P. W. Anderson. Absence of Diffusion in Certain Random Lattices. *Physical Review*, 109(5):1492–1505, March 1958.
- [24] Matthew P. A. Fisher, Peter B. Weichman, G. Grinstein, and Daniel S. Fisher. Boson localization and the superfluid-insulator transition. *Physical Review B*, 40(1):546–570, July 1989.
- [25] Sébastien Balibar. The Discovery of Superfluidity. *Journal of Low Temperature Physics*, 146(5-6):441–470, March 2007.
- [26] L. Landau. Theory of the Superfluidity of Helium II. *Physical Review*, 60(4):356–358, August 1941.
- [27] A. J. Leggett. Superfluidity. *Reviews of Modern Physics*, 71(2):S318–S323, March 1999.

-
- [28] N Bogolubov. On the theory of superfluidity. *J. Phys*, 11:23, 1947.
- [29] R. P. Feynman. Superfluidity and Superconductivity. *Reviews of Modern Physics*, 29(2):205–212, April 1957.
- [30] Lev P. Pitaevskij and Sandro Stringari. *Bose-Einstein Condensation and Superfluidity*. Number 164 in International Series of Monographs on Physics. Oxford University Press, Oxford, 2016.
- [31] Oliver Penrose and Lars Onsager. Bose-Einstein Condensation and Liquid Helium. *Physical Review*, 104(3):576–584, November 1956.
- [32] James F Annett. *Superconductivity, Superfluids, and Condensates*. Oxford University Press Oxford, March 2004.
- [33] N. D. Mermin and H. Wagner. Absence of Ferromagnetism or Antiferromagnetism in One- or Two-Dimensional Isotropic Heisenberg Models. *Physical Review Letters*, 17(22):1133–1136, November 1966.
- [34] P. C. Hohenberg. Existence of Long-Range Order in One and Two Dimensions. *Physical Review*, 158(2):383–386, June 1967.
- [35] V. L. Berezinskii. Destruction of Long-range Order in One-dimensional and Two-dimensional Systems Possessing a Continuous Symmetry Group. II. Quantum Systems. *Soviet Journal of Experimental and Theoretical Physics*, 34:610, January 1972.
- [36] J M Kosterlitz and D J Thouless. Ordering, metastability and phase transitions in two-dimensional systems. *Journal of Physics C: Solid State Physics*, 6(7):1181–1203, April 1973.
- [37] Anna Posazhennikova. *Colloquium* : Weakly interacting, dilute Bose gases in 2D. *Reviews of Modern Physics*, 78(4):1111–1134, October 2006.
- [38] Thomas G. Kiely and Erich J. Mueller. Superfluidity in the one-dimensional Bose-Hubbard model. *Physical Review B*, 105(13):134502, April 2022.
- [39] H. A. Gersch and G. C. Knollman. Quantum Cell Model for Bosons. *Physical Review*, 129(2):959–967, January 1963.
- [40] H. A. Gersch and J. M. Tanner. Solid-Superfluid Transition in He 4 at Absolute Zero. *Physical Review*, 139(6A):A1769–A1782, September 1965.
- [41] J. F. Fernandez and H. A. Gersch. Effect of Attractive Forces on the Solid-Superfluid Transition in He 4 at Absolute Zero. *Physical Review*, 149(1):154–164, September 1966.
- [42] Konstantin V. Krutitsky. Ultracold bosons with short-range interaction in regular optical lattices. *Physics Reports*, 607:1–101, January 2016.
- [43] William J. Mullin. Cell Model of Quantum Liquids and Solids. I. Crystalline State. *Physical Review A*, 4(3):1247–1256, September 1971.
- [44] T. D. Kühner and H. Monien. Phases of the one-dimensional Bose-Hubbard model. *Physical Review B*, 58(22):R14741–R14744, December 1998.

Bibliography

- [45] Markus Greiner, Olaf Mandel, Tilman Esslinger, Theodor W. Hänsch, and Immanuel Bloch. Quantum phase transition from a superfluid to a Mott insulator in a gas of ultracold atoms. *Nature*, 415(6867):39–44, January 2002.
- [46] Thilo Stöferle, Henning Moritz, Christian Schori, Michael Köhl, and Tilman Esslinger. Transition from a Strongly Interacting 1D Superfluid to a Mott Insulator. *Physical Review Letters*, 92(13):130403, March 2004.
- [47] I. Spielman, W. Phillips, and J. Porto. Mott-Insulator Transition in a Two-Dimensional Atomic Bose Gas. *Physical Review Letters*, 98(8):080404, February 2007.
- [48] Martin C. Gutzwiller. Effect of Correlation on the Ferromagnetism of Transition Metals. *Physical Review Letters*, 10(5):159–162, March 1963.
- [49] K. Sengupta and N. Dupuis. Mott-insulator-to-superfluid transition in the Bose-Hubbard model: A strong-coupling approach. *Physical Review A*, 71(3):033629, March 2005.
- [50] Dirk-Sören Lühmann. Cluster Gutzwiller method for bosonic lattice systems. *Physical Review A*, 87(4):043619, April 2013.
- [51] Antoine Georges, Gabriel Kotliar, Werner Krauth, and Marcelo J. Rozenberg. Dynamical mean-field theory of strongly correlated fermion systems and the limit of infinite dimensions. *Reviews of Modern Physics*, 68(1):13–125, January 1996.
- [52] Peter Anders, Emanuel Gull, Lode Pollet, Matthias Troyer, and Philipp Werner. Dynamical mean-field theory for bosons. *New Journal of Physics*, 13(7):075013, July 2011.
- [53] S.I. Mistakidis, A.G. Volosniev, R.E. Barfknecht, T. Fogarty, Th. Busch, A. Foerster, P. Schmelcher, and N.T. Zinner. Few-body Bose gases in low dimensions—A laboratory for quantum dynamics. *Physics Reports*, 1042:1–108, November 2023.
- [54] Martin Ebert, Artem Volosniev, and Hans-Werner Hammer. Two cold atoms in a time-dependent harmonic trap in one dimension. *Annalen der Physik*, 528(9-10):693–704, October 2016.
- [55] X. Y. Yin, Yangqian Yan, and D. Hudson Smith. Dynamics of small trapped one-dimensional Fermi gas under oscillating magnetic fields. *Physical Review A*, 94(4):043639, October 2016.
- [56] Corinna Kollath, Andreas M. Läuchli, and Ehud Altman. Quench Dynamics and Nonequilibrium Phase Diagram of the Bose-Hubbard Model. *Physical Review Letters*, 98(18):180601, April 2007.
- [57] B Bauer, L D Carr, H G Evertz, A Feiguin, J Freire, S Fuchs, L Gamper, J Gukelberger, E Gull, S Guertler, A Hehn, R Igarashi, S V Isakov, D Koop, P N Ma, P Mates, H Matsuo, O Parcollet, G Pawłowski, J D Picon, L Pollet, E Santos, V W Scarola, U Schollwöck, C Silva, B Surer, S Todo, S Trebst, M Troyer, M L Wall, P Werner, and S Wessel. The ALPS project release 2.0: Open source software for strongly correlated systems. *Journal of Statistical Mechanics: Theory and Experiment*, 2011(05):P05001, May 2011.

-
- [58] Phillip Weinberg and Marin Bukov. QuSpin: A Python package for dynamics and exact diagonalisation of quantum many body systems part I: Spin chains. *SciPost Physics*, 2(1):003, February 2017.
- [59] U. Schollwöck. The density-matrix renormalization group. *Reviews of Modern Physics*, 77(1):259–315, April 2005.
- [60] Ulrich Schollwöck. The density-matrix renormalization group in the age of matrix product states. *Annals of Physics*, 326(1):96–192, January 2011.
- [61] Richard T. Scalettar, Ghassan George Batrouni, and Gergely T. Zimanyi. Localization in interacting, disordered, Bose systems. *Physical Review Letters*, 66(24):3144–3147, June 1991.
- [62] S. Trotzky, L. Pollet, F. Gerbier, U. Schnorrberger, I. Bloch, N. V. Prokof'ev, B. Svistunov, and M. Troyer. Suppression of the critical temperature for superfluidity near the Mott transition. *Nature Physics*, 6(12):998–1004, December 2010.
- [63] Boris V. Svistunov, Egor S. Babaev, and Nikolay V. Prokof'ev. *Superfluid States of Matter*. CRC Press, 0 edition, April 2015.
- [64] Lara Benfatto. The Berezinskii-Kosterlitz-Thouless Transition and its Application to Superconducting Systems.
- [65] Naoto Nagaosa. *Quantum Field Theory in Condensed Matter Physics*. Texts and Monographs in Physics. Springer, Berlin New York, 1999.
- [66] J M Kosterlitz. The critical properties of the two-dimensional xy model. *Journal of Physics C: Solid State Physics*, 7(6):1046–1060, March 1974.
- [67] Batyr Ilyas. Berezinskii-Kosterlitz-Thouless transition in superconductors.
- [68] Thierry Giamarchi. *Quantum Physics in One Dimension*. Oxford University Press, December 2003.
- [69] A. Campa, T. Dauxois, D. Fanelli, and S. Ruffo. *Physics of Long-Range Interacting Systems*. Oxford University Press Oxford, 1 edition, August 2014.
- [70] Guido Giachetti. *Novel Phases in Long-Range Many-Body Systems*. PhD thesis, ITA, September 2022.
- [71] J. Sak. Recursion Relations and Fixed Points for Ferromagnets with Long-Range Interactions. *Physical Review B*, 8(1):281–285, July 1973.
- [72] Shamik Gupta and Stefano Ruffo. The world of long-range interactions: A bird's eye view. *International Journal of Modern Physics A*, 32(09):1741018, March 2017.
- [73] M Joyce and T Worrakitpoonpon. Relaxation to thermal equilibrium in the self-gravitating sheet model. *Journal of Statistical Mechanics: Theory and Experiment*, 2010(10):P10012, October 2010.
- [74] S. Chandrasekhar. *Principles of Stellar Dynamics*. Dover Publications, Mineola, NY, dover phoenix ed edition, 2005.

Bibliography

- [75] D. Lynden-Bell. Statistical Mechanics of Violent Relaxation in Stellar Systems. *Monthly Notices of the Royal Astronomical Society*, 136(1):101–121, May 1967.
- [76] P. Hauke and L. Tagliacozzo. Spread of Correlations in Long-Range Interacting Quantum Systems. *Physical Review Letters*, 111(20):207202, November 2013.
- [77] J. Schachenmayer, B. P. Lanyon, C. F. Roos, and A. J. Daley. Entanglement Growth in Quench Dynamics with Variable Range Interactions. *Physical Review X*, 3(3):031015, September 2013.
- [78] Jens Eisert, Mauritz Van Den Worm, Salvatore R. Manmana, and Michael Kastner. Breakdown of Quasilocality in Long-Range Quantum Lattice Models. *Physical Review Letters*, 111(26):260401, December 2013.
- [79] Davide Vodola, Luca Lepori, Elisa Ercolessi, Alexey V. Gorshkov, and Guido Pupillo. Kitaev Chains with Long-Range Pairing. *Physical Review Letters*, 113(15):156402, October 2014.
- [80] L. Lepori, D. Vodola, G. Pupillo, G. Gori, and A. Trombettoni. Effective theory and breakdown of conformal symmetry in a long-range quantum chain. *Annals of Physics*, 374:35–66, November 2016.
- [81] Zongping Gong, Tommaso Guaita, and J. Ignacio Cirac. Long-Range Free Fermions: Lieb-Robinson Bound, Clustering Properties, and Topological Phases. *Physical Review Letters*, 130(7):070401, February 2023.
- [82] L Lepori and L Dell’Anna. Long-range topological insulators and weakened bulk-boundary correspondence. *New Journal of Physics*, 19(10):103030, October 2017.
- [83] Wei Zhu, Chao Han, Emilie Huffman, Johannes S. Hofmann, and Yin-Chen He. Uncovering Conformal Symmetry in the 3D Ising Transition: State-Operator Correspondence from a Quantum Fuzzy Sphere Regularization. *Physical Review X*, 13(2):021009, April 2023.
- [84] Emergent symmetry in a low-dimensional superconductor on the edge of Mottness.
- [85] Philippe Di Francesco, Pierre Mathieu, and David Sénéchal. *Conformal Field Theory*. Graduate Texts in Contemporary Physics. Springer, New York, 1997.
- [86] Giuseppe Mussardo. *Statistical Field Theory: An Introduction to Exactly Solved Models in Statistical Physics*. Ogt:C. Oxford University Press, New York, 2e edition, 2020.
- [87] Alexander M. Polyakov. Conformal symmetry of critical fluctuations. *JETP Lett.*, 12:381–383, 1970.
- [88] Joseph Polchinski. Scale and conformal invariance in quantum field theory. *Nuclear Physics B*, 303(2):226–236, June 1988.
- [89] Anatoly Dymarsky, Zohar Komargodski, Adam Schwimmer, and Stefan Theisen. On scale and conformal invariance in four dimensions. *Journal of High Energy Physics*, 2015(10):171, October 2015.

-
- [90] J L Cardy. Critical percolation in finite geometries. *Journal of Physics A: Mathematical and General*, 25(4):L201–L206, February 1992.
- [91] Catarina Cosme, J. M. Viana Parente Lopes, and João Penedones. Conformal symmetry of the critical 3D Ising model inside a sphere. *Journal of High Energy Physics*, 2015(8):22, August 2015.
- [92] Giacomo Gori and Andrea Trombettoni. Conformal invariance in three dimensional percolation. *Journal of Statistical Mechanics: Theory and Experiment*, 2015(7):P07014, July 2015.
- [93] Elliott H. Lieb and Derek W. Robinson. The finite group velocity of quantum spin systems. *Communications in Mathematical Physics*, 28(3):251–257, September 1972.
- [94] Bruno Nachtergaele and Robert Sims. Lieb-Robinson Bounds in Quantum Many-Body Physics. 2010.
- [95] S. Bravyi, M. B. Hastings, and F. Verstraete. Lieb-Robinson Bounds and the Generation of Correlations and Topological Quantum Order. *Physical Review Letters*, 97(5):050401, July 2006.
- [96] M. A. Rajabpour and S. Sotiriadis. Quantum quench in long-range field theories. *Physical Review B*, 91(4):045131, January 2015.
- [97] Kaden R. A. Hazzard, Mauritz Van Den Worm, Michael Foss-Feig, Salvatore R. Manmana, Emanuele G. Dalla Torre, Tilman Pfau, Michael Kastner, and Ana Maria Rey. Quantum correlations and entanglement in far-from-equilibrium spin systems. *Physical Review A*, 90(6):063622, December 2014.
- [98] Minh C. Tran, Chi-Fang Chen, Adam Ehrenberg, Andrew Y. Guo, Abhinav Deshpande, Yifan Hong, Zhe-Xuan Gong, Alexey V. Gorshkov, and Andrew Lucas. Hierarchy of Linear Light Cones with Long-Range Interactions. *Physical Review X*, 10(3):031009, July 2020.
- [99] Chi-Fang (Anthony) Chen, Andrew Lucas, and Chao Yin. Speed limits and locality in many-body quantum dynamics. *Reports on Progress in Physics*, 86(11):116001, November 2023.
- [100] Matthew B. Hastings and Tohru Koma. Spectral Gap and Exponential Decay of Correlations. *Communications in Mathematical Physics*, 265(3):781–804, August 2006.
- [101] Zhe-Xuan Gong, Michael Foss-Feig, Spyridon Michalakis, and Alexey V. Gorshkov. Persistence of Locality in Systems with Power-Law Interactions. *Physical Review Letters*, 113(3):030602, July 2014.
- [102] Romain Bachelard and Michael Kastner. Universal Threshold for the Dynamical Behavior of Lattice Systems with Long-Range Interactions. *Physical Review Letters*, 110(17):170603, April 2013.
- [103] Andrew Y. Guo, Minh C. Tran, Andrew M. Childs, Alexey V. Gorshkov, and Zhe-Xuan Gong. Signaling and scrambling with strongly long-range interactions. *Physical Review A*, 102(1):010401, July 2020.

Bibliography

- [104] David-Maximilian Storch, Mauritz Van Den Worm, and Michael Kastner. Interplay of soundcone and supersonic propagation in lattice models with power law interactions. *New Journal of Physics*, 17(6):063021, June 2015.
- [105] M E J Newman and G T Barkema. *Monte Carlo Methods in Statistical Physics*. Oxford University Press, 02 1999.
- [106] Shiwei Zhang. 15 auxiliary-field quantum monte carlo for correlated electron systems. *Emergent Phenomena in Correlated Matter*, 2013.
- [107] James Gubernatis, Naoki Kawashima, and Philipp Werner. *Quantum Monte Carlo Methods: Algorithms for Lattice Models*. Cambridge University Press, 2016.
- [108] Helmut G. Katzgraber. Introduction to Monte Carlo Methods.
- [109] Nicholas Metropolis, Arianna W. Rosenbluth, Marshall N. Rosenbluth, Augusta H. Teller, and Edward Teller. Equation of State Calculations by Fast Computing Machines. *The Journal of Chemical Physics*, 21(6):1087–1092, June 1953.
- [110] W. K. Hastings. Monte Carlo sampling methods using Markov chains and their applications. *Biometrika*, 57(1):97–109, April 1970.
- [111] N. Prokof'ev and B. Svistunov. Worm Algorithm for Problems of Quantum and Classical Statistics. 2009.
- [112] V. G. Rousseau. Superfluid density in continuous and discrete spaces: Avoiding misconceptions. *Physical Review B*, 90(13):134503, October 2014.
- [113] Olga Goulko, Andrey S. Mishchenko, Lode Pollet, Nikolay Prokof'ev, and Boris Svistunov. Numerical analytic continuation: Answers to well-posed questions. *Physical Review B*, 95(1):014102, January 2017.
- [114] N. V. Prokof'ev and B. V. Svistunov. Spectral analysis by the method of consistent constraints. *JETP Letters*, 97(11):649–653, August 2013.
- [115] Zoran Ristivojevic, Aleksandra Petković, Pierre Le Doussal, and Thierry Giamarchi. Superfluid/bose-glass transition in one dimension. *Phys. Rev. B*, 90:125144, Sep 2014.
- [116] Ehud Altman, Yariv Kafri, Anatoli Polkovnikov, and Gil Refael. Insulating phases and superfluid-insulator transition of disordered boson chains. *Phys. Rev. Lett.*, 100:170402, May 2008.
- [117] Ehud Altman, Yariv Kafri, Anatoli Polkovnikov, and Gil Refael. Superfluid-insulator transition of disordered bosons in one dimension. *Phys. Rev. B*, 81:174528, May 2010.
- [118] Lode Pollet, Nikolay V. Prokof'ev, and Boris V. Svistunov. Asymptotically exact scenario of strong-disorder criticality in one-dimensional superfluids. *Phys. Rev. B*, 89:054204, Feb 2014.
- [119] Daniel Barredo, Henning Labuhn, Sylvain Ravets, Thierry Lahaye, Antoine Browaeys, and Charles S. Adams. Coherent excitation transfer in a spin chain of three Rydberg atoms. *Phys. Rev. Lett.*, 114:113002, Mar 2015.

-
- [120] A. Piñeiro Orioli, A. Signoles, H. Wildhagen, G. Günter, J. Berges, S. Whitlock, and M. Weidemüller. Relaxation of an isolated dipolar-interacting Rydberg Quantum Spin System. *Phys. Rev. Lett.*, 120:063601, Feb 2018.
- [121] Antoine Browaeys and Thierry Lahaye. Many-body physics with individually controlled Rydberg atoms. *Nature Physics*, 16(2):132–142, February 2020.
- [122] G. Semeghini, H. Levine, A. Keesling, S. Ebadi, T. T. Wang, D. Bluvstein, R. Verresen, H. Pichler, M. Kalinowski, R. Samajdar, A. Omran, S. Sachdev, A. Vishwanath, M. Greiner, V. Vuletić, and M. D. Lukin. Probing topological spin liquids on a programmable quantum simulator. *Science*, 374(6572):1242–1247, December 2021.
- [123] Cheng Chen, Guillaume Bornet, Marcus Bintz, Gabriel Emperauger, Lucas Leclerc, Vincent S. Liu, Pascal Scholl, Daniel Barredo, Johannes Hauschild, Shubhayu Chatterjee, Michael Schuler, Andreas M. Läuchli, Michael P. Zaletel, Thierry Lahaye, Norman Y. Yao, and Antoine Browaeys. Continuous symmetry breaking in a two-dimensional Rydberg array. *Nature*, 616(7958):691–695, April 2023.
- [124] Sylvain de Léséleuc, Vincent Lienhard, Pascal Scholl, Daniel Barredo, Sebastian Weber, Nicolai Lang, Hans Peter Büchler, Thierry Lahaye, and Antoine Browaeys. Observation of a symmetry-protected topological phase of interacting bosons with Rydberg atoms. *Science*, 365(6455):775–780, 2019.
- [125] Irénée Frérot, Piero Naldesi, and Tommaso Roscilde. Entanglement and fluctuations in the XXZ model with power-law interactions. *Physical Review B*, 95(24):245111, June 2017.
- [126] Nicolas Dupuis. Superfluid–Bose-glass transition in a system of disordered bosons with long-range hopping in one dimension. *Physical Review A*, 110(3):033315, September 2024.
- [127] M E J Newman and G T Barkema. *Monte Carlo Methods in Statistical Physics*. Oxford University PressOxford, February 1999.
- [128] J. A. Nelder and R. Mead. A Simplex Method for Function Minimization. *The Computer Journal*, 7(4):308–313, January 1965.
- [129] Naoki Kawashima and Nobuyasu Ito. Critical Behavior of the Three-Dimensional $\pm J$ Model in a Magnetic Field. *Journal of the Physical Society of Japan*, 62(2):435–438, February 1993.
- [130] Jérôme Houdayer and Alexander Hartmann. Low-temperature behavior of two-dimensional Gaussian Ising spin glasses. *Physical Review B*, 70(1):014418, July 2004.
- [131] A B Harris. Effect of random defects on the critical behaviour of Ising models. *Journal of Physics C: Solid State Physics*, 7(9):1671–1692, May 1974.
- [132] J. T. Chayes, L. Chayes, Daniel S. Fisher, and T. Spencer. Finite-Size Scaling and Correlation Lengths for Disordered Systems. *Physical Review Letters*, 57(24):2999–3002, December 1986.

Bibliography

- [133] Björn Sbierski, Marcus Bintz, Shubhayu Chatterjee, Michael Schuler, Norman Y. Yao, and Lode Pollet. Magnetism in the two-dimensional dipolar XY model. *Physical Review B*, 109(14):144411, April 2024.
- [134] Oriana K. Diessel, Sebastian Diehl, Nicolò Defenu, Achim Rosch, and Alessio Chiocchetta. Generalized Higgs mechanism in long-range-interacting quantum systems. *Physical Review Research*, 5(3):033038, July 2023.
- [135] Guido Masella, Nikolay V. Prokof'ev, and Guido Pupillo. Anti-drude metal of bosons. *Nature Communications*, 13(1):2113, April 2022.
- [136] Ghassan Batrouni, Richard Scalettar, and Gergely Zimanyi. Quantum critical phenomena in one-dimensional Bose systems. *Physical Review Letters*, 65(14):1765–1768, October 1990.
- [137] J. K Freericks and H Monien. Phase diagram of the Bose-Hubbard Model. *Europhysics Letters (EPL)*, 26(7):545–550, June 1994.
- [138] Immanuel Bloch, Jean Dalibard, and Wilhelm Zwerger. Many-body physics with ultracold gases. *Reviews of Modern Physics*, 80(3):885–964, July 2008.
- [139] T Giamarchi and H. J Schulz. Localization and Interaction in One-Dimensional Quantum Fluids. *Europhysics Letters (EPL)*, 3(12):1287–1293, June 1987.
- [140] Jorge V José. *40 Years of Berezinskii–Kosterlitz–Thouless Theory*. WORLD SCIENTIFIC, August 2013.
- [141] Elmar Haller, Russell Hart, Manfred J. Mark, Johann G. Danzl, Lukas Reichsöllner, Mattias Gustavsson, Marcello Dalmonte, Guido Pupillo, and Hanns-Christoph Nägerl. Pinning quantum phase transition for a Luttinger liquid of strongly interacting bosons. *Nature*, 466(7306):597–600, July 2010.
- [142] G. Boéris, L. Gori, M. D. Hoogerland, A. Kumar, E. Lucioni, L. Tanzi, M. Inguscio, T. Giamarchi, C. D’Errico, G. Carleo, G. Modugno, and L. Sanchez-Palencia. Mott transition for strongly interacting one-dimensional bosons in a shallow periodic potential. *Physical Review A*, 93(1):011601, January 2016.
- [143] Antoine Browaeys, Daniel Barredo, and Thierry Lahaye. Experimental investigations of dipole–dipole interactions between a few Rydberg atoms. *Journal of Physics B: Atomic, Molecular and Optical Physics*, 49(15):152001, August 2016.
- [144] M. A. Baranov, M. Dalmonte, G. Pupillo, and P. Zoller. Condensed Matter Theory of Dipolar Quantum Gases. *Chemical Reviews*, 112(9):5012–5061, September 2012.
- [145] T Lahaye, C Menotti, L Santos, M Lewenstein, and T Pfau. The physics of dipolar bosonic quantum gases. *Reports on Progress in Physics*, 72(12):126401, December 2009.
- [146] R. Islam, C. Senko, W. C. Campbell, S. Korenblit, J. Smith, A. Lee, E. E. Edwards, C.-C. J. Wang, J. K. Freericks, and C. Monroe. Emergence and Frustration of Magnetism with Variable-Range Interactions in a Quantum Simulator. *Science*, 340(6132):583–587, May 2013.

-
- [147] Joseph W. Britton, Brian C. Sawyer, Adam C. Keith, C.-C. Joseph Wang, James K. Freericks, Hermann Uys, Michael J. Biercuk, and John J. Bollinger. Engineered two-dimensional Ising interactions in a trapped-ion quantum simulator with hundreds of spins. *Nature*, 484(7395):489–492, April 2012.
- [148] M. Ferraretto and L. Salasnich. Effects of long-range hopping in the Bose-Hubbard model. *Physical Review A*, 99(1):013618, January 2019.
- [149] Werner Krauth. Bethe ansatz for the one-dimensional boson Hubbard model. *Physical Review B*, 44(17):9772–9775, November 1991.
- [150] V.F. Elesin, V.A. Kashurnikov, A.V. Krashennnikov, and A.I. Podlivaev. Metal-insulator transition in Emery-Anderson model. Density of states calculations. *Physica C: Superconductivity*, 222(1-2):127–132, March 1994.
- [151] V. A. Kashurnikov, A. V. Krasavin, and B. V. Svistunov. Mott-insulator-superfluid-liquid transition in a one-dimensional bosonic Hubbard model: Quantum Monte Carlo method. *Journal of Experimental and Theoretical Physics Letters*, 64(2):99–104, July 1996.
- [152] M. Boninsegni, A. B. Kuklov, L. Pollet, N. V. Prokof'ev, B. V. Svistunov, and M. Troyer. Fate of Vacancy-Induced Supersolidity in He 4. *Physical Review Letters*, 97(8):080401, August 2006.
- [153] B. Capogrosso-Sansone, N. V. Prokof'ev, and B. V. Svistunov. Phase diagram and thermodynamics of the three-dimensional Bose-Hubbard model. *Physical Review B*, 75(13):134302, April 2007.
- [154] Barbara Capogrosso-Sansone, Şebnem Güneş Söyler, Nikolay Prokof'ev, and Boris Svistunov. Monte Carlo study of two-dimensional Bose-Hubbard model. *Physical Review A*, 77(1):015602, January 2008.
- [155] T. Botzung, D. Hagenmüller, G. Masella, J. Dubail, N. Defenu, A. Trombettoni, and G. Pupillo. Effects of energy extensivity on the quantum phases of long-range interacting systems. *Physical Review B*, 103(15):155139, April 2021.
- [156] M. Dalmonte, G. Pupillo, and P. Zoller. One-Dimensional Quantum Liquids with Power-Law Interactions: The Luttinger Staircase. *Physical Review Letters*, 105(14):140401, September 2010.
- [157] S. Baier, M. J. Mark, D. Petter, K. Aikawa, L. Chomaz, Z. Cai, M. Baranov, P. Zoller, and F. Ferlaino. Extended Bose-Hubbard models with ultracold magnetic atoms. *Science*, 352(6282):201–205, April 2016.
- [158] James R. Anglin and Wolfgang Ketterle. Bose–Einstein condensation of atomic gases. *Nature*, 416(6877):211–218, March 2002.
- [159] J. Bardeen, G. Baym, and D. Pines. Effective Interaction of He 3 Atoms in Dilute Solutions of He 3 in He 4 at Low Temperatures. *Physical Review*, 156(1):207–221, April 1967.
- [160] Marek Kutschera and Włodzimierz Wójcik. Proton impurity in the neutron matter: A nuclear polaron problem. *Physical Review C*, 47(3):1077–1085, March 1993.

Bibliography

- [161] Igor Bray, Xavier Weber, Dmitry V. Fursa, Alisher S. Kadyrov, Barry I. Schneider, Sudhakar Pamidighantam, Maciej Cytowski, and Anatoli S. Kheifets. Taking the Convergent Close-Coupling Method beyond Helium: The Utility of the Hartree-Fock Theory. *Atoms*, 10(1):22, February 2022.
- [162] R. Alhyder and G. M. Bruun. Mobile impurity probing a two-dimensional superfluid phase transition. *Physical Review A*, 105(6):063303, June 2022.
- [163] Zoe Z. Yan, Yiqi Ni, Carsten Robens, and Martin W. Zwierlein. Bose polarons near quantum criticality. *Science*, 368(6487):190–194, April 2020.
- [164] V. E. Colussi, F. Caleffi, C. Menotti, and A. Recati. Lattice Polarons across the Superfluid to Mott Insulator Transition. *Physical Review Letters*, 130(17):173002, April 2023.
- [165] Hartweg Tom. *Introduction to the Worm Algorithm and Application to Polaron Physics*. PhD thesis, University of Strasbourg, Strasbourg, 2023.
- [166] F. D. M. Haldane. Effective Harmonic-Fluid Approach to Low-Energy Properties of One-Dimensional Quantum Fluids. *Physical Review Letters*, 47(25):1840–1843, December 1981.
- [167] Berezinskii-Kosterlitz-Thouless transitions in classical and quantum long-range systems.